ANKARA YILDIRIM BEYAZIT UNIVERSITY

GRADUATE SCHOOL OF NATURAL AND APPLIED SCIENCES

FABRICATION AND CHARACTERIZATION OF COMPOSITIONALLY-ENGINEERED GLASS/CERAMIC/NANO-FILLER COMPOSITES FOR LTCC AND RADOME APPLICATIONS

Ph. D. Thesis by

Oğuzhan BİLAÇ

Department of Materials Engineering

July, 2023

ANKARA

FABRICATION AND CHARACTERIZATION OF COMPOSITIONALLY-ENGINEERED GLASS/CERAMIC/NANO-FILLER COMPOSITES FOR LTCC AND RADOME APPLICATIONS

A Thesis Submitted to

The Graduate School of Natural and Applied Sciences of

Ankara Yıldırım Beyazıt University

in Partial Fulfillment of the Requirements for the Degree of Doctor of Philosophy of Science in Materials Engineering

by

Oğuzhan BİLAÇ

July, 2023

ANKARA

Ph. D. THESIS EXAMINATION RESULT FORM

We have read the thesis entitled **"FABRICATION AND CHARACTERIZATION OF COMPOSITIONALLY-ENGINEERED GLASS/CERAMIC/NANO-FILLER COMPOSITES FOR LTCC AND RADOME APPLICATIONS"** completed by **Oğuzhan BİLAÇ** under the supervision of **PROF. DR. CİHANGİR DURAN** and we certify that in our opinion it is fully adequate, in scope and in quality, as a thesis for the degree of Doctor of Philosophy.

Prof. Dr. Cihangir DURAN

Supervisor

Prof. Dr. Caner DURUCAN

Jury Member

Prof. Dr. Hüseyin YILMAZ

Jury Member

Prof. Dr. Asaf Behzat ŞAHİN

Jury Member

Doç. Dr. Gülsüm TOPATEŞ

Jury Member

Prof. Dr. Sadettin ORHAN

Director

Graduate School of Natural and Applied Sciences

ETHICAL DECLARATION

I hereby declare that, in this thesis which has been prepared in accordance with the Thesis Writing Manual of Graduate School of Natural and Applied Sciences,

- All data, information and documents are obtained in the framework of academic and ethical rules,
- All information, documents and assessments are presented in accordance with scientific ethics and morals,
- All the materials that have been utilized are fully cited and referenced,
- No change has been made on the utilized materials,
- All the works presented are original,

and in any contrary case of above statements, I accept to renounce all my legal rights.

Date: 11.07.2023 **Signature:**

Name & Surname: Oğuzhan BİLAÇ

ACKNOWLEDGMENTS

I would like to express my gratitude to the all people who contributed in some way to the work described in this thesis. First, I would like to thank my advisor, Prof. Dr. Cihangir DURAN, for his guidance, patience, encouragement, and confidence in me.

I would like to thank to my examining committee members, Prof. Dr. Caner DURUCAN, Prof. Dr. Hüseyin YILMAZ, Prof. Dr. Asaf Behzat ŞAHİN and Assoc. Prof. Dr. Gülsüm TOPATEŞ for their criticism, insightful comments and valuable contributions to this work.

I would like to extend my deepest gratitude to my colleagues and lab mates in Ankara. Also, I would like to thank to Gebze Technical University for mechanical property measurements, Sivas Cumhuriyet University for dielectric and thermal property measurements, and Akcoat for thermal expansion coefficient and heat microscopy measurements as well as for providing glass frit powder.

Financial supports from Scientific and Technological Research Council of Turkey (TÜBİTAK, 112M216/1002) and AYBU-BAP (FDK-2021-2262) are highly appreciated.

Most of all, I would like to thank my family, my parents, and my brother for all the support. Finally, I would like to thank my wife Gamze and my children Meryem Sare and Zeynep Meva for all their constant supports, encouragement and trust. Without their support, none of this would have been possible.

2023, 11 July **Oğuzhan BİLAÇ**

FABRICATION AND CHARACTERIZATION OF COMPOSITIONALLY-ENGINEERED GLASS/CERAMIC/NANO-FILLER COMPOSITES FOR LTCC AND RADOME APPLICATIONS

ABSTRACT

It was aimed to optimize mechanical, thermal and dielectric properties of (SiO_2-Al_2O_3-CaO based) glass/ceramic/(and nanofiller (hexagonal boron nitride, aluminum nitride) composites for functional and structural applications. A base alumina/55 weight percent glass composition was first selected and then engineered to improve overall physical properties. For this purpose, mullite as the replacement for alumina as well as addition of nano fillers (e.g., platelet-shaped hexagonal nano boron nitride particles or nano aluminum nitride powders) were primarily considered. Densification, phase formation, microstructure evolution, mechanical properties (hardness, flexural strength, elastic constant), dielectric properties (dielectric constant and loss) and thermal properties (thermal conductivity, thermal expansion coefficient) were investigated as a function of glass content (10 to 60 weight percent), nano filler content (1 to 10 weight percent) and crystalline phases (mullite or alumina). Densification mechanism was liquid phase sintering for the 10-30 weight percent glass and viscous sintering for the 50-60 weight percent glass compositions. Nano fillers aluminum nitride and hexagonal boron nitride neither chemically reacted with other phases nor decomposed due to sintering temperatures less than 950 °C. Closed porosity was found to be a critical parameter for the nano filler-added composites. The overall results were evaluated to comply with some potential structural and functional applications such as low temperature co-fired ceramics (e.g., mullite/55 weight percent glass/10 weight percent hBN; bulk density=2.3 g/cm^3 after sintering at 900 °C, dielectric constant (loss) = 5.13 (0.003) at 5 MHz, thermal conductivity = 1.91 W/m·K at 25 °C, thermal expansion coefficient= 4.89 ppm/°C, flexural strength=71 MPa and elastic modulus=71 GPa) and radome (mullite/20 weight percent glass; high sintering temperature of 1450°C and highest thermal shock resistance parameter of 162°C together with dielectric constant (loss)=7.12 (0.0025) at 5 MHz (and dielectric constant=5.9 at 4–10 GHz), thermal conductivity=3.72 W/m·K, thermal expansion coefficient=4.27 ppm/°C, flexural strength=180 MPa, elastic modulus=189 GPa). These results are comparable with respect to the commercial products. Finally, low-temperature co-fired ceramic and radome prototypes were successfully fabricated by tape casting and gel casting, respectively.

Keywords: Ceramic processing, low-temperature co-fired ceramics, radome material, dielectric properties, thermal properties, mechanical properties.

LTCC VE RADOM UYGULAMALARI İÇİN KOMPOZİSYON OLARAK TASARLANMIŞ CAM/SERAMİK/NANO-DOLGU KOMPOZİTLERİN ÜRETİMİ VE KARAKTERİZASYONU

ÖZ

Bu çalışmada, fonksiyonel ve yapısal uygulamalar için (SiO_2-Al_2O_3-CaO bazlı) cam/seramik/(ve nano dolgu (hegzagonal bor nitrür, alüminyum nitrür)) kompozitlerin mekanik, termal ve dielektrik özelliklerinin optimize edilmesi araştırılmıştır. İlk olarak alümina/ağırlıkça yüzde 55 cam bileşimi seçilmiş ve ardından kompozisyon tasarımı ile genel fiziksel özelliklerin iyileştirilmesi tamamlanmıştır. Bu sebeple, öncelikle alümina yerine müllit ve ayrıca nano dolgu malzemeleri (örneğin, plaka şeklinde hegzagonal nano bor nitrür parçacıklar veya nano alüminyum nitrür tozlar) eklenmiştir. Kompozitlerin yoğunlaşma, faz oluşumu, mikroyapı gelişimi, mekanik (sertlik, eğilme mukavemeti, elastik sabit), dielektrik (dielektrik sabiti ve kayıp) ve termal (termal iletkenlik, termal genleşme katsayısı) özellikleri, cam miktarı (ağırlıkça yüzde10-60), nano dolgu miktarı (ağırlıkça yüzde 1-10) ve kristal fazların (müllit veya alümina) bir fonksiyonu olarak incelenmiştir. Yoğunlaştırma mekanizması, ağırlıkça yüzde 10-30 cam miktarı için sıvı faz sinterleme ve ağırlıkça yüzde 50-60 cam miktarı için ise viskoz sinterleme metodu ile olmuştur. Nano dolgu alüminyum nitrür ve hegzagonal bor nitrür malzemeleri, diğer fazlarla kimyasal olarak reaksiyona girmemiştir ve sinterleme sıcaklıkları 950 ºC'nin altında olduğu için faz değişimi olmamıştır. Kapalı gözeneklilik, nano dolgu katkılı kompozitler için kritik bir parametre olduğu saptanmıştır. Sonuçlar, düşük sıcaklıkta birlikte pişirilen seramikler (örneğin, müllit/ağırlıkça yüzde 55 cam/ağırlıkça yüzde 10 hBN; 900 °C'de sinterlemeden sonra kütle yoğunluğu=2.3 g/cm^3, 5 MHz'de dielektrik sabit (kayıp) = 5.13 (0.003), 25 °C'de termal iletkenlik = 1.91 W/m·K, termal genleşme katsayısı= 4.89 ppm /°C, eğilme mukavemeti=71 MPa ve elastik modül= 71 GPa) ve radom (örneğin, müllit/ağırlıkça yüzde 20 cam; 1450°C'de yüksek sinterleme sıcaklığı ve 162°C olan yüksek termal şok direnci parametresi ve 5 MHz'de dielektrik sabit (kayıp)=7.12 (0.0025) (ve 4–10 GHz'de dielektrik sabit=5.9), termal iletkenlik=3.72 W/m·K, termal genleşme katsayısı=4.27 ppm/°C, eğilme mukavemeti=180 MPa, elastik modül=189 GPa) gibi bazı potansiyel yapısal ve fonksiyonel uygulamalara uygunluk açısından değerlendirilmiştir. Elde edilen sonuçlar ticari ürünler ile kıyaslanabilir seviyede olduğu bulunmuştur. Son olarak düşük sıcaklıkta birlikte pişirilen seramikler ve radom prototipleri, sırasıyla şerit dökümü ve jel döküm yöntemleri ile başarılı bir şekilde üretilmişlerdir.

Anahtar Kelimeler: Seramik süreçler, düşük sıcaklıkta birlikte pişirilen seramik, radom malzeme, dielektrik özellikler, termal özellikler, mekanik özellikler.

CONTENTS

NOMENCLATURE

ABBREVIATIONS

μm	Micrometer
Al_2O_3	Alumina
hBN	Hexagonal boron nitride
AlN	Aluminum nitride
CaO	Calcium Oxide
K_2O	Potassium Oxide
Na_2O	Sodium Oxide
MPa	Mega Pascal
Na_2O	Sodium Oxide
rpm	Round per minute
SiO_2	Silica
vol%	Volume percent
wt%	Weight percent
AM	Acrylamide
MBAM	Methylenebisacrylamide
APS	Ammoniumpersulfate
TEMED	Tetramethylenediamine
3-D	3-Dimension
MHz	Megahertz
GHz	Gigahertz
GPa	Giga Pascal
ppm	Part per million
ZrO_2	Zirconium oxide
TiO_2	Titanium oxide

Fe_2O_3	Ferric oxide
MgO	Magnesium oxide
CTE	Thermal expansion coefficient
d_{50}	Median particle size
$3Al_2O_3.2SiO_2$	Mullite

Acronyms:

EDS	Energy Dispersive Spectrometry
HV	Vickers Hardness
LPS	Liquid Phase Sintering
OM	Optical Microscope
SEM	Scanning Electron Microscopy
XRD	X-ray Diffraction
TG-DTA	Thermogravimetric-Differential Thermal Analysis
LTCC	Low Temperature Co-Fired Ceramics

LIST OF TABLES

LIST OF FIGURES

CHAPTER 1

INTRODUCTION

1.1 Glass Structure and Properties

The definition of glass has taken various forms with their development, some of which are "non-crystalline solids", "materials obtained by solidification of a liquid without crystallization" and "all amorphous solids obtained by supercooling a liquid, regardless of chemical composition"[1]. Glass is defined by ASTM as "inorganic melting product cooled to rigid conditions without crystallization". Silicates are the most important compositions of the glasses [2][3].

Conventionally, glasses are obtained by cooling a liquid at a rate at which crystallization can be prevented. Therefore, glass formation can also be defined as the inhibition of crystallization. During cooling process, a temperature where the liquid-solid phase transformation and changes in physical properties occur is expressed as glass transition temperature (T_g). Unlike crystalline materials, glasses do not show a sharp melting point; instead, they gradually soften. Finally, they become fluid due to constantly decreasing viscosity with increasing temperature [4]. Figure 1.1 displays volume-temperature diagram of a material having a glassy characteristic in the crystalline, amorphous, and liquid states [5]. A rapid cooling rate prevents the structure from being rearranged, raising the T_g value and lowering the density. Also, vice versa is true. The viscosity of the glasses changes depending on the temperature. The solid's viscosity is approximately 10^{15} poise (P), while the viscosity at T_g is between 10^{13} and 10^{14} P. Consequently, the sample acts like a solid [6].

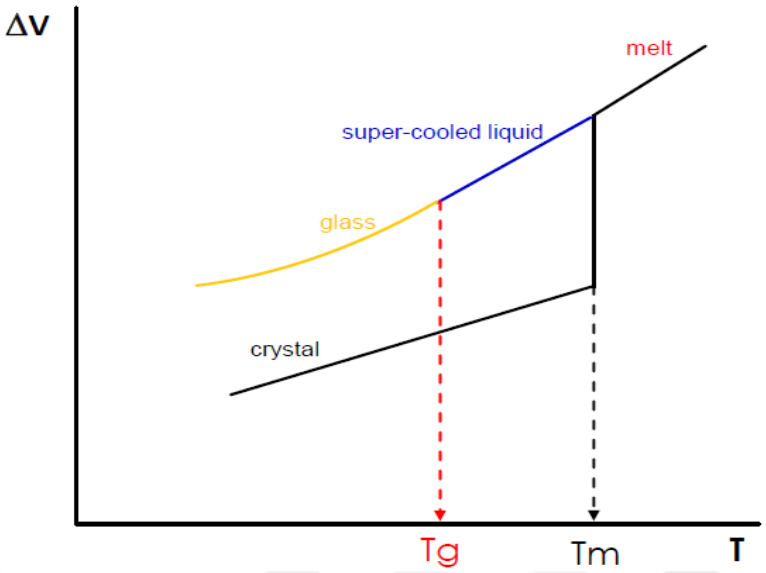

Figure 1.1 Specific volume-temperature relations of liquid, glass and crystal [5].

Many models and approaches have been developed to explain the structures of glasses [4]. The most important one is the random mesh model that explains three-dimensional layout of an amorphous material [7]. According to this model, glasses are seen as a three-dimensional mesh with a certain symmetry and non-periodicity. These non-repetitive networks in oxide-based glasses consist of oxygen polyhedra. The randomness of oxide networks in the structure causes glass to have a higher internal energy with respect to crystalline state. Zachariasen's observations, who put forward one of the first theories about the glass formation, support this model [3][4][7], and are summarized below [8];

1. The formation of an oxygen triangle or tetrahedron requires only a small number of oxygen ions to coordinate around the center cation—4 or less.

2. These polyhedra share their corners, not edges or faces

3. No more than two cations should be connected to each oxygen ion.

4. Each polyhedron should have three corners that are shared.

Figure 1.2 shows the differences between the random network and regular crystal structure of an A_2O_3 type oxide. In both cases, the structures are composed of AO_3

triangles. Unlike crystalline materials that repeats periodically, glasses are amorphous materials and has an irregular structure with short-distance ordering [3].

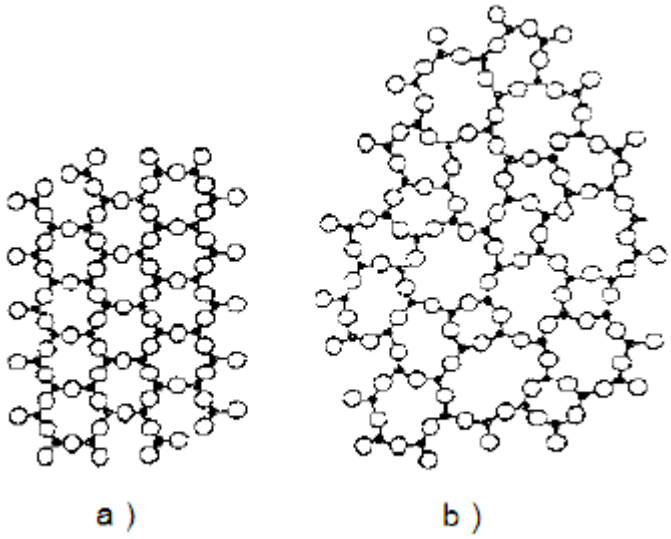

Figure 1.2 Two-dimensional schematic representation of A_2O_3 type oxide a) crystal structure, b) random network structure [3].

In order to form a glass structure, a rapid cooling is required below melting temperature and crystallization of the overcooled liquid must be prevented. Therefore, crystallization rate is an important factor controlling glass formation [9] and it should be very low in glassy materials. If a melt cannot be cooled fast enough to solidify in a glassy amorphous structure, crystallization occurs [1][10].

Oxides used in commercial glass production are divided into three basic classes, that is, glass-forming oxides, modifying oxides and intermediate oxides [4][9]. Usually glass-forming oxygen polyhedras are triangles or tetrahedras. The most basic of the network former oxides; mainly SiO_2, B_2O_3, GeO_2, P_2O_5, As_2O_5 [3][4] . Modifying oxides are not used as glass-forming materials alone, but they disrupt the mesh structure of the glass and fabricate a more densely arranged order. When these oxides are used in certain ratios, they allow an opportunity to modify the production conditions or properties of the final glass. Examples of modifying oxides include Na_2O, K_2O, Li_2O, PbO, MgO, ZnO and BaO. Intermediate oxides can be added to the glass mesh structure, although they generally do not have the ability to make glass

alone. Examples of intermediate oxides are Al_2O_3, BeO, PbO, TiO_2 and ZrO_2. This group of intermediate oxides can serve as both network former and modifying oxides [1][4][9] Figure 1.3 shows SiO_2 network and SiO_2 network modified through addition of Na_2O.

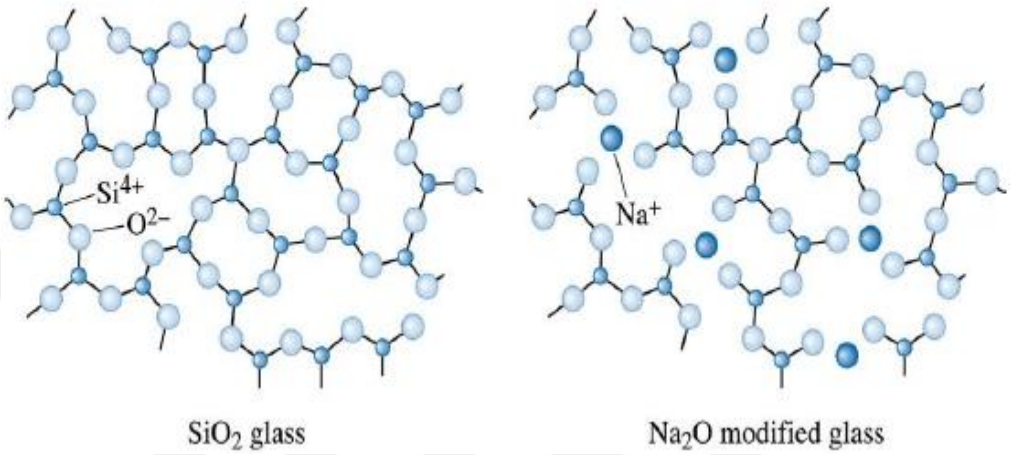

Figure 1.3 Schematic glass networks; SiO_2 network and SiO_2 network modified through addition of Na_2O [11].

Table 1.1 displays the characteristics and potential uses of commercially available glass compositions.

Table 1.1 Several typical commercial glass compositions and characteristics [12].

Glass Type	Composition (wt%)						Characteristics and Applications
	SiO_2	Na_2O	CaO	Al_2O_3	B_2O_3	Other	
Fused silica	>99.5						High melting temperature, very low coefficient of expansion (shock resistance)
96% Silica (Vycor)	96				4		Thermally shock and chemically resistant laboratory ware
Borosilicate (Pyrex)	81	3.5		2.5	13		Thermally shock and chemically resistant ovenware
Container (soda-lime)	74	16	5	1		4 MgO	Low melting temperature, easily worked, also durable
Fiberglass	55		16	15	10	4 MgO	Easily drawn into fibers-glass-resin composites
Optical flint	54	1		18		37 PbO, 8 K_2O	High density and high index of refraction optical lenses
Glass-ceramic	70					4.5 TiO_2, 2.5 Li_2O	Easily fabricated; strong; resists thermal shock-ovenware

1.2 Glass-Ceramics

Glass-ceramics are polycrystalline materials made from glasses that have been deliberately crystallized. Crystallization in glasses occurs with the nucleation and growth of crystal phases within the glass as a result of heat treatment [11][13]. The structure of a glass-ceramic usually contains 50-95 vol% crystalline phase. It is aimed to alter mechanical properties of glass-ceramic compared to the main glass. While glass-ceramics show high wear and corrosion resistance compared to metals, they show superior impact resistance and fracture toughness compared to glasses. As a result, glass-ceramics have many uses and enable the development of unique microstructures with unique characteristics [14][15]. There are two ways of obtaining glass-ceramic; glass-ceramic route (controlled heat treatment of a melt) and glass /ceramic route (also named as a composite where crystalline ceramic phase is admixed with a glass phase) [16].

1.2.1 Glass-Ceramic Route

This technique uses a thermal procedure to fabricate a glass ceramic from a glass. There are two primary stages: the powder method, in which glass powder mixtures are sinter-crystallized, and the standard approach, in which glass batches are volume-crystallized. The materials are first melted to fabricate a glass in the traditional method, and then the glass ceramic is fabricated by carefully controlling crystallization to promote crystal nucleation and growth. Figure 1.4 provides a schematic illustration of the typical crystallization method of a glass. Small nuclei are formed in the glass during the nucleation stage, and crystals are grown by heating to a higher temperature during the crystal growth stage, as shown in Figure 1.5. Either homogeneous nucleation in the absence of foreign boundaries or heterogeneous nucleation in the presence of foreign boundaries causes nucleation of glass. This stage is a process in which the transformation of an amorphous phase to a more stable crystalline phase takes place as a result of energy reduction. In general, the development of crystal grains growing in an amorphous phase may result in a non-uniform body with large grain size, even though glass ceramics should be free of cracks, holes, and surface roughness through regulated crystallization. Generally, ZrO_2 and TiO_2 are the most commonly used nucleating agents to control crystallization and crystal size [5].

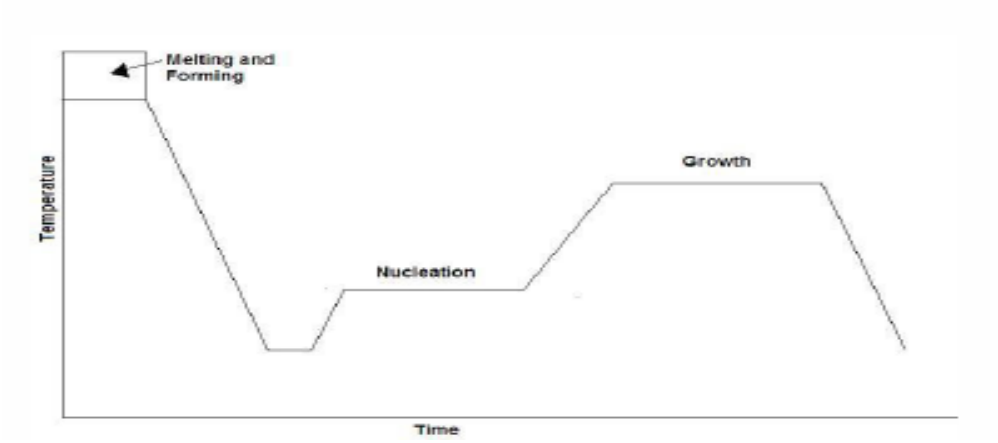

Figure 1.4 Glass crystallization in a typical method: a schematic processing cycle [5].

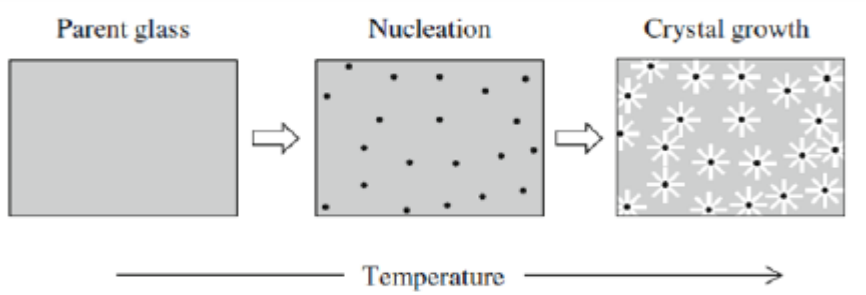

Figure 1.5 Glass-ceramic formation by conventional method [14].

1.2.2 Glass/Ceramic Route

The conventional glass-ceramic production method has one disadvantage because it requires a nucleation / crystal growth step that is difficult to control and economically costly [11]. In addition, defects such as pores remain in the glass-ceramic adversely affect the resulting mechanical properties. However, glass/ceramic composite route does not require heating above melting temperature; instead, densification of the composite is achieved by softening and wetting of glass on ceramic powders during sintering. The amount of glass determines by which sintering (or densification) method will apply because densification occurs through a fully reactive, partially reactive or non-reactive system depending on the reactivity between glass and ceramic phases. In reactive systems, glass reacts with ceramic at sintering temperature and acts as a binding agent between glass and ceramic. In non-reactive systems, ceramic particles are slightly soluble in glass during sintering. The dissolution of ceramic in glass in partially reactive environments is localized and constrained. Also, shape accommodation and particle growth are not observed in partial reactive systems. The crystal phase increases viscosity and minimizes distortion during sintering. Additionally, the glass/ceramic mechanical strength is increased by the crystalline phases presence. The glass phase connects and embraces the crystalline phase, which enables tailoring of properties. As a result, the glass to ceramic ratio largely determines the special features of the glass/ceramic structure [16].

1.3 Sintering Process and Fundamentals

The term sintering is basically the enlargement of the contact area between the solid particles by mass transport events through or around the pores under suitable conditions of time, temperature, pressure, and atmosphere. This process results in an increase in strength and a decrease in system total energy. The sticking of ice cubes in a glass of water due to the temperature difference between water and ice can be seen as the simplest example of sintering [17]. Some of the first sintered products were bricks that were heated over an open-hearth fire to increase their strength. The first reports on sintering were published on platinum material in 1829. Since the early 1900s, the first steps have been taken to establish the theory and practice of sintering. In the late 1940's, the first analyzes of sintering were proposed by Rhines for solid phase sintering and Lenel for liquid phase sintering [18]. Since the early 21st century, sintering has been used in a wide variety of products including dental implants, rocket nozzles, aircraft wing weights, ultrasonic transducers, turbochargers, semiconductor substrates, golf clubs [18].

The reduction in surface area and surface free energy caused by the replacement of solid-vapor contacts are the driving forces during sintering. By reducing surface area (solid-vapor) and forming interparticle bonds (solid-solid), sintering lowers the system's free energy. On the microscopic scale, material transport is affected by changes in pressure and differences in free energy. If the particle size is small, these effects become very large [5].

Sintering is an irreversible process. Once the powder is heated, it will not revert back to powder form due to the elimination of weak solid-vapor contacts. Engineering properties such as strength, ductility, conductivity, magnetic permeability and corrosion resistance improve significantly during sintering. Improving these properties is the primary rationale for sintering. The sintering properties depend on the microstructure. With prolonged sintering, the microstructural properties develop to a point where they peak, then decrease with continuous heating for longer periods and at higher temperatures. Not only the strength is greatly increased, but also the compact density is increased due to shrinkage [19].

1.3.1 Sintering Mechanisms

Sintering can be carried out with different methods depending on the type of material, the shape and size of the sample. The neck growth between the contacting particles corresponds to the first stage of sintering, where the sintering behavior is controlled by curvature gradients. The neck size increases during the first stage of sintering until the neck size is less than one-third of the particle size. In general, there is not much dimensional change, so linear shrinkage up to 3% is seen in the first stage. The second stage corresponds to the rounding of the pores and the onset of grain growth. Tubular pores are linked to the surface. The final step of sintering commences when the porosity is 8%. Pores are closed and spherical. Typically, the component is more than 92% dense at the final stage. Particle size, surface area, temperature, time, green density, pressure, and environment are among the factors that affect sintering. The changes that occur during sintering are given in Figure 1.6 [20][21].

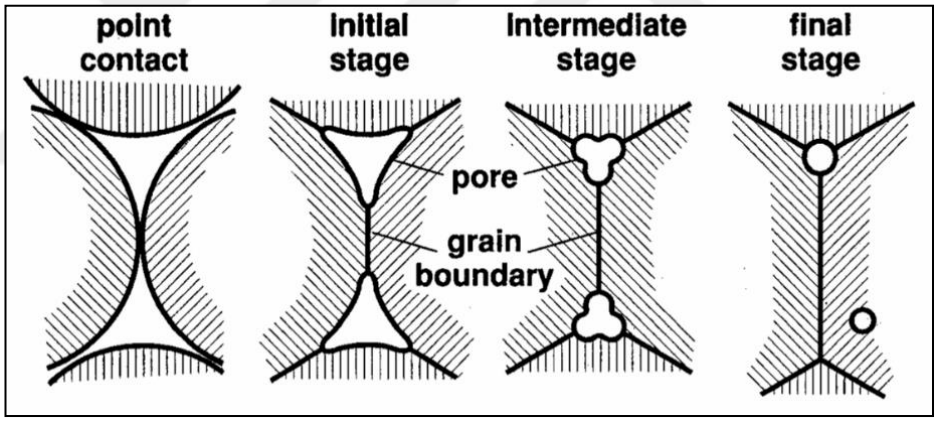

Figure 1.6 Schematic diagrams of the pore structure changes during sintering [20]

Sintering takes place by diffusion of atoms. This diffusion is due to the difference in chemical potential, and hence atoms move from an area with a higher chemical potential to an area with a lower chemical potential. The different paths that atoms take to move from one point to another are called transport mechanism. There are two mechanisms (i.e., surface and bulk transports) and densification occurs by means of bulk transport mechanisms (e.g., volume diffusion, grain boundary diffusion, plastic flow, and viscous flow) [7][22]. The interparticle distance can only be reduced by transporting material across the grain boundary, either by viscous flow or by atomic

motion. Therefore, grain boundaries are the source of material transport for densification and shrinkage [23]. In general, sintering is grouped as solid state, liquid phase and viscous sintering.

1.3.1.1 Solid State Sintering

The ions that make up the ceramic must have enough mobility in the microstructure for solid state sintering to begin. When the ceramic is heated above roughly 80% of its melting point, this mobility is typically possible. Significant changes to the microstructure occur early in the process of solid state sintering. Ion diffusion from convex to concave surfaces is one of the main diffusion mechanisms. This process reduces the curvature at particle contact points and lowers the system's free energy. Since mass transport and pore shape change only occur in areas near the pore surface, this mechanism does not aid in densification [20][24].

The difference in free energy between neck region and powder surface acts as a driving force during sintering. Densification increases as lower energy solid-solid contacts replace with higher energy solid-vapor interfaces. Due to the intrinsic imperfections of grain boundaries, pore shrinkage and densification are facilitated. Following the removal of pores and completion of densification process, the system's free energy can be further decreased through grain growth. Therefore, densification takes place by reducing the size of thermodynamically unstable pores [20] [24][25]. Figure 1.7 schematically illustrates the stages of solid phase sintering. By diffusing materials from higher chemical potential regions to lower chemical potential regions, solid state sintering takes place. A notable characteristic of sintering is the development of necks between interacting particles.

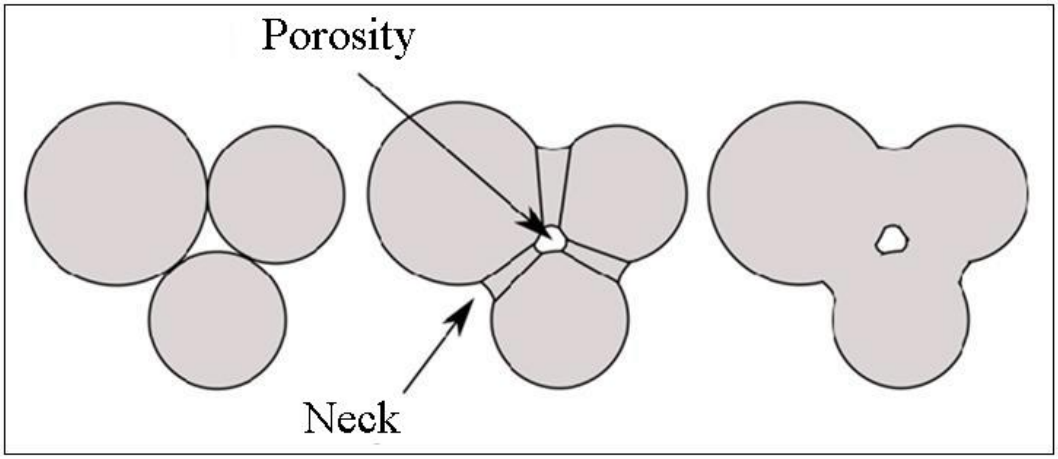

Figure 1.7 Solid state sintering [22]

1.3.1.2 Liquid Phase Sintering

In liquid phase sintering, temperature and composition are chosen so that usually less than 5 vol% liquid is formed between the particles [22]. In order to fabricate a eutectic liquid during sintering, crystalline solids must be heated and melted. It is crucial that the crystalline phase has a solubility in the liquid. In this instance, material transport is accomplished through a "solution-precipitation" mechanism in which atoms dissolve in high-energy regions and precipitate in lower-energy regions. The liquid must wet the solid particles and the solid must be soluble in the liquid in order for liquid phase sintering to occur. The concentration of the liquid and the solubility of the solid in the liquid, or an increase in reactivity, increase as the temperature rises above the eutectic temperature [20][26].

Densification is a multi-step process during liquid phase sintering. Initially, the liquid begins to flow thru the ceramic particles under the influence of capillary forces, which results in rearrangement of particles and contributes to densification. This process is easy due to the lubricating effect of the formed liquid phase. To reduce the system free energy, the material on the convex particle surfaces starts to dissolve in the liquid and diffuse to the concave surfaces. The particles can now alter their tetracaidecahedral shapes to fill the vacant places. With the help of solution-precipitation, densification continues as a solid three-dimensional skeletal framework forms. In the final stage, pores are closed and spherical, and densification continues similar to solid state

sintering [20][26][27]. Figure 1.8 shows the stages of liquid phase sintering schematically. The liquid forms during the heating stage. Sintering is accompanied by rearrangement in the initial step, followed by solution-precipitation and final stages.

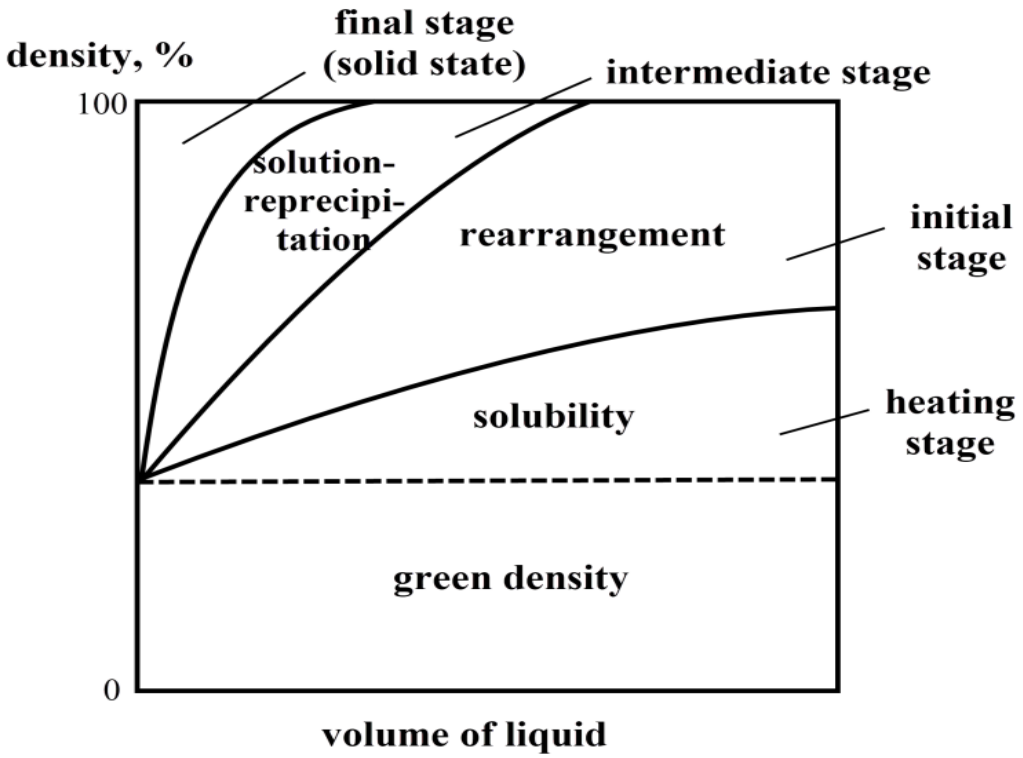

Figure 1.8 Stages of densification during liquid phase sintering according to liquid content [22].

The goal of liquid phase sintering is to reduce the system's interface free energy. In general, the change in free energy when moving from one configuration to another in a solid-liquid-vapor system is;

$$\Delta G = \Delta A_{sv}\gamma_{sv} + \Delta A_{ss}\,\gamma_{ss} + \Delta A_{sl}\,\gamma_{sl} + A_{lv}\gamma_{lv} \qquad 1.1$$

Here, ΔA_{sv}, ΔA_{ss}, ΔA_{sl}, and ΔA_{lv} are the changes in various interface areas, and γ_{sv}, γ_{ss}, γ_{sl} and γ_{lv} are the corresponding interface energies (subscripts s, l, and v represent solid, liquid, and vapor, respectively). Assuming the solid is thoroughly wetted by a liquid, ΔA_{sv} and ΔA_{ss} are negligible. Also, ΔA_{sl} can be neglected in the absence of grain growth. Therefore, "$A_{lv}\gamma_{lv}$ is the primary and most important component of the driving force for liquid phase sintering [27]. The rate of deformation of the liquid film

particles during rearrangement is proportional to the shear stress to reduce the liquid-vapor surface area. Accordingly, the densification ratio is;

$$d(\Delta p/p_0)=A(g)(\gamma v/\eta)r_s^{-1} \quad 1.2$$

Here, ρ is density, t is time, A(g) is the geometric factor, η is the liquid viscosity, and r_s is the radius of the solid particle [27]. As the viscosity and radius of solid particle decrease densification rate increases.

1.3.1.3. Viscous Sintering

Densification is accomplished by viscous flow if the volume of liquid is more than 36 vol% (see Figure 1.8). The path along which matter travels is not determined in viscous flow mechanism. Instead, the equations for matter transport are derived from Frenkel's energy balance notion, in which the rate of energy dissipation by viscous flow is set equal to the rate of energy gained by surface area decrease. When there is enough liquid to completely cover the solid surfaces, rearrangement is the primary method of achieving densification [5][22].

The three key elements are viscosity, particle size and pore size. The rate of viscous sintering is inversely proportional to the glass viscosity. If η (viscosity) is constant, as in sintering at a constant temperature, the degree of densification after time t is proportional to dt/η. Because the extent of densification and crystallization are both determined by the same viscosity function, any factor that changes the viscosity influences both processes in such a way that the volume fraction of crystals is exactly the same when a desired density is reached. The crystallization process is unaffected by the glass microstructure, however, according to viscous sintering theories, the densification rate is inversely related to pore size (r). Small pores promote fast sintering while not interfering with the driving force for crystallization. One of the most successful strategies for enhancing the densification rate to crystallization rate ratio is to reduce pore size. As was already mentioned, densification is enhanced by particle size reduction. The following is the Arrhenius dependency of viscosity on temperature [5]

$$\eta(T)=\eta_0\cdot\exp(E/R\cdot T) \quad 1.3$$

where η is viscosity ($N.s/m^2$), T is temperature (K), η_0 is a coefficient, E is the activation energy (J/mol) and R is the universal gas constant (J/mol·K). Viscosity drops with rising temperature. The viscosity of the glass can also be decreased at a controlled temperature by altering the composition [5].

1.4 Properties

Basic properties such as elastic modulus, flexural strength, stiffness, fracture toughness, thermal shock resistance, dielectric constant, dielectric loss, thermal conductivity, and coefficient of thermal expansion are briefly explained here. The formulae are provided in the Experimental Procedures section together with the necessary ceramic dimensions and measurement data.

1.4.1 Mechanical Properties

1.4.1.1 Flexural strength

A maximum tensile strength at fracture is its flexural strength for brittle materials. While fracture in glasses is non-crystallographic and has an easy cleavage plane, it happens along a crystallographic cleavage plane in polycrystalline materials. Polycrystalline ceramics can impede crack growth and prevent fracture because they have barriers like grain boundaries. Flaws might cause fracture to begin in brittle solids at an specific applied stress that is lower than the theoretically-calculated values [5].

1.4.1.2 Elastic modulus

Elastic property is important in determining materials behavior when subjected to a deformation process. It is related to the forces between atoms. In other words, an increase in spacing distance between the atoms correlates to the elastic elongation of a body under an applied load. The overall modulus in two-phase systems is intermediate between two components [5].

The elastic modulus of a polyphase ceramic will also be an additive function of the individual properties (or characteristics) of the crystalline and glassy phases. It is expected in the glass-ceramics that elastic constant of the main crystalline phase will

determine the overall modulus of elasticity due to its high modulus for majority of the cases. In particular, CaO, MgO, and Al_2O_3 appear to have a noticeable impact on the elastic moduli of glasses [4]. A comparison of the elastic module of glass-ceramic materials with other materials is shown in Table 1.2.

Table1.2 Comparison of elastic modulus of glass-ceramics with other materials [11].

Materials	Elastic Modules (GPa)
Glass	7.2
Soda lime glass	6.9
Glass-ceramics	8.3-13.8
Electro porcelain (glazed)	6.6
Ceramics	36.6
Pyrex	6.6

1.4.1.3 Hardness

It refers to a material's resistance to localized plastic deformation. It is measured by the amount of penetration of a hard object into a material. Low values indicate soft materials and vice versa. Hardness is not one of the fundamental physical properties of a material, but is a complex function of the physical properties depending on the test method. Hardness tests are used because they are straightforward, affordable, and non-destructive, and the results can be used to forecast some mechanical qualities [4][12].

1.4.1.4 Fracture toughness

Fracture is the splitting of a solid body into two or more parts under stress. Fracture toughness (K_{IC}) is the resistance of a material to crack propagation under load. High fracture toughness materials are more crack propagation resistant, while low fracture toughness materials have lower crack propagation resistance. Similarly, the fracture toughness of single crystals is lower than polycrystalline ones. The microstructure of polycrystalline materials, which includes grain boundaries and other obstacles to crack propagation, also reflects an uneven crack route, such as intragranular or intergranular fractures. Although pores can serve as stress concentrators, they sometimes have a tendency to slow the spread of cracks [28].

1.4.1.5 Thermal shock resistance (TSR)

The ability of a material to withstand abrupt temperature changes without being damaged and without causing weight loss is called the thermal shock resistance. The undesired stress that results from thermal expansion can quickly cause a component to fracture due to thermal shock. Fracture occurs when a body crack is extended by enough stress level. The critical temperature difference (ΔT) is defined as a TSR parameter of R (°C) for extremely rapid cooling and represented as;

$$R=\Delta T=\sigma_f \cdot (1-\mu)/\alpha \cdot E \quad (1.4)$$

where σ_f is the flexural strength (Pa), μ is the poison's ratio, α is the thermal expansion coefficient (CTE) (ppm/°C) and E is the Elastic modulus (Pa). However, this formula does not make the test geometry clear. The second TSR parameter, R' (kW/m), includes thermal conductivity and is displayed as;

$$R'=\Delta T=\sigma_f \cdot k \cdot (1-\mu)/\alpha \cdot E \quad (1.5)$$

Where k is thermal conductivity (W/m·K). Higher thermal shock resistance is provided by higher TSR values. The values of R and R' vary when thermal conductivity is included [29]. For a high TSR, low α and E together with high σ_f and k are required. Porosity also influences TSR [30]. The effect of porosity on elastic modulus of Al_2O_3 produced by spark plasma sintering and normal sintering is shown in Figure 1.9. The

elastic modulus decreases with increasing porosity. Therefore, an optimization is needed according to the porosity (or densification) level because porosity decreases k [30].

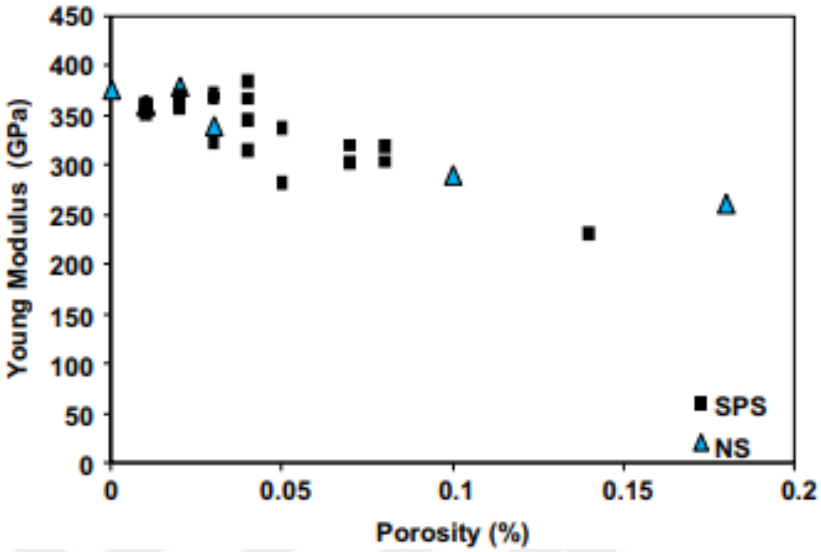

Figure 1.9 The effect of porosity on elastic modulus of micro-structured Al_2O_3 by natural sintering and spark plasma sintering [30].

1.4.2 Dielectric properties

Electrical conductivity is implemented by atomic level charge that carries electrons and electron holes. For electrical conductivity, charge carriers have a long-range motion. When charge carriers have short motion under an electric field, dielectric dipoles occur. Ionic solids contain positive and negative charge carriers and when there is an applied electric field in solid, these charge carriers will be separated. This behavior is named polarization and it is a finite displacement [31]. Figure 1.10 shows four different polarization types in dielectric materials: namely, electronic, ionic, orientational (dipolar) and space charge (interfacial) polarization. A net dipole formation is observed. In electronic polarization, electrons move in opposite direction with respect to the nucleus. Ionic polarization occurs only in ionic materials. Applied electric field displaces cations to negative side and displaces anions to positive side. Dipolar polarization occurs only in materials that have a permanent dipole moment. It occurs as a result of the rotation of permanent dipoles in line with applied field. The

orientation of all dipoles is just a little bit shifted, so that an average orientation in field direction results. The interfacial (space charge) polarization occurs when there is an accumulation of charge at an interface between two materials or two regions within a material because of an external field[28]. The total polarization of a material is the total of all polarization types, and is given as [32] ;

$$P_t = P_e + P_i + P_d + P_s \quad (1.6)$$

P_e: Electronic polarization

P_i: Ionic polarization

P_d: Orientational (dipolar) polarization

P_s: Space charge (interfacial) polarization

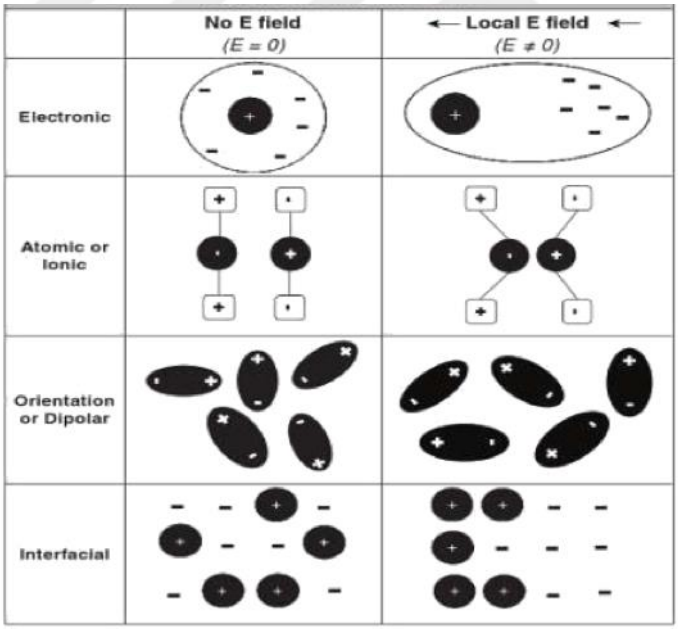

Figure 1.10 Polarization mechanisms [32]

Materials are polarizable with different ways. According to frequency response, dielectric constant of a material varies. Under an electrical field, the dipoles are reoriented with the field. In practice, materials show a relaxion time for charge transport and relaxation frequency for realignment of the dipoles. Change in the

polarization mechanisms as a function of frequency vary the dielectric constant as represented in Figure 1.11 [32].

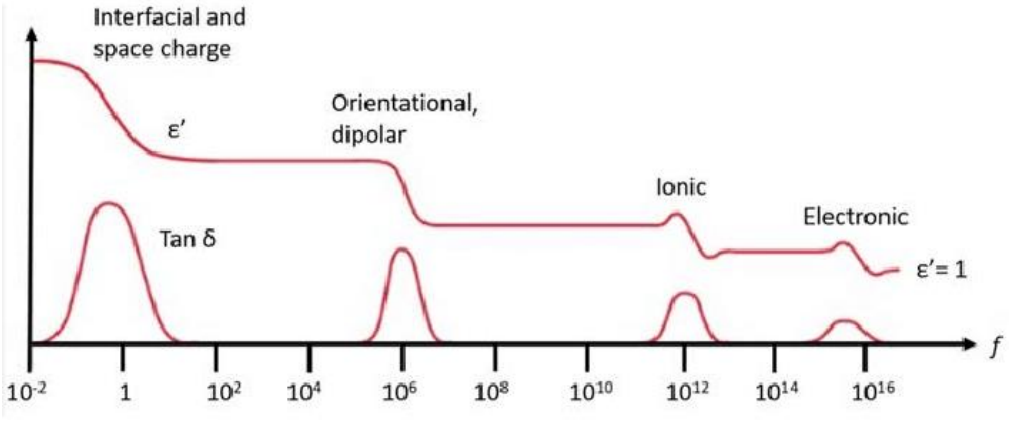

Figure 1.11 Frequency dependence of polarization contributions to the dielectric constant [32]

Dielectric constant (K) is called relative permittivity and represents how a material is polarized under an electric field. The relative permittivity is determined by dividing a material's permittivity by that of a vacuum or free space. The formula is given as[33];

$$K = {}^{\varepsilon}/_{\varepsilon_0} \tag{1.7}$$

K: relative permittivity (dielectric constant)

ε: permittivity of a material (F/m)

ε_0: permittivity of free space or vacuum (8.8541×10^{-12} F/m)

The dielectric loss tangent (tan δ) of a material represents the amount of electrical energy that is dissipated quantitatively as a result of various physical processes, including electrical conduction, dielectric relaxation, dielectric resonance, and loss from non-linear processes. The delay between the electric field and the electric displacement vectors can also be thought as a factor in the origin of dielectric losses. Figure 1.12 shows tangent of the dielectric loss angle between current and voltage in a material. It serves as a measure of the heat production of ceramic when operated. This direct measurement typically takes place under the same conditions as capacity measurement. When it comes to leakage current (a current that leaks through the

insulator and to earth), commercial insulators do not always lead the applied voltage by exactly 90˚. The phase angle is smaller than 90˚. The dielectric loss angle is defined as the complementary angle δ= 90˚-θ [34]. The following formula can be used to calculate the power loss P of a dielectric for an insulator with capacitance (C) and a voltage V applied to it at a frequency (f, Hz);

$$P = V^2\, 2\pi f C tan\delta \qquad 1.8$$

As long as V, f and other factors are constant, P depends on only tanδ. Intrinsic and extrinsic losses together make up the overall dielectric loss. The losses in perfect crystals known as intrinsic dielectric losses rely on crystal structure and can be explained by how the phonon system interacts with the ac electric field. The temperature, ac field frequency, and crystal symmetry all affect intrinsic dielectric losses. In single crystals without defects or perfectly pure materials, these inherent losses fix the bottom limit of losses. Extrinsic losses are connected to imperfections in the crystal structure, including impurities, microstructural defects, grain boundaries, porosity, microcracks, order-disorder, random crystallite orientation, dislocations, vacancies, dopant atoms, etc. Extrinsic losses are caused by lattice defects, therefore they can theoretically be completely removed or minimized with the right material preparation. The losses resulting from various defects exhibit varying frequency and temperature dependence. The temperature and frequency dependences of dielectric losses in crystals with various symmetry groups vary [35].

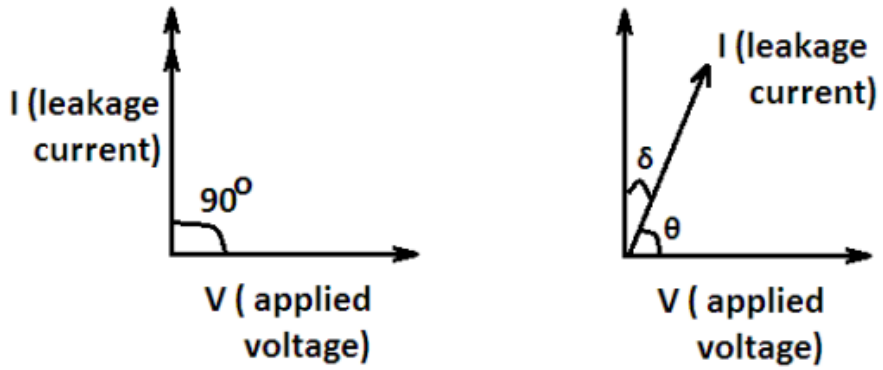

Figure 1.12 The dielectric loss of an ideal (left) and commercial (right) dielectric [35].

1.4.3 Thermal properties

1.4.3.1 Thermal conductivity

The thermal conductivity (W/m·K) means how easy or difficult to move energy through a material under a temperature gradient. Free electrons and lattice vibration are two means of heat conduction. Consequently, it is dependent on atomic bonds. Lattice vibration is more dominant in ceramics and energy is carried by phonons. The free electron predominates in metallic materials leading to higher thermal conductivity. In solids, thermal conductivity is determined by temperature, interactions between phonons, and the mean free path of phonons scattering from lattice defects in the solid. The mean free route is determined by phonon-phonon interactions. Temperature-dependent phonon scattering results in a short mean free path, which results in a lower thermal conductivity as temperature rises. Additionally, structural defects including grain boundaries, secondary phases, chemical impurities, and dislocations can scatter phonons. The mean free route of the phonons is also constrained by the random network (e.g., extremely irregular and disordered) or amorphous structure of glasses. Extremely low heat conductivity in amorphous materials is caused by atomic or molecular movement (migration). The increase in the thermal conductivity results from the improvement of atomic or molecular migration with increasing temperature [28][36][37]. The thermal conductivity of crystalline and amorphous ceramics is given in Table 1.3.

Table 1.3 Thermal conductivity of crystalline and amorphous ceramics.

Materials	k (W/m·K)	T (ºC)
Al_2O_3 [37]	36 - 6.3	25-900
Vitreous silica[38]	0.85 - 1.5	(-150 – (+100))
Soda lime glass[38]	0.8 - 1.15	(-100 – (+100))

1.4.3.2 Thermal expansion coefficient

As temperature rises, the volume of a crystal expands as a result of increasing atomic separation due to lattice vibrations. Therefore, the coefficient of thermal expansion (CTE, ppm/°C) is a property of materials to measure volumetric change as a function of temperature. Bond strength and crystal structure are closely connected to the CTE. For example, diamond has a high bond strength with a low CTE (1 ppm/°C) [12]. In general, ceramic materials have lower CTE values than metallic materials because they have stronger ionic and covalent bonds. Silicate glasses have low CTEs due to ability of absorbing vibrational energy by adjusting irregular bond angles [28]. CTE can be stated in two different ways: as an average coefficient of thermal expansion (α) over a range of temperatures, or as the real coefficient of thermal expansion ($\bar{\alpha}$) at a given temperature [39]. Table 1.4 shows the thermal conductivity and thermal expansion coefficient of metal, glass ceramic and polymer materials.

Table 1.4 Thermal properties of metal, glass ceramic and polymer materials [12]

Materials	Thermal conductivity (W/m·K)	Thermal expansion coefficient (ppm/ºC)
Aluminum	247	23.6
Alumina	36	6.5-8.1
Borosilicate glass	1.4	3.3
Polyethylene	0.3-0.5	0.46-0.48

1.5 Applications

1.5.1 Low Temperature Co-Fired Ceramics

The rapid growth of information technology requires electronic components that are small, lightweight and multi-functional. Multi-layer ceramics allow the production of high-density electronic substrates by integrating conductive paths in a three-dimensional compact structure with desired properties. They are an essential part of multi-chip module (MCM) technology as they allow for the convenience, high-density integration and packaging in the production of complex systems[16][40]. In the past, microwave devices were conventionally machined from metal, and RF (radio frequency) connections were often made, leading to expensive, heavy and bulky packets [41][42]. But nowadays, automotive industry, entertainment electronic devices and electronic circuits for telecommunication must take up as little space as possible as they have to meet ever-increasing demand requirements [41][42]. In the development of complex miniaturized circuits, glass-ceramic inserts, known as low-temperature co-sintering ceramic (LTCC) substrate, play a decisive role as the base material and have become a critical component in the development of various modules and substrates [43][44][45]. In this technology, multilayer 3D LTCC modules are

produced by combining thin ceramic layers with low dielectric properties and conductive paths. LTCC enables a versatile mixture of passive microwave components such as microstrips, strips, antennas, filters, resonators, capacitors, and inductors, allowing the creation of a practical whole design matrix on Al_2O_3 or any other substrate. Also, these integrated components are interconnected by a 3D stripe circuit [24, 27, 28]. The most important parameter for the LTCC technology is low sintering temperature that is <950 °C [40]. In this respect, it provides an advantage of packaging in today's microelectronics and microwave modules. Since LTCC can densify at low temperatures, it enables usage of low melting temperature metals such as silver, copper, gold (961 °C for Ag, 1063 °C for Au, and 1083 °C for Cu) with high conductivity, low dielectric resistance, low conductivity loss for embedded microwave components and transmission lines [40]. Glass is intentionally added to the composition to increase densification at low sintering temperatures. The dielectric, mechanical and thermal properties depend on the intrinsic properties and microstructure (e.g., amorphous phase, ceramic phase, crystallized phase and residual pores). Taking into account of low thermal expansion (close to Si), high strength, and high thermal conductivity, the glass-ceramic-based LTCC technology has a distinct advantage over polymer-based one, especially in terms of low loss and high-speed data communication at high-frequency circuits. Additionally, they work well in a variety of potential applications, including miniaturized devices having a high integration density, wireless communication systems, microwave products, integrated circuit packaging of radar and antennas, RF devices, and automotive applications. Materials with low dielectric constant enable devices with high signal speed to be produced [16], [33], [40], [46], [47], [48]]. As shown in Figure 1.13, LTCC modules enable the integration of passive and active electronic components such capacitors, inductors, resistors, and filters. These components are integrated into layers, enabling the creation of a monolithic structure with improved functionality, performance, and reliability [49].

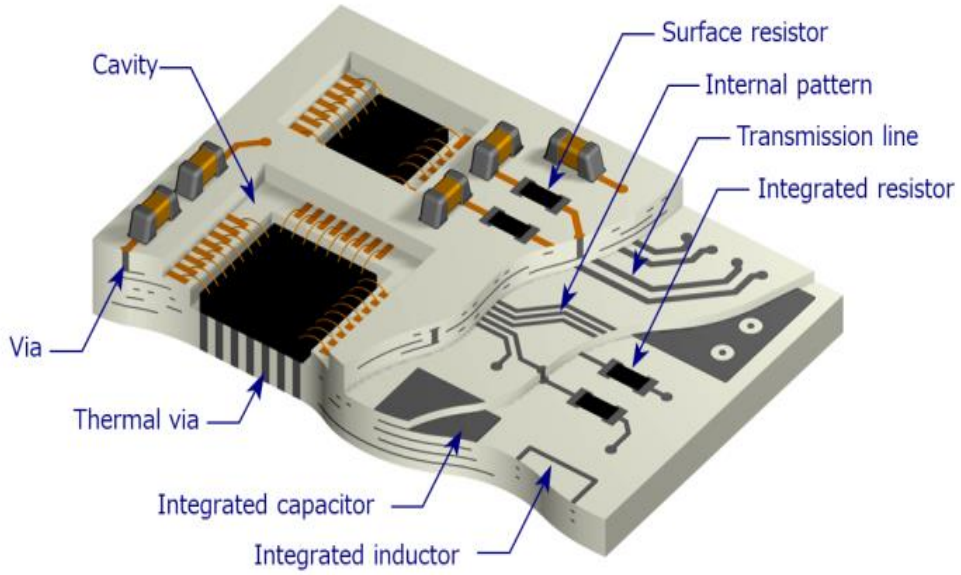

Figure 1.13 An advanced LTCC package where the components are integrated into the module [49].

1.5.1.1 Requirements

The following are the requirements for LTCC materials in general;

Low sintering temperature: The sintering temperature must be lower than the melting point of the electrode since LTCC materials are heat-treated alongside a metal electrode. A common electrode material is Ag because of its excellent conductivity and chemical stability. Ag melts at a temperature of 961 °C. As a result, LTCC's sintering temperature should be lower than 950 °C [16], [40], [50].

Low dielectric constant and dielectric loss: Substrate layers often employ materials with low dielectric constants (4–12), whereas capacitor layers typically use materials with high dielectric constants. Signal propagation delay is one of the most important parameters in electronic packaging which is directly related with dielectric constant as follows:

$$t_d = l \cdot \sqrt{K}/c \qquad 1.9$$

where t_d: propagation delay (s), l metal line length (m), K: dielectric constant of the pad and c: speed of light (m/s). For high-speed signal transmission, the dielectric

constant must be low. Dielectric loss also has a direct impact on both power usage and signal quality. Low dielectric constant and loss are crucial characteristics for the LTCC systems [16][40],[51][52].

Low thermal expansion and high thermal conductivity: The reliability of the entire system is impacted when thermal expansion mismatch damages solder connections between substrate and chip in the systems using Si chips mounted on LTCC substrates. Therefore, thermal expansion coefficient of the substrate should be close to Si (~ 2.6-3.3 ppm/°C). The thermal conductivity of the substrate material is another crucial factor. The thermal conductivity formula is given in the equation below;

$$k = \alpha \cdot q \cdot C_p \qquad 1.10$$

where k: thermal conductivity (W/m·K), α: thermal dissipation coefficient (m^2/sec), q:density (kg/m^3) and C_p: heat capacity (J/kg·K). The low thermal conductivity of LTCC, which is typically between 2 and 5 W/m·K, is one of its key disadvantages. It is essential for more reliable and effective packaging that the heat produced by the device be removed. Heat removal has become increasingly important as the demand for high-density, high-power devices that run at high speeds grows [16], [40], [51].

Chemical compatibility with electrode material: Because the formation of additional phases has potential to alter or worsen the overall performance, electrode material (i.e., conductive paste containing glass to bond well to the LTCC substrate) must not react with the LTCC [16]. Table 1.5 lists some of the basic characteristics of commercial LTCC materials from leading manufacturers. In general, high thermal conductivity comes with high dielectric constant. Therefore, optimization of dielectric, thermal and mechanical properties is strongly required by means of compositional engineering.

Table 1.5 Commercial LTCC products and properties [53][54][55][56].

LTCC supplier	Code	Sintering Temperature	Dielectric constant	Dielectric loss	CTE (ppm/°C)	Thermal Conductivity (W/m·K)	Flexural Strength (MPa)	Elastic Modulus (GPa)
Kyocera	GL330	-	7.7 (at 2 MHz)	0.0005 (at 2 MHz)	8.2	4.3	400	178
	GL952		7.9 (at 2 MHz)	0.0015 (at 2 MHz)	8.3	1.8	250	119
	GL570		5.7 (at 2 MHz)	0.0007 (at 2 MHz)	3.4	2.8	200	128
	GL771		5.2 (at 2 MHz)	0.0036 (at 2 MHz)	12.3	2	170	74
	GL773		5.8 (at 2 MHz)	0.0023 (at 2 MHz)	11.7	1.9	280	95
Murata	LFC	900 °C	7.7 (at 1 MHz)	0.0040 (at 6 GHz)	5.5	2.5	270	-
	AWG		8.8 (at 1 MHz)	0.0042 (at 6 GHz)	7.2	3.5	300	
	SWG		8.8 (at 1 MHz)	0.0042 (at 6 GHz)	7.2	3.5	450	
Dupont	951	850 °C	7.8 (at 10 GHz)	0.0140 (at 10 GHz)	5.8	3.3	320	120
	9K7		7.1 (at 10 GHz)	0.0010 (at 10 GHz)	4.4	6.4	230	145
Ferro	A6-M	850 °C	5.75 - 6.05 (at 100 MHz)	0.002 (at 100 MHz)	-	-	193	-
	A6-C		6.0 - 6.7 (at 100 MHz)	0.005 (at 100 MHz)			207	
Heraeus	X200 /X200W	880 °C	8.8 – 9.5 (at 30 MHz)	< 0.002 (at 30 MHz)	5.6	3	-	-
	503K08 /51555 W	-	7.5 – 8.5 (at 1 MHz)	< 0.001 (at 1 MHz)	5.2	-		

1.5.1.2 Tape Casting Method

In Figure 1.14, the tape casting method is schematically depicted for the production of LTCC technology. In LTCC process, each layer is fabricated separately and then laminated to form a monolithic substrate. The process begins with tape casting of glass-ceramic slurry under a doctor blade at a desired thickness. To enable electrical connections between the layers on the substrate's vertical axis, the holes or paths (i.e., vias) are physically punched or laser-cut, then filled with conductive paste. To make horizontal interconnects on the surface of the layers, each layer is screen-printed

individually. Typically, electrically conductive holes and a distinct set of printed electrical traces are present on the surface of each layer. The ceramic sheets are then layered, laminated, sintered, and finally assembled after post-firing metallization and electrical testing. This layer, track, and via arrangement are carefully planned to form a three-dimensional ceramic block with an imbedded electrical circuit. [16], [40], [49].

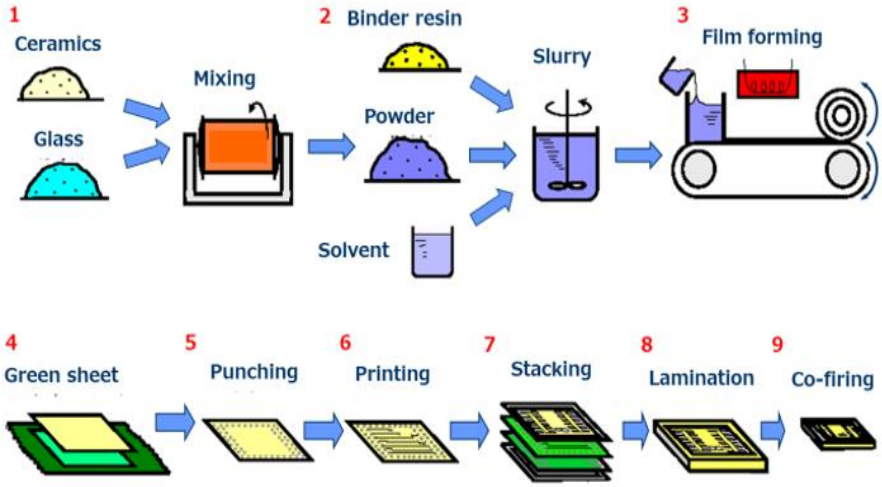

Figure 1.14 LTCC produced by tape casting [57].

1.5.2 Radome

An antenna enclosure known as a radome protects radar from outside environment while maintaining electrical and magnetic performance of the system. Radom material should provide required structural strength without impairing the antenna's electromagnetic performance. As a result, the material transmission loss is greatly influenced by its dielectric constant and dielectric loss. Additionally, radome material needs to be lightweight and highly resistant to rain erosion. There are many application areas for radome, such as air radar, aviation, maritime communications, surveillance, satellite communications, coastal surveillance, military and civilian flight simulation, military and civilian radar, microwave and broadcast equipment. The picture of an aviation radome is shown in Figure 1.15.

Figure 1.15 Missile radome [58]

There are 3 basic types of radome: airborne radome (aircraft and missile radomes), ground floor radome, and shipboard radome according to their application areas. Radomes that are ground-based must endure wind-induced air pressure changes. Moisture, rain, snow, and moisture buildup on the exterior wall are additional issues to take into account. Radome inside the ship must resist corrosion from the salty marine environment. Typically, monolithic or sandwich forms of fiberglass-reinforced polymer matrix composites are employed extensively for shipboard and ground-based radomes. They have an advantage such as low production costs and light weight [59][60][61]. As for the radome in the air, attention should be paid to thermal gradients caused by thermal shocks, high terminal velocities and accelerations. Additionally, pressure difference and impact strength, that is, the impact loads from birds, stones, and rain, are other crucial factors in choosing effective materials. Polymer matrix composites can only be used for low-speed radomes. However, radome running faster than Mach 2 over an extended length of time are vulnerable to a rise in temperature. Ceramic, silica or glass based inorganic materials must be preferred at speeds exceeding Mach 2. These materials must not only withstand high temperatures without deterioration in performance, but also protect against rain erosion. Water absorption

decreases the strength of the radome and increases the dielectric constant and dielectric loss [59][60][62]. Table 1.6 provides a list of some fundamental characteristics of the common radome materials.

Table 1.6 Commercial materials for radome applications [63]

Materials	Flexural Strength, MPa	Elastic Modulus, GPa	Thermal Expansion Coefficient, Ppm/°C	Thermal Conductivity, W/m·K	Thermal Shock Resistance, R	Dielectric constant	Dielectric loss
Al_2O_3	270 (25°C) 250 (500°C) 220 (1000°C)	380 (25°C) 350 (500°C) 285 (1000°C)	6.5-8.1 (25-1000 °C)	38 (25°C) 29 (100°C) 13 (500°C)	Fair	9.6 (25°C, 10-40 GHz) 10.3 (500°C, 10GHz) 11.4 (1000°C, 10GHz)	0.0001 (10 GHz, 25°C), 0.0005 (10 GHz, 500°C) 0.0014 (10 GHz, 500°C)
Pyroceram 9606	235 (25°C) *200 (500°C)* 75 (1000°C)	120 (25°C *120 (500°C)* 100 (1000°C)	3 (25°C) *7.8 (120°C)* 3.8 (500°C)	3.8 (2 °C) *3.2 (500°C)* 2.9 (1000°C)	Good and better than Al_2O_3	5.7 (25°C, 10-40 GHz) *5.8 (500°C,10GHz)* 6.1 (1000°C, 10 GHz)	0.00025 (25 °C, 10-40 GHz) *0.001 (500°C,10 GHz)* 0.0016 (750 °C, 10 GHz)
BN	130 (25°C) 85 (500°C) 25(1000°C)	95 (25°C) 70 (500°C) 50 (750°C)	3.2	25.1 (100°C) 18.8 (500°C) 12.6 (1000°C)	Very good	4.5 (25°C, 10-40 GHz) 4.6 (500°C, 10 GHz) 4.78 (1000°C, 10GHz)	0.0006 (500°C, 10 GHz) 0.0009 (750°C, 10 GHz)
BeO	260 (25°C) 225 (400°C) 150 (800°C)	320 (up to 400°C) 300 (500°C) 250 (800°C)	8 (20-100°C) 7.7 (20-500°C) 9.1 (20-1000°C)	293 (20°C) 92 (500°C) 50 (750°C)	Very good	6.6 (25 °C, 10-40 GHz) 7.2 (500°C, 10GHz) 8 (1000 °C, 10GHz)	0.0003 (25°C, 10 GHz) 0.0006 (25°C, 36 GHz) 0.0014 (100°C, 10 GHz)
Si_3N_4	425 (25-1000°C)	310 (25-1000°C	3.2	21 (20°C) 13.4 (1000°C)	Excellent	7.9 (25°C, 10-40 GHz) 8.2 (750°C, 10 GHz)	<0.005 (25°C, 10-40 GHz) <0.005 (700°C, 10 GHz)
Mullite	Tensile 130 (25°C) 100 (700°C)	220 (up to 700°C)	4 (20-500 °C 4.5 (20-1000°C)	6.3 (25-600°C)	improved thermal shock with respect to Al_2O_3	6.6 (25°C, 10-40 GHz) 6.7 (700°C, 10 GHz)	<0.001 (25°C, 10-40 GHz) <0.0045 (25-750°C, 10 GHz)
SiO_2	44 (25°C) 54 (500°C) 66 (1000°C)	50 (25-850°C)	1.5 (25-800°C)	0.6 (25-900°C)	Very good	3.5 (25°C, 10-40 GHz) 3.55 (500°C, 10GHz) 3.8 (1000°C, 10GHz)	<0.0006 (25°C, 10-40 GHz) 0.001 (500°C, 10-GHz) 0.0016 (750°C, 10GHz)

1.5.2.1 Requirements

The following are the specifications for radome materials in general;

Dielectric requirements: The antenna inside the radome should experience the least amount of electromagnetic distortion possible. For the radome electrical performance, the material dielectric constant and loss are crucial. The signal propagation time (see Equation 1.9) and transmission loss of an electromagnetic wave through the radome must be minimal, necessitating a low dielectric constant. Additionally, for high-power applications, the radome material high dielectric loss raises the temperature, which reduces its electrical characteristics and increases system noise. Therefore, dielectric loss of the radome should also be low. In addition to these, the shape and design of the radome is a very important parameter in terms of overall system performance [60][61].

Mechanical requirements: Aerodynamics, structural stability, and operating environment are among the mechanical requirements. Mechanical stresses in radome material are caused by airflow, acceleration forces and sudden thermal expansion. Radome material is required to maintain sufficient strength even above service temperature. Thermal shock typically results in the largest mechanical stresses for high-speed radomes. In addition, the system (antenna and radome) must be resistant to vibrations or mechanical impacts, and therefore designs of these structures are of great importance. Thermal shock resistance (see Equation 1.4 and 1.5) is one of the important parameters and is expressed above [60][61];

As can be seen, to have high thermal shock resistance, σ_f and k must increase and α and E must decrease. Therefore, radome ceramic composition is of great importance to fulfill these required parameters.

High rain erosion: It is expected that radomes have a high electromagnetic transmission coefficient. Moisture absorbed by a radome can have a significant impact on this performance due to the change in dielectric properties [64]. In this regard, the density and pore structure (open and/or closed) are important. Since density is also related to strength, it also affects the abrasion resistance that may be caused by rain erosion.

When organic materials like Teflon are unsuitable for high-temperature radomes, Al_2O_3 is typically utilized instead. As a result of its ability to endure Mach 3 speed, it is frequently utilized for missile radomes. At 10 GHz, the dielectric loss is minimal

(0.001) and the dielectric constant is approximately 10. Its relatively high density (3.95 g/cm^3) results in a reduction in the thickness of the design. Materials with high dielectric constants require mechanical machining with a narrower tolerance in manufacturing compared to the lower dielectric constant materials. Al_2O_3 is sufficient in terms of mechanical properties and rain erosion resistance [63]. Commercial magnesium-aluminum silicate glass-ceramic Corning Pyroceram (9606) is resistant to high temperatures caused by velocities above Mach 3, making it suitable for missile radomes. The thickness tolerance in the design is made possible by the microwave range dielectric constant of 5.65. It is lighter than Al_2O_3 and has a density of 2.62 g/cm^3. Given that it softens at 1350 °C, Al_2O_3 mechanical characteristics are only slightly better. It also offers excellent resistance to rain erosion. It is well acknowledged that Al_2O_3 is less resistant to thermal shocks [63][65]. A commercially produced glass ceramic called MACOR has 45% borosilicate glass and 55% fluorophlogopite mica. It is stable at 800 °C and can withstand up to 1000 °C. Its properties include density of 2.52 g/cm^3, dielectric constant of 6.01, dielectric loss of 0.004 at 1 kHz, elastic modulus of 67 GPa, and flexural strength of 94 MPa [65][66]. Chen et al. [67] investigated that porous Si_3N_4 ceramics (porosity of 40%–71%) exhibited flexural strength of 6.8–80 MPa and dielectric constant of 2.29–4.84. Also, Fangsen et al. [68] reported that 20–50 wt% Si_3N_4 coated urea balls resulted in 48%–70% porosity, very low flexural strength of 24–80 MPa and dielectric constant of 2.7–3.9.

Densification is closely related to dielectric (i.e., dielectric constant decreases if densification decreases), mechanical (i.e., E and σ_f decrease if densification decreases) and thermal properties (i.e., k decreases if densification decreases). In other words, the pores significantly lower (or, improve) the dielectric properties but, at the same time, degrades the mechanical properties sharply that may limit the practical usage. As with the LTCC materials, optimization of dielectric, mechanical and thermal properties must be ensured for the radomes based on their speeds.

1.5.2.2 Gel Casting Method

Gel casting is an essential 3D ceramic fabrication technology because it enables for the manufacturing of large and complex form ceramics. Figure 1.16 depicts a

schematic representation of the gel casting process. Powder, monomer solution (mixing acrylamide (AM) and methylenebisacrylamide (MBAM)), initiator ammoniumpersulfate (APS), and catalyzer tetramethylenediamine (TEMED) are mixed to prepare gel cast slurries. First, monomer solution, dispersant, and powder mixture are mixed together to obtain a stable slurry. Then, for several minutes, APS and TEMED are mixed together. If quick curing is desired, TEMED is added. Green samples are shaped using molds [69].

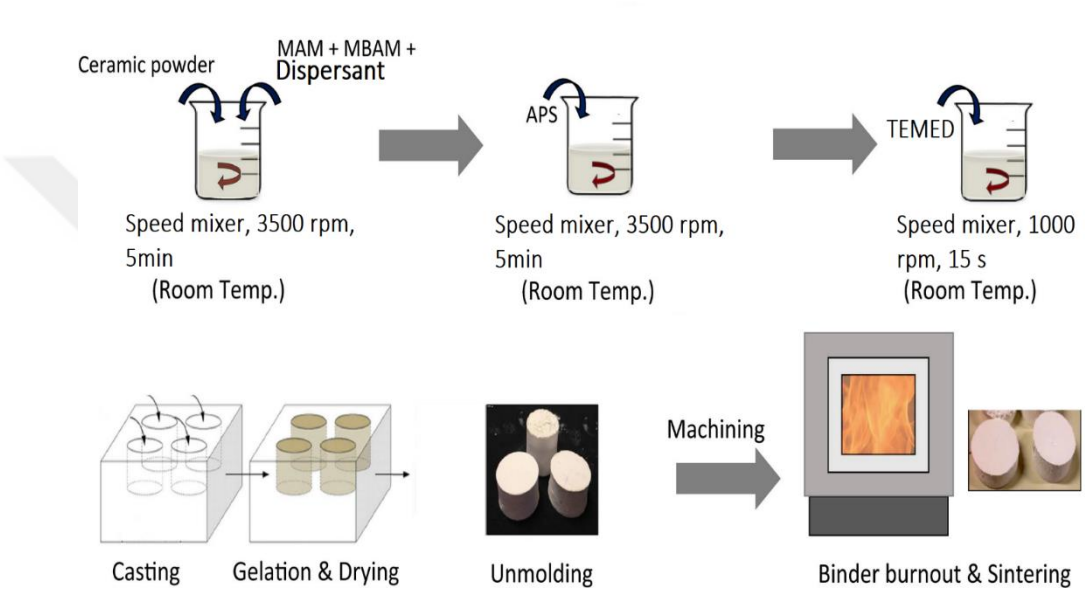

Figure 1.16 The mechanism of gel casting [69]

The cross-linking process of acrylamide monomers in the presence of APS and TEMED is depicted in Figure 1.17. The acrylamide monomers are cross-linked to generate polyacrylamide. With TEMED, APS forms oxygen free radicals from the catalysts such as O_2, O_2^-, OH, and H_2O_2. Then, the process is initiated by oxygen free radicals. Finally, the double bonds in the AM and MBAM between CH_2 and CH are broken. At this moment, linear monomer interconnection and crosslinking bisacrylamide monomers form [70].

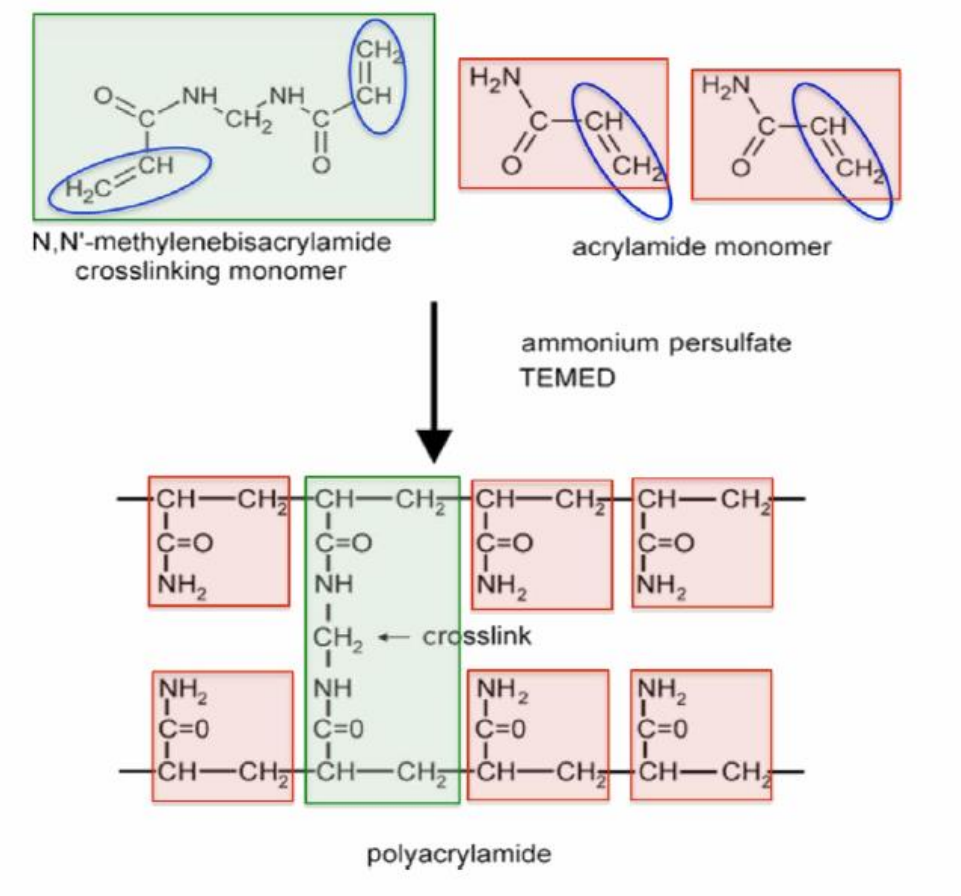

Figure 1.17 Cross-linking principle of the monomers by APS and TEMED [70].

1.7 Aim of the study

In this thesis, it was aimed to optimize mechanical, thermal and dielectric properties of (SiO_2-Al_2O_3-CaO based) glass/ceramic/(and nanofiller (hBN, AlN)) composites for functional and structural applications. In a former study [71], CaO-SiO_2-Al_2O_3-based glass (20 to 60 wt%)/Al_2O_3 composites were reported such that 55 wt% glass/Al_2O_3 composites were densified at 850 °C and had a dielectric constant of 7.3 at 5 MHz. However, they had a low thermal conductivity of 1.31 W/m·K at 75ºC (and a mean value of 1.23 W/m·K between 75 °C and 250 °C). In our study, therefore, the composite composition was engineered in order to improve properties together such as high thermal conductivity and low dielectric constant without increasing densification temperature above 950 °C. For this purpose, mullite as the replacement for Al_2O_3 as well as addition of nano fillers (e.g., platelet-shaped nano hBN particles or nano AlN powders) were primarily considered. Densification, phase formation, microstructure evolution, mechanical properties (hardness, flexural strength, elastic constant), dielectric properties (dielectric constant and loss) and thermal properties (thermal conductivity, thermal expansion coefficient) were investigated as a function of glass content (10 to 60 wt%), nano filler content (1 to 10 wt%) and crystalline phases (mullite or Al_2O_3). The results were evaluated to comply with some potential structural and functional applications such as low temperature co-fired ceramics and radome, and were compared with the literature and commercial products. It is particularly important to establish a national infrastructure to decrease/eliminate foreign dependency on critical ceramic systems and components.

CHAPTER 2

EXPERIMENTAL PROCEDURE

Spray-granulated alumina (Al_2O_3, CT3000SG, Almatis, purity 99.78%, ρ=3.96 g/cm^3), mullite ($3Al_2O_3.2SiO_2$, Nabaltec, 90-95 % mullite+5-10 % glassy phase+1 % Al_2O_3, ρ=3.13 g/cm^3), a commercial glass ($CaO-Al_2O_3-SiO_2$ based, Akkim), hexagonal boron nitride powder (hBN, Nanografi, ρ=2.1 g/cm^3, 65-75 nm, SSA=30-35 m²/g) and aluminum nitride powder (AlN, nanografi, ρ =3.26 g/cm^3, particle size 65-75 nm, SSA=50 m^2/g) were used as starting materials. A binder burn-out was performed at 600 °C for 30 minutes to remove binder from Al_2O_3 powder to be used for colloidal methods. The glass frit was first ground using a mortar and pestle. Then, it was ball milled in ethanol using ZrO_2 balls for 48 hours.

In the first step, property improvement due to nano hBN filler was checked using 55 wt% glass and 45 wt% Al_20_3 mixture (hereafter abbreviated as A55), based on a previous study [71]. A powder mixture consisting of Al_2O_3 and glass were ball-milled using ZrO_2 balls in ethanol for 24 h and then dried at 100 °C. The A55 was then mixed with hBN at various proportions and then ball milled for another 24 h in ethanol. The composites will hereafter be referred to as A55-1, A55-2.5, A55-5 and A55-10 which corresponds to 1, 2.5, 5 and 10 wt% hBN, respectively. The green samples, formed by dry pressing (added dispersant as 2 wt% of total powder) at 100 MPa, were sintered on Al_2O_3 substrates at various temperatures in the range of 800–900 °C for 1 h in air with a heating and cooling rate 5 °C/min. In addition, various forming methods such as cold isostatic pressing at 250 MPa and by tape casting were applied in order to understand the effect of platelet-shape hBN particles on densification. For tape casting experiments, powders were dispersed using a ready-to-use vinyl-based commercial binder solution (MSE Teknoloji, Türkiye) at a solid:solution mass ratio of 60:40. Polymer ratio in solution was 17.65 wt% for the A55, A55-1, A55-2.5, A55-5 slurries and 25 wt% for the A55-10 slurry. The slurries were prepared using a speed mixer (FlackTek, DAC 150.1 FVZ) at 3500 rpm for 10 min and then casted on a silicon coated Mylar film at a casting rate of 5 cm/s with a blade gap of 250 μm. After drying

at 25 °C for 1 h, green tapes were cut into desired size and laminated at 80 °C by applying 20 MPa for 10 minutes. The green samples were binder burn-out at 600 ˚C for 30 min with a slow heating rate of 1 ˚C/min and cooling rate was 2 ˚C/min. After binder burn-out process, composites were sintered on mullite substrates at various temperatures between 800 °C and 900 °C for 1 h with a heating rate 5 °C/min.

For the mullite/glass composites, glass powder was mixed with mullite at mass ratios (wt%) of 10, 20, 30, 50, 55, and 60 by ball milling for 24 h in ethanol with a binder solution (added as 2 wt% of total powder) and then dried at 100 °C. The mullite glass composites will hereafter be referred to as M10, M20, M30, M50, M55, M60 which corresponds to 10, 20, 30, 50, 55, and 60 wt% glass powder, respectively. The composites were uniaxial dry-pressed at 100 MPa, and then sintered on mullite substrates at various temperatures in the range of 750-1600 °C for 1 h with a heating and cooling rate 5 °C/min in air, depending on the glass content. The mullite/glass/hBN composites (hereafter referred to as M55, M55-1hBN, M55-2.5hBN, M55-5hBN, and M55-10hBN which corresponds to 0, 1, 2.5, 5 and 10 wt% hBN, respectively) and mullite/glass/AlN composites (hereafter referred to as M55, M55-1AlN, M55-2.5AlN, M55-5AlN and M55-10AlN which corresponds to 0, 1, 2.5, 5 and 10 wt% AlN, respectively) were fabricated by tape casting method as described above. The mass ratio of solid to binder solution was set to 60:40 for the M55, 50:50 for the M55-1 AlN and M55-2.5 AlN and 47.5:52.5 for the M55-5 AlN and M55-10AlN composites. The flowchart of the experimental studies is shown in Figure 2.1.

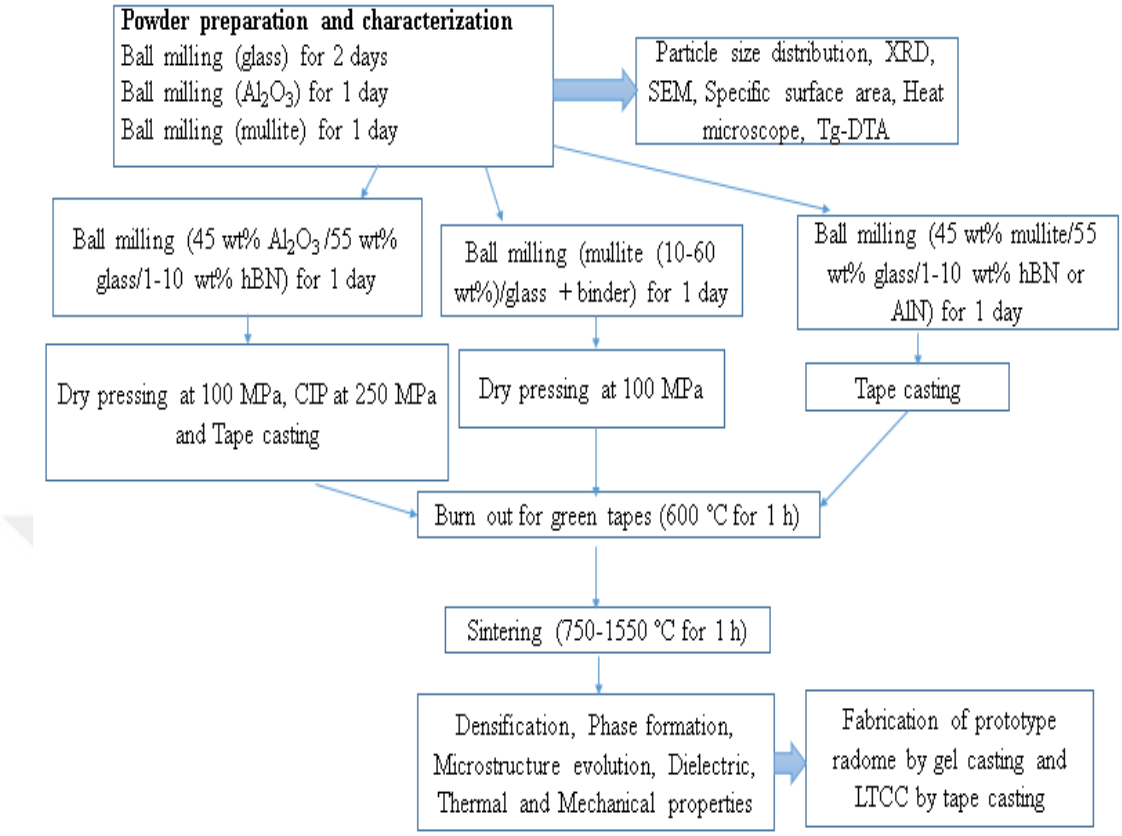

Figure 2.1 Flowchart of the experimental procedures

Bulk densities of the sintered samples were determined from the Archimedes' method. The bulk density was calculated, according to Equation 2.1. Apparent porosity (AP, %) and water absorption (WA, %) values were calculated according to the Equation 2.2 and Equation 2.3, respectively.

$$Bulk\ density = \left[\frac{Ms}{Ww-Ws}\right] \times \mathrm{d} \tag{2.1}$$

$$\mathrm{AP\%} = \left[\frac{\mathrm{Ww-Ms}}{\mathrm{Ww-Ws}}\right] \times 100 \tag{2.2}$$

$$\mathrm{WA\%} = \left[\frac{\mathrm{Ww-Ms}}{\mathrm{Ms}}\right] \times 100 \tag{2.3}$$

where Ms is the sintered dried mass (g), Ws is the weight of sample in water (suspended weight) (g), Ww is the weight of sample impregnated with water (g), d is the density of water (~ 1 g/cm^3). The thermal behaviour of commercial glass frit was

measured by a heating microscope (Misura 3.32). The particle size of glass powder was determined by a laser diffraction particle size analyzer (Malvern, Mastersizer 3000). Specific surface area was determined by BET method (Quantachrome ASiqwin). Phase formation was checked by XRD (Rigaku, Miniflex600) with Cu/Kα radiation and a scan rate of 2 °C/min. Microstructure evolution was observed by a Scanning Electron Microscopy and Energy Dispersive Spectrometry (EDS), respectively (SEM, Hitachi SU5000).

The hardness and fracture thoughness of the sintered composites were determined by Micro Vickers hardness tester (Shimadzu HMV-G) by applying 20 N for 10 seconds. Vickers hardness was calculated according to ISO 6507-1:2005 standard from the following formula;

$$H = 0.1891 \frac{P}{a^2} \tag{2.4}$$

where H is Vickers hardness, P is test force (N) and a is average length of diagonal lines of the indentation (mm). Fracture toughness was calculated using the formula given by Lawn et al.[72]:

$$K_c = \delta \frac{\sqrt{E \,.\, P}}{\sqrt{H}.\ \sqrt{C^3}} \tag{2.5}$$

where K_c is fracture toughness (MPa/√m), E is Elastic modulus (MPa), c is half of the average crack length (m), a is half of the average length of indentation diagonal lines (m), and δ is a non-dimensional constant which is primarily a function of the indenter geometry. It was given as 0.026 for the hardness tester used. Composites for flexural strength and elastic modulus measurements were produced by dry pressing at 100 MPa and tape casting (green tapes were kept at 80 °C for 30 minutes and then laminated by applying 50 MPa for 10 minutes) at nearly 3x4x50 mm dimensions. Five samples from each set were prepared. Then, the composites were sintered at optimum sintering temperature for each composite. The flexural strength was determined by a 3-point bending test (40 mm span length and 0.5 mm/min crosshead speed) using a universal tester (Instron 5569, 500 kg load cell) and calculated according to ASTM standard C1161-18 from the following formula;

$$S = \frac{3\,.\,P\,.\,L}{2\,.b\,.\,d^2} \tag{2.6}$$

where P is break force (N), L is support span (mm), b is specimen width (mm), and d is specimen thickness (mm). Elastic modulus was determined by a resonance frequency method using a Grindo Sonic system (Grindo Sonic MK5). Elastic modulus was calculated according to ASTM standard C1259-15 from the following formula;

$$\mathrm{E} = 0.9465.\,(\mathrm{m}\,.\,\mathrm{f}^2{}_{\mathrm{f}}/\mathrm{b}).\,(\mathrm{L}^3\,/\mathrm{t}^3).\,\mathrm{T}_1 \tag{2.7}$$

$$\mathrm{T}_{1\,=}\,1 + 6.585\,.\,(1 + 0.2023\,.\,\mu + 2.173\,\mu^2)\,.\,(\mathrm{t/L})^2 - 0.868\,(\mathrm{t/L})^4 - \left[\frac{8.34\,.\,(1 + 0.2023\,.\,\mu + 2.173\,\mu^2\,(\mathrm{t/L})^4)}{1 + 6.338.\,(1 + 0.1408\,.\ \mu + 1.536\,\mu^2\,).\,(\mathrm{t/L})^2}\right] \tag{2.8}$$

where E is elastic modulus (Pa), m is mass of the bar (g), b is the width of the bar (mm), L is the length of the bar (mm), t is the thickness of the bar (mm), f_f is fundamental resonant frequency of the bar (Hz), and μ is Poisson's ratio. The statistical analysis of flexural strength was conducted by using Weibull approach. Probability of failure (P) vs. failure stress (S) curve was first drawn. Then, a linear fit was applied to the data points. The characteristic strength (σ) was finally calculated as [73];

$$\sigma\ = \mathrm{e}^{\mathrm{c/m}} \tag{2.9}$$

where m is slope of the curve and c is the constant variable in the linear equation of y=mx+c. A general simple method was used to determine thermal shock resistance (R) (see Equation 1.4 and 1.5) [74]

The dielectric properties were measured using an impedance analyzer (Agilent, 4294A) at 5 MHz and then the dielectric constant K was calculated according the following formula;

$$\mathrm{K} = \frac{C.d}{\varepsilon_0\,.A} \tag{2.10}$$

where C is capacitance (F), d is thickness of specimen (m), ε_0 is permittivity of vacuum (F/m) and A is area of electrode (m^2). A network analyzer (Rohde&Schwarz ZNB40) was used to calculate the dielectric constant between 4 and 10 GHz.

Thermal analysis of the hBN and AlN powders were investigated by differential thermal analysis and thermogravimetric analysis methods (HITACHI STA 7300) up to 1300 °C at heating and cooling rates of 10 °C/min in air. Thermal conductivity was measured at room temperature using a single-sided testing configuration (Hot Disk, TPS 3500). Thermal expansion coefficient of the sintered composites (at dimensions of 5x5x25 mm) were measured using a dilatometer (NETZSCH DIL 402 PC) at a heating rate of 10 °C/min in the temperature range of 25–800 °C for each sample.

The optimum compositions were used to prepare LTCC and radome prototypes. Tape casting method was used to prepare LTCC prototypes and the same procedures were followed as mentioned above. A manual screen printer (LPKF ProtoPrint S RP) with 120 silk mesh was used for Ag printing on single green sheets. The green tapes with/out electrodes were hot laminated at 80 °C applying 20 MPa for 10 min for each side. Because radomes are large and 3D products, they were fabricated by gel casting method. Powder mixture, monomer solution (mixing acrylamide (AM) and methylenebisacrylamide (MBAM)), ammoniumpersulfate (APS) ($(NH_4)_2S_2O_8$, Sigma-Aldrich), and tetramethylenediamine (TEMED) ($C_6H_{16}N_2$, Sigma-Aldrich) were used to prepare gel cast slurries. Firstly, powder mixture, dispersant (ammonium salt of polyacrylic acid, Coatex P90, added as 2 wt% of the total powder weight) and monomer solution (14 wt %) were mixed at 3500 rpm for 5 minutes. Then, APS solution (3 wt %) added and mixed at 3500 rpm for 5 minutes. Finally, TEMED was admixed at 1000 rpm for 15 seconds. Then, the slurries were poured into aluminum foil molds. Prior to being demolded, samples were cured at ambient temperature and then dried slowly to prevent crack formation. In other words, the samples were heated from 40 ˚C to 70 ˚C with 5 ˚C increments at every 12 hours in a drying oven. Then, the samples were cooled to the 25 ˚C. The polymer in the green samples were burn-out at 600 ˚C for 1h with a slow heating rate of 1 ˚C/min and cooling rate was 2 ˚C/min. Finally, the green samples were green-machined and then sintered.

CHAPTER 3

POWDER CHARACTERIZATION

A commercially available glass frit was used as the starting material. The glass frit was first crushed with a mortar and pestle and then ball milled for 48 hours in ethanol using ZrO_2 balls to obtain fine glass powder. The glass frit had d_{50}=2.13 μm and d_{90}=3.91 μm, SSA = 1.89 m^2/g after milling. SEM microstructure, XRD phase analysis and particle size distribution of the ground glass powder are shown in Figure 3.1. Figure 3.1 (a) demonstrates SEM image of the glass particles with angular shapes. Figure 3.1 (b) shows XRD pattern of glass powder that has amorphous in nature except for a small peak belonging to quartz phase (Card number: 00-009-0466). Figure 3.1 (c) indicates a unimodal particle size distribution with a d_{10}=1.16 μm d_{50}=2.13 μm and d_{90}=3.91 μm. Stable oxide composition for each element was calculated based on the EDS results and given in Table 3.1. The main components in the glass powder were SiO_2, Al_2O_3, and CaO. Based on the EDS results, the crystallization was expected to be in anorthite phase ($CaO.Al_2O_3.2SiO_2$ or $(Ca,Na)(Si_2Al)_4O_8$). SiO_2 was the network former, Al_2O_3 was the intermediate and CaO, Na_2O, and K_2O were the modifiers in the glass [5].

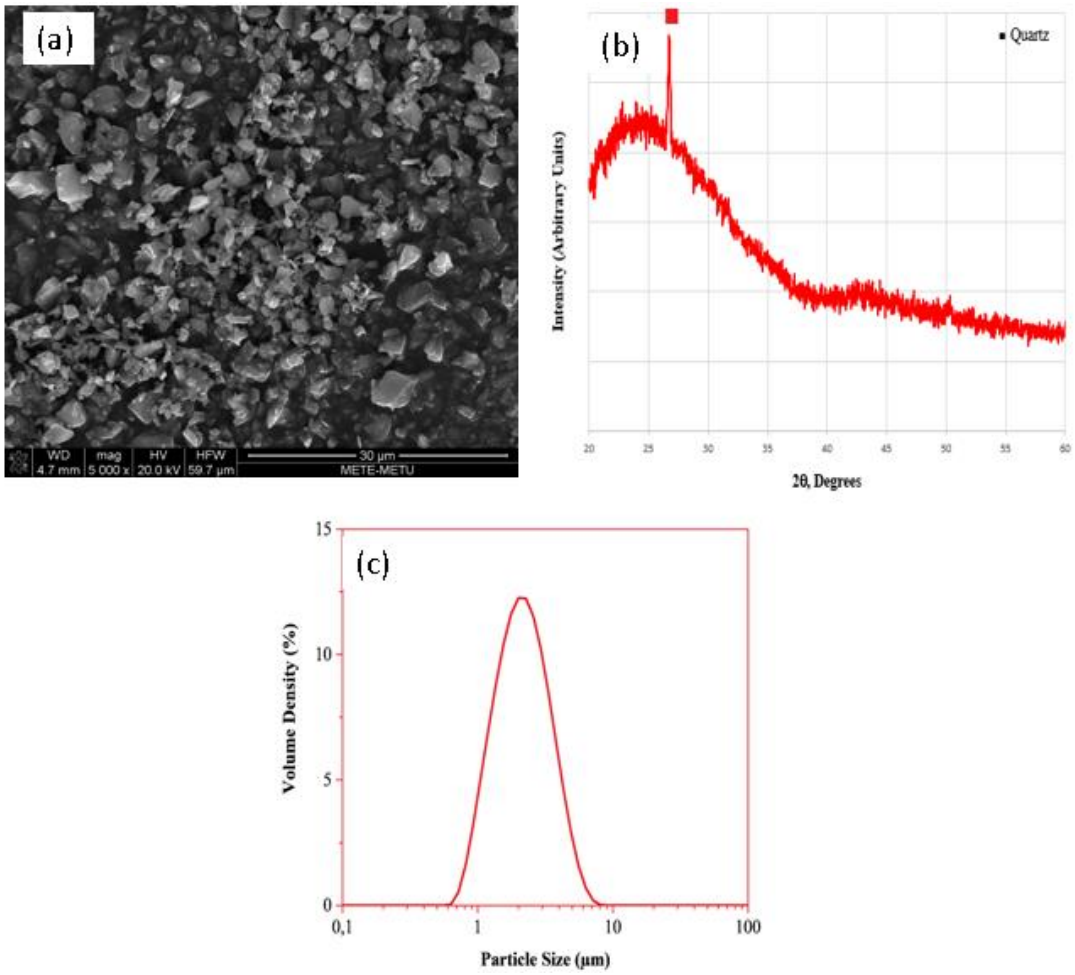

Figure 3.1 (a) SEM image; (b) XRD pattern; (c) Particle size distribution of glass powder

Table 3.1 Stable oxide composition of the glass powder

Composition	SiO_2	Al_2O_3	CaO	Na_2O	K_2O
wt. %	65.7	15.6	10.7	4.8	3.2

Heating microscope result of the glass pellet, prepared from ground glass powder, is given in Figure 3.2. Sintering, softening and melting temperatures were determined as 726 °C, 852 °C, 1104 °C, respectively. Glass pellets sintered at 750 °C, 775 °C, 800 °C, 850 °C, 950 °C are also shown as an inset in Figure 3.2. It is evident that the sintering results are compatible with the heating microscope results.

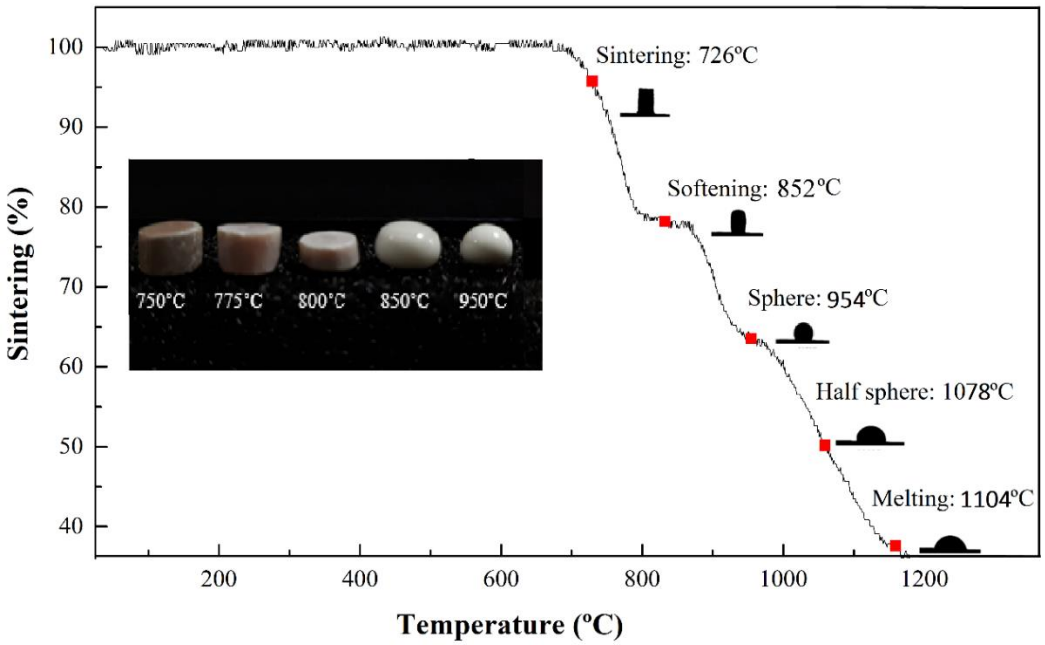

Figure 3.2 Heating microscope results of the glass powder. Inset shows glass pellets sintered at 750 °C, 775 °C, 800 °C, 850 °C, 950 °C.

Figure 3.3 shows backscattered SEM images of the glass pellets heated at 750 °C and 825 °C. Irregular pore shapes seen in Figure 3.3 (a) reveal an incomplete densification; however, spherical pore shapes seen in Figure 3.3 (b) indicate completion of sintering.

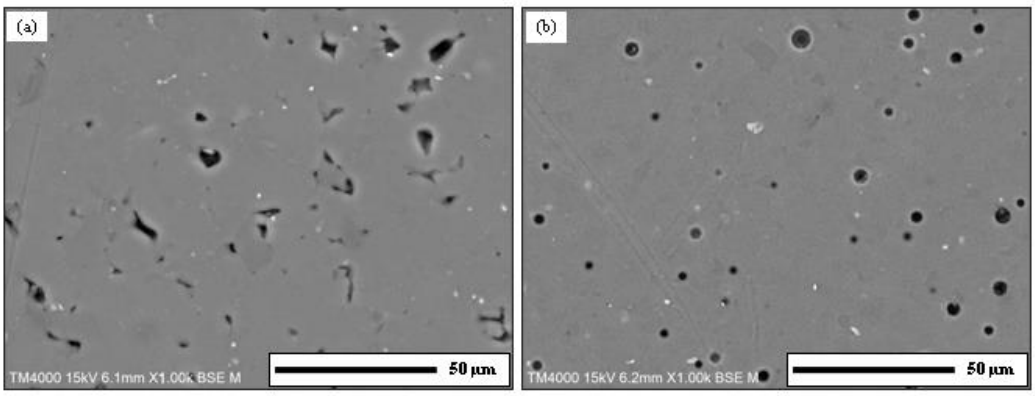

Figure 3.3 Backscattered SEM images of glass pellets; heated at (a) 750 °C and (b) 825 °C.

Figure 3.4 shows XRD patterns of the as-received and heat-treated glass powders at 825 °C. The glass powder did not show any crystallization with increasing temperature

except for a small quartz peak at 2θ=26.77° (Card number: 00-009-0466) present in both powders. The presence of quartz may be due to incomplete vitrification during fabrication. Heat treatment significantly reduced the background that tended to crystallize.

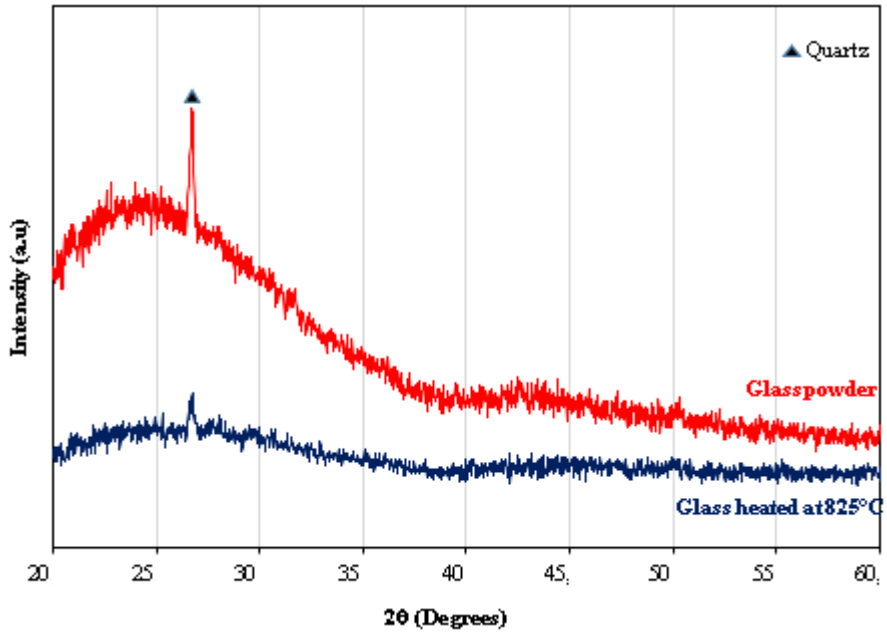

Figure 3.4 XRD patterns of the glass powder and heat-treated powders at 825 °C.

Table 3.2 shows properties of spray-granulated Al_2O_3 powder. First, Al_2O_3 powder was subjected to burnout process at 600 °C for 30 min to remove polymer and then ball-milled for 24 h to decrease particle size for colloidal processing. Figure 3.5 shows particle size distribution of Al_2O_3 powder that was slightly bimodal. After ball milling, Al_2O_3 powder had a d_{10}=0.19 μm, d_{50}=0.44 μm, d_{90}=1.17 μm and SSA=6.44 m^2/g. A relatively lower d_{50} after ball milling could cause slight agglomeration that lowered specific surface area.

Table 3..2 The properties of Al_2O_3 powder [75]

Properties	Values
Specific surface area (m^2/g)	7.5
Specific density (g/cm^3)	3.9
Chemical composition	99.78% Al_2O_3 0.03% SiO_2 0.02% Fe_2O_3 0.02% CaO 0.07% MgO 0.08% Na_2O
d_{50}, μm	0.5

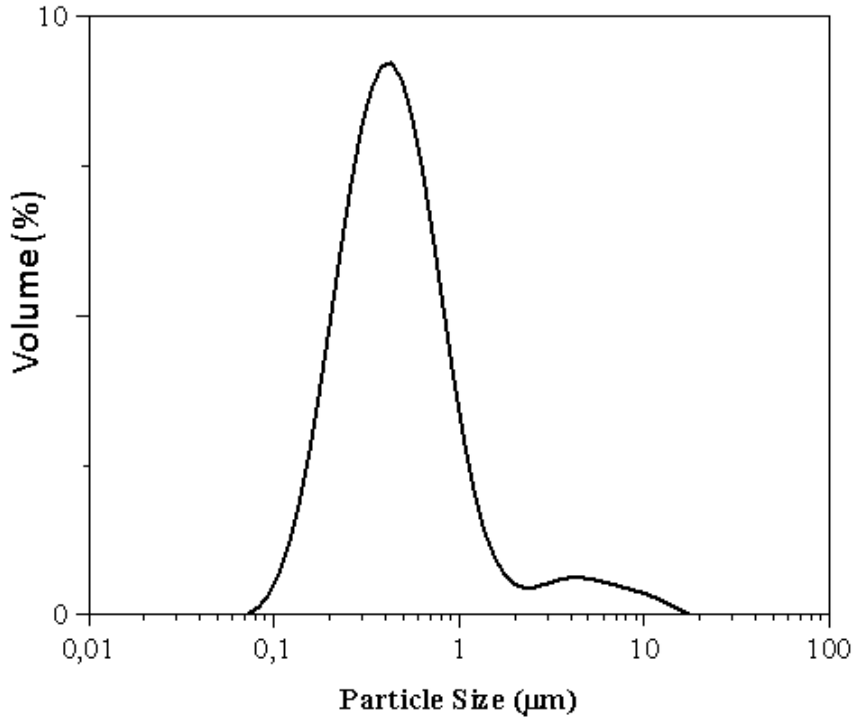

Figure 3.5 Particle size distribution of Al_2O_3 powder after ball milling for 24 hours.

Mullite ($3Al_2O_3.2SiO_2$) was used as starting material. The properties of as-received mullite is shown in Tables 3.3. Because mullite was produced by quenching method, it was ball-milled to reduce particle size required for dry-pressing and colloidal processing. After ball milling, mullite powder had a d_{10}=0.17 μm, d_{50}=0.34 μm,

d_{90}=1.21 μm and SSA=2.89 m²/g. Figure 3.6 shows that its particle size distribution was slightly bimodal. The d_{50} was significantly reduced by ball milling from 3-5 μm to 0.34 μm.

Table 3.3 Properties of as-received mullite [76]

Properties	Values
Mineralogical composition	90-95 % mullite 5-10 % glassy phase 1 % Al_2O_3
Specific density (g/cm^3)	3.13
Chemical composition	72% Al_2O_3 26% SiO_2 0.3% Fe_2O_3 0.2% TiO_2 0.05% CaO 0.1% MgO 0.2% Na_2O 0.6% K_2O
d_{50}, μm	3-5

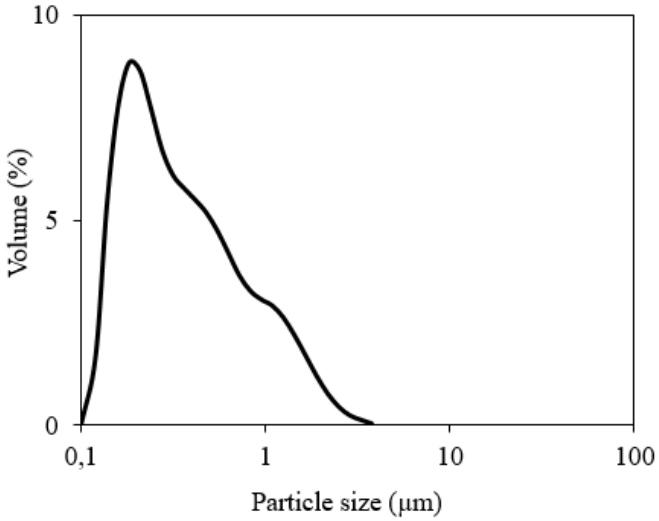

Figure 3.6 Particle size distribution of mullite powder after ball milling for 24 hours.

Commercial hBN and AlN nano powders were added as filler materials to the composites. hBN powder had an SSA of 30-35 m^2/g, and averaged particle size of 65-

75 nm, AlN powder had an SSA of 50 m^2/g and averaged particle size of 60-70 nm. TG-DTA graphics of hBN and AlN are given in Figures 3.7 and 3.8, respectively. The TG-DTA analysis indicated that hBN and AlN powders started oxidizing at 1019 °C and 1174 °C in air (i.e., >950 °C), respectively, which is critical for the LTCC applications from the thermal and dielectric properties point of view.

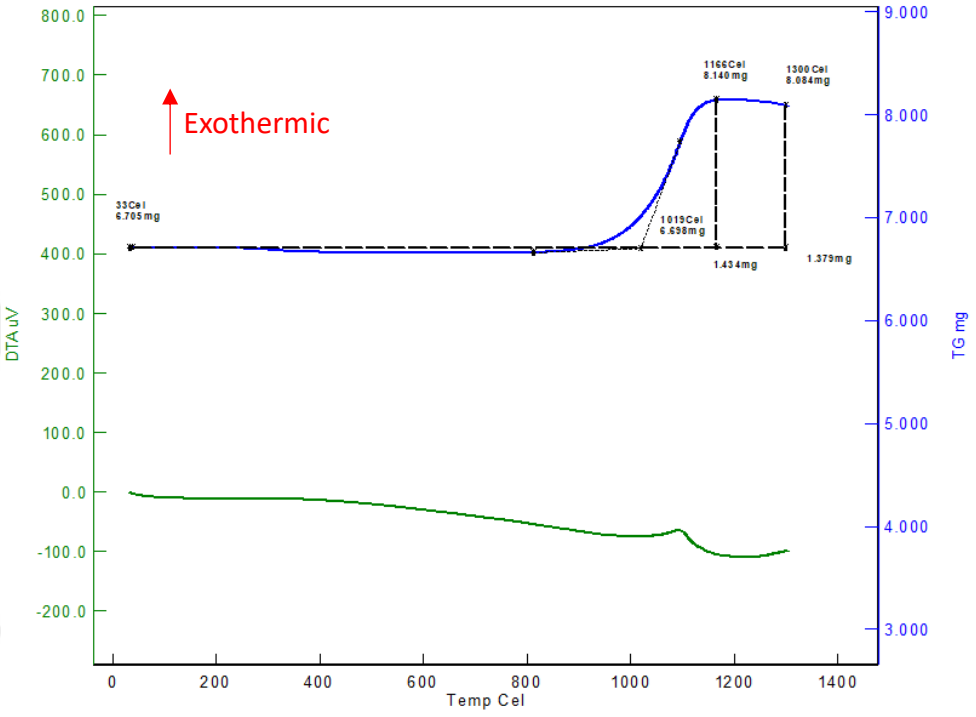

Figure 3.7 TG-DTA graphic of hBN powder

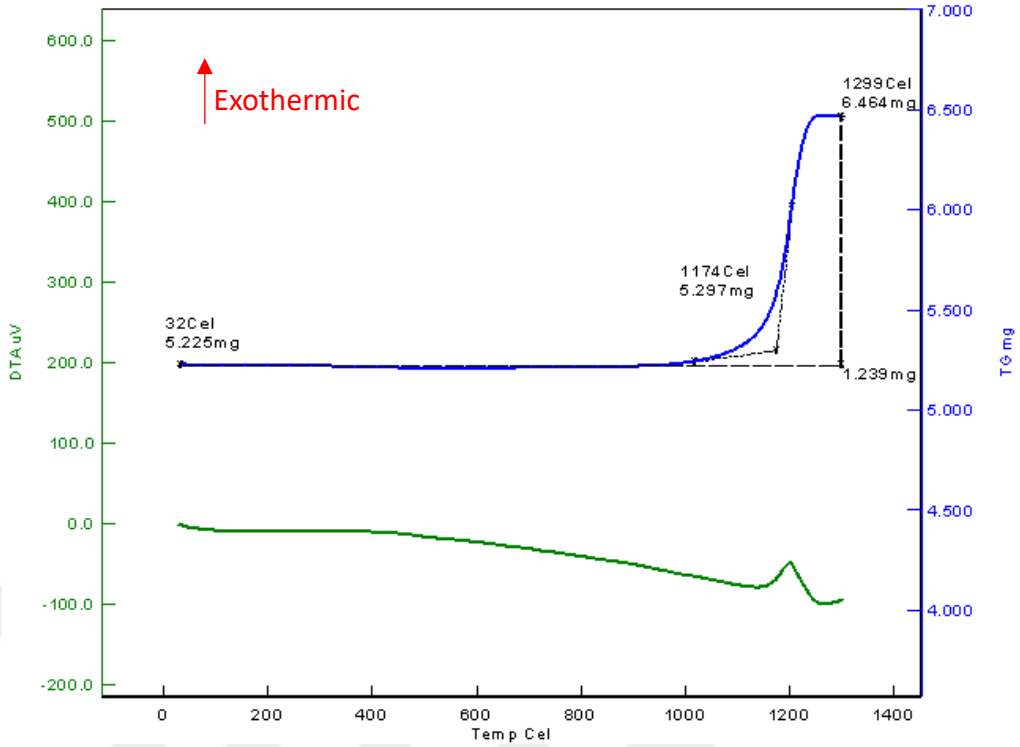

Figure 3.8 TG-DTA graphic of AlN powder

Al_2O_3, mullite and glass powder were processed separately and made ready for direct usage. hBN and AlN nano powders were purchased and used as-received. Table 3.4 shows dielectric, thermal and mechanical properties of Al_2O_3, mullite, glass, hBN and AlN ceramics. Anisotropic properties of hBN was taken from textured hBN-based ceramics because of the lack of pure hBN ceramic or single crystal data.

Table 3.4 Mechanical, thermal, dielectric properties of Al_2O_3, mullite, glass, hBN and AlN

Materials	Flexural strength (MPa)	Elastic modulus (GPa)	CTE (ppm/°C)	Thermal conductivity (W /m·K)	Dielectric constant	Dielectric Loss
Al_2O_3	411 [37]	390[37]	8.8 (0-1000 °C)[28]	36[37]	9.6 (25°C, 10-40 GHz)[63]	0.0001 (10 GHz)[63]
Mullite [77]	190	91-220	4.5 (20-1000ºC)	6.07	6.6 (1-40 GHz)	<0.001 (10-40 GHz)
Glass	87[28]	70[28]	0.55[28]	0.85[38]	6.37[71]	0.0016[71]
hBN	~ 82-138 //c, ~18-34 ⊥c [78][79]	~ 62-82 //c, ~ 8-25 ⊥c [78][79]	~ 2.3-2.4 ⊥c, ~11.3-15.6 //c (100-1200 °C) [78][79]	~20-23 //c, ~ 111-137 ⊥c [78][79]	4.5 (1-10 GHz) [80]	0.0003 (10 GHz) [80]
AlN	320[81]	300-350[81]	4.5-5 (25-400°C)[81]	320[81]	8.6-9.2[82]	0.05-0.001 [82]

⊥c: perpendicular to the c-axis, //c: parallel to the c-axis

CHAPTER 4

MECHANICAL, THERMAL AND DIELECTRIC PROPERTIES OF Al_2O_3/GLASS/hBN COMPOSITES

In a former study [71], CaO-SiO_2-Al_2O_3-based glass (20 to 60 wt%)/Al_2O_3 composites were reported such that 55 wt% glass/Al_2O_3 composites were densified at 850 °C and had a dielectric constant of 7.3 at 5 MHz. However, they had a low thermal conductivity of 1.31 W/m·K at 75ºC (and a mean value of 1.23 W/m·K between 75 °C and 250 °C). In this chapter, therefore, this composition was further engineered to improve thermal properties without increasing densification temperature and degrading other properties. Nano hBN filler was added at 1 (A55-1), 2.5 (A55-2.5), 5 (A55-5) and 10 (A55-10) wt% to the base 55 wt% glass/Al_2O_3 composite (A55) because hBN has high thermal conductivity and low dielectric properties (Table 3.4).

4.1 Densification

Densification and apparent porosity (AP) values of the dry-pressed samples as a function of hBN amount and temperature are given in Figure 4.1. The solid lines are drawn to guide eye. Generally, as the hBN amount was increased, bulk densities of the composites decreased for each sintering temperature due to hBN lower density (hBN=2.1 g/cm^3 [83]) with respect to Al_20_3 (3.93 g/cm^3 [71]) and glass (2.43 g/cm^3 [71]). Furthermore, the AP decreased with increasing densification. The bulk densities of the A55-10 were the lowest for each temperature. The densification temperatures for each composite were first compared among themselves based on the lowest AP and water absorption (WA) calculated from the Archimedes' method. The highest densification was obtained at 800 ºC for the A55 (2.89 g/cm^3, AP=0.13% and WA=0%), the A55-1 (2.81 g/cm^3, AP=0.17% and WA=0.16%), the A55-2.5 (2.75 g/cm^3, AP=0.23% and WA=0.08%), and at 900 °C for the A55-5 (2.48 g/cm^3 and AP=0.05% and WA=0.02%) and the A55-10 (2.28 g/cm^3, AP=14.87% and WA=6.51%). The A55-5 and A55-10 samples had relatively low densities despite being sintered at high temperatures. They were then produced by cold isostatic

pressing (CIP) and tape casting to further improve densification of the composites. Densification and AP behaviors of the composites produced by different methods are compared in Figure 4.2. The bulk densities for the A55-5 and A55-10 composites produced by the CIP method were 2.54 g/cm^3 and 2.28 g/cm^3, respectively. The bulk densities for the A55-5 and the A55-10 composites produced by the tape casting method were 2.65 g/cm^3 and 2.45 g/cm^3, respectively. Note that the AP decreased to 0.91% and 0.32% with the WA of 0.46% and 0.13% for the A55-5 and A55-10 samples produced by tape casting method, respectively. On the other hand, the densification temperature of the A55-5 sample was successfully reduced from 900 °C to 800 °C by changing the fabrication method from dry pressing to tape casting. These results are an advantage of the colloidal processing method, which allows addition of a high amount of hBN to the Al_2O_3/glass structure and allows homogeneous dispersion of the plate-like hBN particles. Relative density for each composition was found by dividing bulk density to theoretical density as-calculated using logarithmic mixing rule [84]. The relative densities of the A55, A55-1, A55-2.5, A55-5 and A55-10 were 98.64%, 96.24%, 94.83%, 92.34% and 87.19%, respectively. Although the AP and WA values were very close to zero, lower (bulk) relative densities with increasing hBN content might be attributed to the increased numbers of closed pores (closed porosity, CP=total porosity-AP), that is, total porosity (i.e., 100-relative density) was 1.36% (AP=0.13%, CP=1.23%) for the A55 (800°C), 3.76% (AP=0.17%, CP=3.59%) for the A55-1 (800°C), 5.17% (AP=0.23%, CP=4.94%) for the A55-2.5 (800°C), 7.66% (AP=0.91%, CP=6.75%) for the tape-cast A55-5 (800°C) and 12.81% (AP=0.32%, CP=12.49%) for the tape-cast A55-10 (900°C). It is evident that the CP increased significantly from 1.23% for the A55 to 12.49% for the A55-10, although the AP varied slightly between 0.13% and 0.91%. Similar effects of hBN particles on densification have been reported in the literature for barium aluminasilicate ($BaAl_2Si_2O_8$, BAS)/hBN (10 to 50 wt%) composites produced by hot pressing at 1500 °C [85]. The bulk density decreased from 3.18 g/cm^3 at 10 wt% hBN without visible micro cracks to 2.22 g/cm^3 at 50 wt% hBN with cracks and voids. Similar results were reported by Cho et al. [86] such that the plate-like hBN in the AlN (5-20 vol%)-hBN ceramics triggered the formation of porosity, resulting in limited densification.

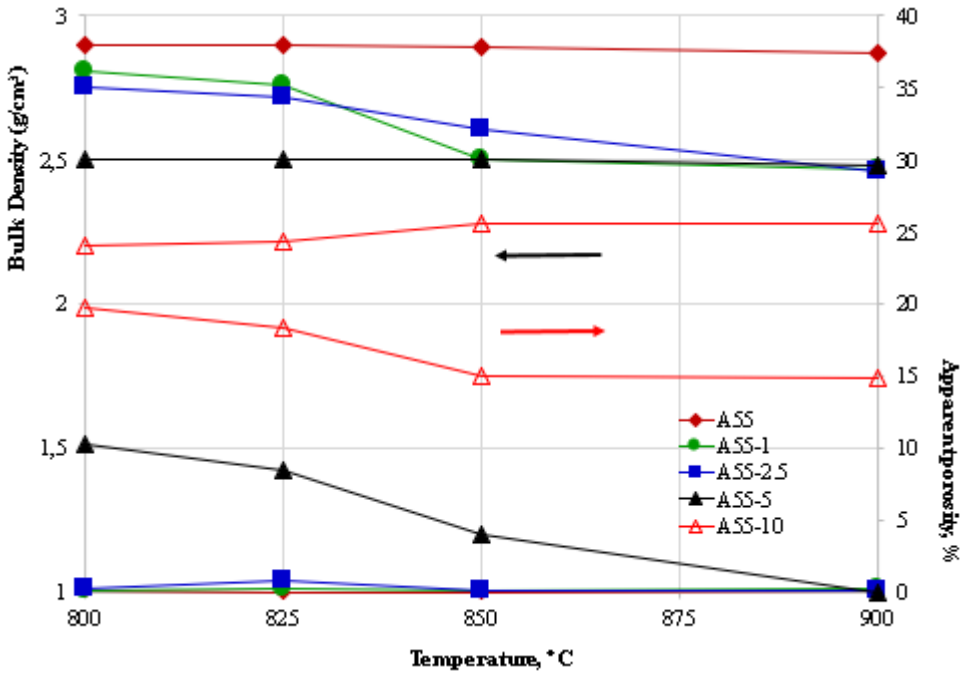

Figure 4.1 Densification of the samples as a function of hBN content and temperature

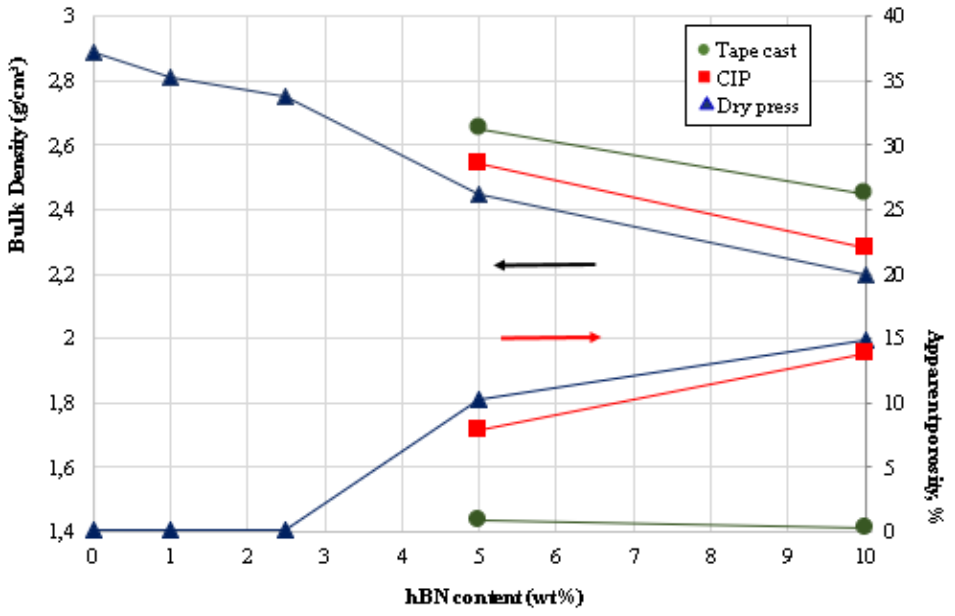

Figure 4.2 Densification of the samples fabricated via different methods and sintered at 800 °C (for the A55, A55-1, A55-2.5 and A55-5) and 900 °C (for the A55-10)

4.2 Phase Formation and microstructure evolution

The XRD results of the composites sintered at optimum sintering temperature are shown in Figure 4.3. Al_2O_3 (Card number: 00-010-0173, Corundum) was the main crystalline phase for each XRD pattern. Anorthite $(Ca,Na)(Si,Al)_4O_8$ (Card number: 00-041-1481) and hBN (Card number: 01-074-1977) phases are also marked on the patterns. The hBN peak intensity increased with the initial hBN amount, which proves that hBN neither chemically reacted with other phases nor decomposed with temperature. The chemical stability of the hBN phase is extremely critical at helping decrease dielectric constant and increase thermal conductivity of the composites. Anorthite phase did not form except for the A55-10. Figure 4.4 compares phase evolution as a function of temperature for the A55-5 samples fabricated by dry pressing and tape casting methods. The most distinguishing feature between them was the orientation of the plate-like hBN particles (i.e., basal plane (0002) located at 2θ~26.7°) during tape casting, which also considerably contributed to lowering densification temperature from 900°C to 800 °C (see Figure 4.2) by inhibiting porosity resulted from mainly hBN agglomeration and/or random packing. Anorthite phase formed and its amount considerably increased with increasing temperature. The intensity ratio of the anorthite peak at 2θ~27.9° to Al_2O_3 peak at 2θ~25.5° (i.e., $I_{Anorthite}/I_{Al2O3}$) were used to qualitatively calculate anorthite ratio with temperature. Note that the main Al_2O_3 peak at 2θ~35.1° was not used due to a background hump (see the glass XRD pattern in Figure 4.3). The intensity ratio is 1.25 for the tape-cast A55-10 sample given in Figure 4.3. The intensity ratio is about 0.04 for both dry-pressed and tape-cast samples sintered at 800 °C (i.e., almost no anorthite formation within the XRD detection limit), 0.73 for the Tape-850 °C and 1.29 for the Tape-900 °C samples. The densification levels also changed with temperature, that is, 2.65 g/cm^3 (RD= 92.34%, AP=0.91% and CP=6.75%) at 800 °C, 2.63 g/cm^3 (RD= 91.63%, AP=0.95% and CP=7.42%) at 850 °C, and 2.49 g/cm^3 (RD=86.75%, AP = 8.71% and CP=4.54) at 900 °C. These results indicate that sintering temperature is important to control both densification and phase evolution, which is critical for dielectric and thermal properties.

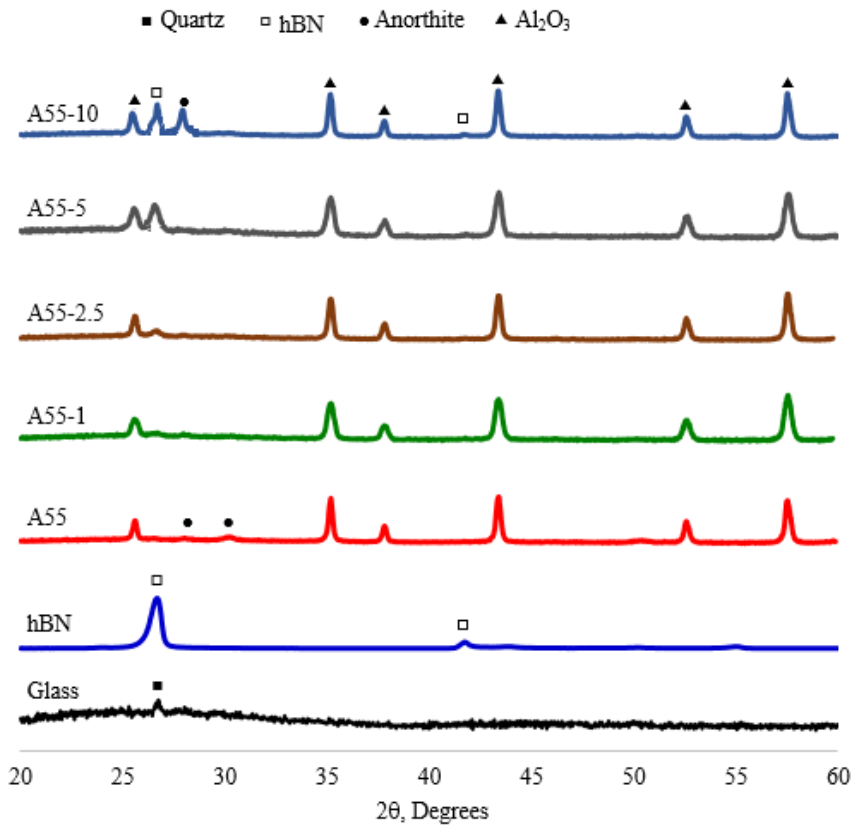

Figure 4.3 XRD patterns of the composites sintered at 800 °C (for the dry-pressed A55, A55-1, A55-2.5 and tape-casted A55-5) and sintered 900 °C (for the tape-casted A55-10)

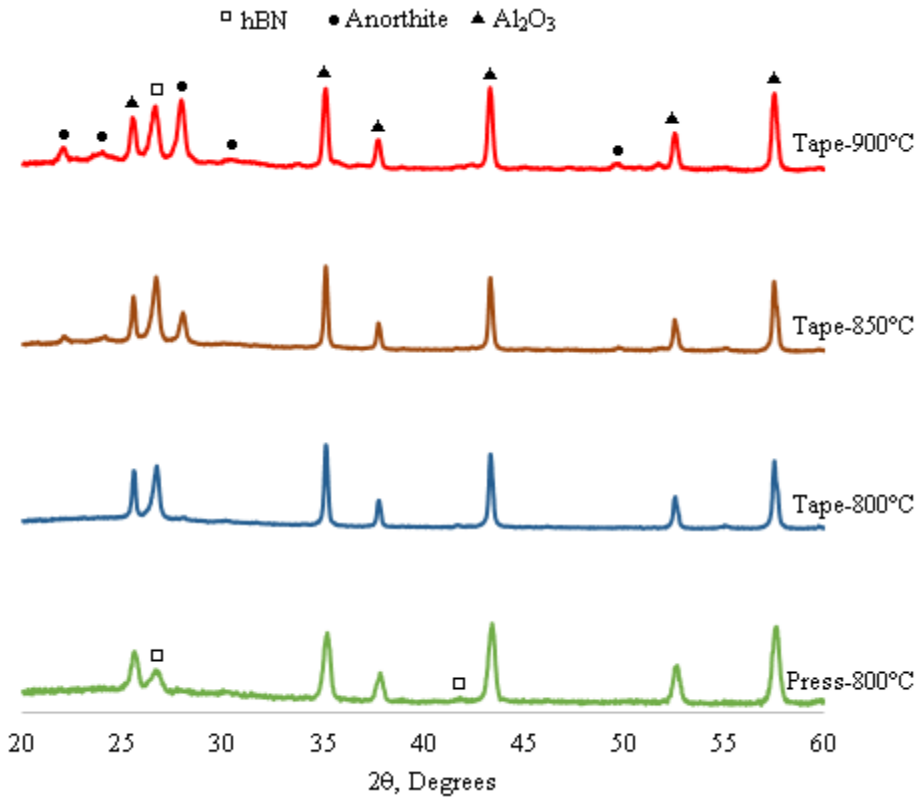

Figure 4.4 XRD patterns of the dry-pressed and tape-casted A55-5 samples sintered at various temperatures

SEM images of the A55, A55-2.5, A55-5 composites sintered at 800 °C and A55-10 sintered at 900 °C are shown in Figure 4.5. As seen in Figure 4.5 (a), Al_2O_3 particles were homogeneously dispersed in the A55 sample without any visible pores. The A55-2.5 and A55-5 produced by dry pressing are shown in Figures 4.5 (b) and 4.5 (c), respectively. It is evident that agglomeration of the plate-like hBN particles resulted in the formation of visible pores in the microstructures. However, as shown in Figures 4.5 (d) and 4.5 (e), the A55-5 and A55-10 samples produced by tape casting had homogeneously dispersed and oriented platelet hBN particles (See also XRD pattern for orientation in Figure 4.4). The arrows indicate orientation of the hBN particles. In addition, the contrast between Al_2O_3 powders and glass matrix fades away with increasing the hBN content. Dense sample preparation by tape casting is critical for LTCC production for both dielectric properties and thermal properties.

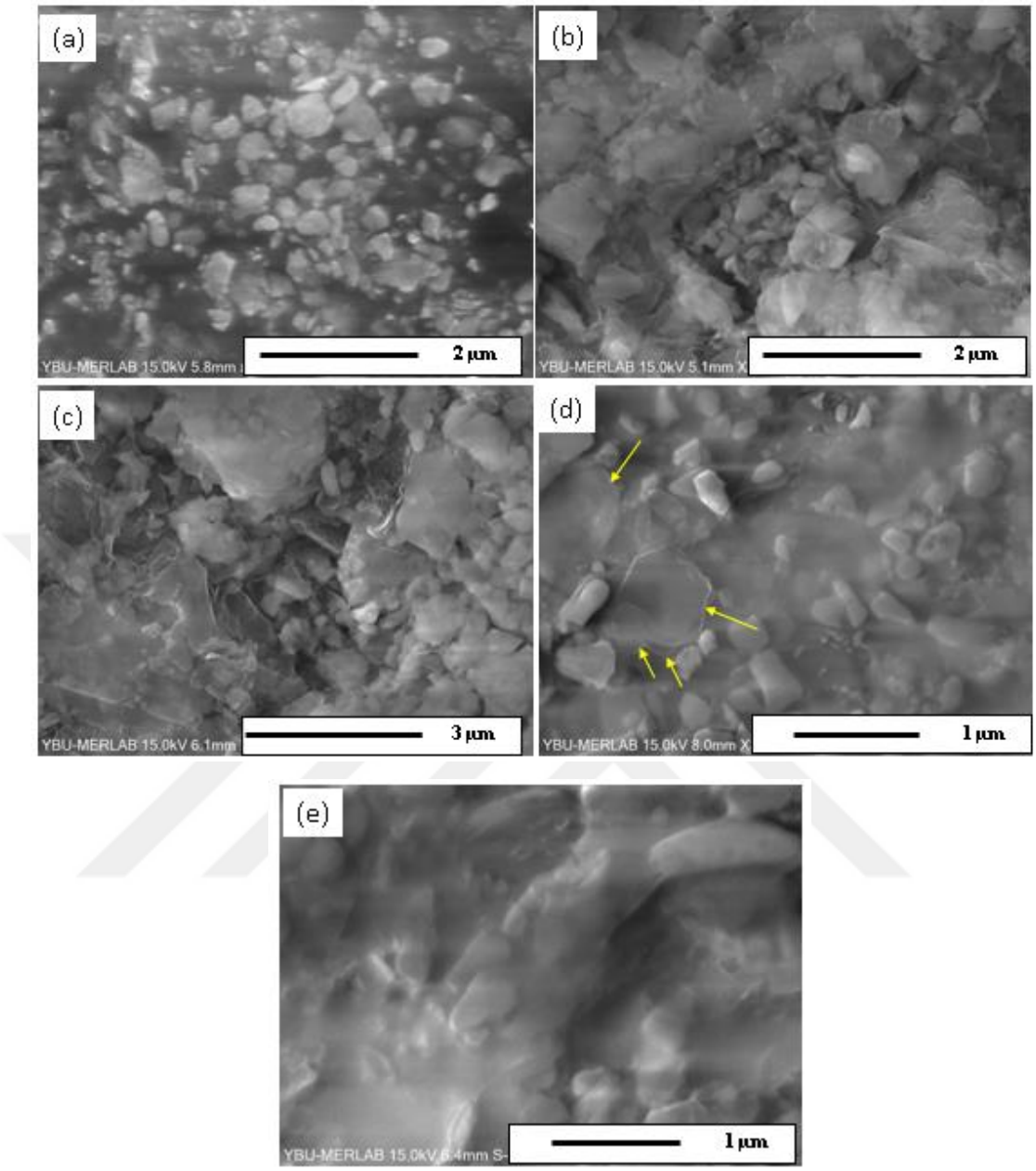

Figure 4.5 SEM pictures of the samples sintered at 800 °C; (a) A55, (b) A55-2.5, (c) dry-pressed A55-5, (d) tape-casted A55-5 (e) tape-casted A55-10 sintered at 900 °C

4.3. Dielectric Properties

Dielectric properties depend on several factors, including densification (or porosity), crystalline phases present, and glass content. The hBN dependence of the dielectric constant (K) and loss measured at 5 MHz for the samples sintered at 800 °C (for the A55, A55-1, A55-2.5 and A55-5) and sintered at 900 °C (for the A55-10) are given in Figure 4.6. The A55, A55-1, and A55-2.5 composites were fabricated by dry pressing,

the A55-5 and A55-10 composites were fabricated by tape casting. Note that K (loss)=10.19 (0.0018) [71] and K (loss)=6.37 (0.0016 [71]) at 5 MHz for Al_2O_3 and glass end compositions, respectively. K decreased with increasing hBN content such that the K values were 7.3 for the A55, 7.2 for the A55-1, 6.6 for the A55-2.5, 6.55 for the A55-5 and 5.57 for the A55-10. Dielectric behavior can be explained based on several parameters such as low K of hBN (i.e., 4–4.4 at 1 MHz [80][83] and 4.5 at 1–10 GHz [63]), amount of closed porosity (i.e., CP=1.23% for the A55, CP= 3.59% for the A55-1, CP=4.94% for the A55-2.5, CP=6.75% for the A55-5 at 800 °C and CP=12.49% for the A55-10 at 900 °C) and also formation of anorthite in the A55-10 (i.e., K (loss)=7.14 (0.0011) and 7.5 (0.0024) at 1 MHz for single crystal and amorphous anorthite[87], respectively). A shallow decrease up to the A55-5 but a strong decrease for the A55-10 suggest that both hBN and closed porosity are mainly responsible for the decrement, but the latter decreases K sharply since K=1 for air [88] although anorthite should increase it for the A55-10. Note that the AP values slightly vary between 0.13% and 0.91% for all compositions.

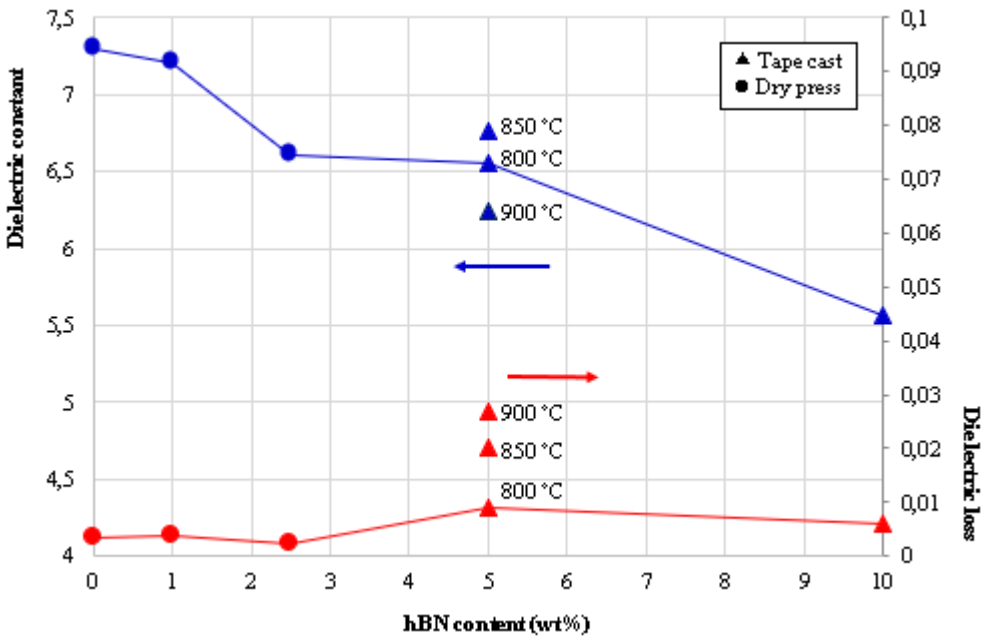

Figure 4.6 Dielectric properties measured at 5 MHz for the samples sintered at 800 °C (for the A55, A55-1, A55-2.5 and A55-5) and sintered 900 °C (for the A55-10)

Figure 4.6 also shows the effect of sintering temperature on K for the A55-5 specimens produced by tape casting. Although both samples had similar density and AP, K slightly increased from 6.55 at 800 ºC to 6.76 at 850 ºC, which may be the result of more anorthite crystallization (e.g., intensity ratio increased from 0.04 to 0.73). For this reason, more anorthite crystallization resulted in higher K. However, the sample sintered at 900 ºC had a lower K=6.24 due to higher AP=8.71%, although it had higher anorthite crystallization (e.g., intensity ratio 1.29). Therefore, porosity (K=1 [88]) tends to decrease and anorthite tends to increase overall K. It has been reported in literature for BN, Si_3N_4, SiO_2 and Al_2O_3 ceramics that porosity reduces K [63]. Similar porosity (or densification) and hBN effects were also observed in hBN/Si_3N_4 composites [89][90]. Complete densification (or near-zero AP) is very important at reducing K in the case of especially limited or without in-situ anorthite crystallization. This is because the signal propagation delay (Equation 1.8) in LTCC electronic packaging is one of the most important parameters directly related to K and a reduction in K is strongly required for high-speed signal transmission [40][52].

Figure 4.6 shows that the dielectric loss was nearly constant up to the A55-2.5 and then increased to 0.009 for the A55-5 sintered at 800 ºC and then decreased to 0.006 for the A55-10. The dielectric loss was relatively high for the A55-5 samples sintered at 850 ºC (e.g., 0.027) and 900 ºC (e.g., 0.020), which can be attributed to the composition and/or porosity of the composites. Because each component (e.g., Al_2O_3, hBN and in-situ crystallized anorthite, and glass) has a loss value between 0.0003 and 0.0024, porosity may be responsible for increasing the loss. Since K (loss)=1 (0) for air [88], it definitely reduces K, but there are various results in the literature that it increases loss for Al_2O_3 and SiO_2 and decreases loss for BN and Si_3N_4 [63]. Because the composites had dominantly Al_2O_3 and SiO_2 in the compositions, they possibly controlled the overall dielectric loss with increasing porosity. It has been reported in the literature that porosity also reduces loss in hBN/Si_3N_4 composites [90].

4.4 Thermal Properties

In LTCC applications, high thermal conductivity (k) is highly desired for a more reliable and more efficient packaging to dissipate heat generated during service. The

need for heat removal has become much more critical with the growing need to manufacture high-density and high-power devices operating at high speeds [40] [91]. Figure 4.7 shows thermal conductivity and thermal expansion coefficient of the samples sintered at optimum sintering temperatures. The A55, A55-1 and A55-2.5 were produced by dry pressing, the A55-5 and A55-10 were produced by tape casting. The k values are 36 W/m·K [37] and 0.85 W/m·K [38] at 25 °C for Al_2O_3 and glass, respectively. The average k values at room temperature increased with increasing the hBN content such that k=1.93 W/m·K for the A55, 2.15 W/m·K for the A55-1, 2.24 W/m·K for the A55-2.5, 2.46 W/m·K for the A55-5 and 2.71 W/m·K for the A55-10. The hBN crystal structure allows anisotropic physical properties parallel (//c) and perpendicular (⊥c) to the c-axis. Zhang et al. [78] investigated anisotropic thermal properties of highly textured hBN with $3Y_2O_3$-$5Al_2O_3$-4MgO added as sintering additives. The samples were hot-pressed at 1900 °C for 1 h with a sintering pressure of 30 MPa in N_2 atmosphere, and mass ratio of hBN to sintering additive was kept at 8:2. In addition, Tian et al.[79] also reported anisotropic thermal properties of highly textured hBN with CaO-Y_2O_3-Al_2O_3 added as sintering additives. The samples were hot-pressed at 1800 °C for 1 h with a sintering pressure of 0.1 MPa in N_2 atmosphere, and mass ratio of hBN to sintering additive was kept at 8:2. The k values were reported as 20-23 W/m·K for the //c and 111-137 W/m·K for the ⊥c. Note that the measurement direction was the //c in the tape-casted A55-5 and A55-10 samples. The high k value of hBN increased the k values of the composites in general but it was not as high as expected despite a relatively high thermal conductivity of hBN along the //c. This is because high amount of closed pores with increasing hBN content resulted in a limited improvement due to a very low thermal conductivity of air (0.0267 W/m·K [92]). Pores definitely puts obstacles among the hBN particles which limits heat transfer paths to enhance overall k of the composites [93]. In addition, because of the short-range order of the glass structure, the phonon thermal conductivity is delayed, and thus thermal conductivity of glasses often are very low [94]. A similar trend in the hBN/BAS systems has been reported such that k increased from 2.5 W/m·K (10 wt% hBN) to 7.2 W/m·K (50 wt% hBN) at 100 °C [95]. In fact, the A55-10 composite should have achieved a higher k since the aligned platelet hBN particles had a lower k along the c-axis or measurement direction. As seen in Figure 4.3 and Figure 4.7, dry

pressed composites have been shown to have average (or isotropic) k values due to the random orientation of the hBN particles compared to anisotropic k values resulting from the aligned particles during tape casting. For this reason, a higher k for the ⊥c (or, alternatively, a faster heat dissipation towards the edges of the LTCC modules) is expected. Similar anisotropic thermal and mechanical properties have also been reported in literature for hot-pressed Al_2O_3/hBN composites [96]. It is evident that the hBN addition significantly enhances k provided that AP is close to zero.

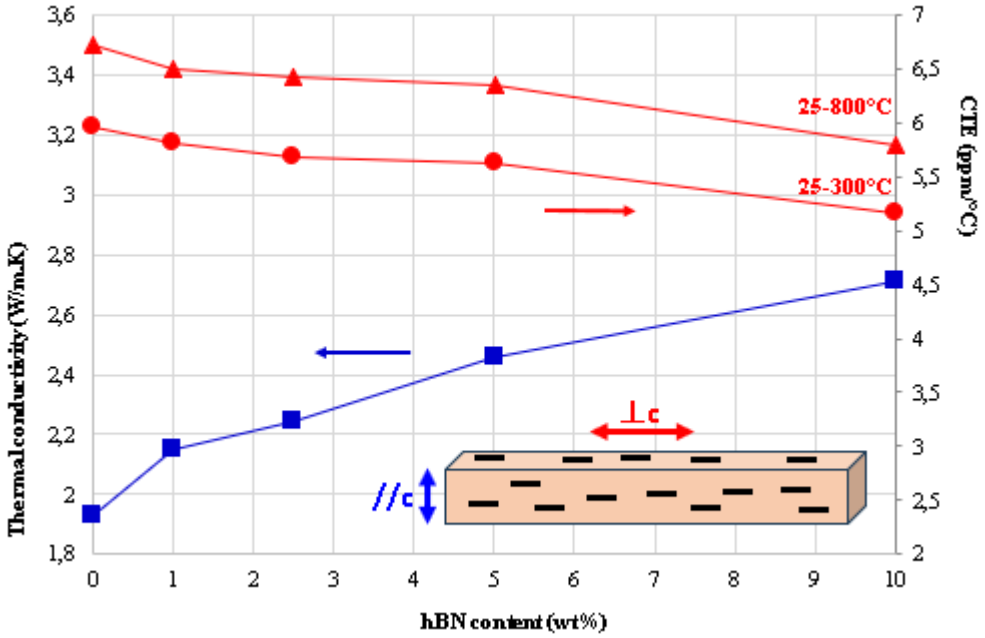

Figure 4.7 Thermal conductivity and thermal expansion coefficient of the composites sintered at optimum temperature for each composition

One of the most critical parameters in the LTCC systems is the thermal expansion mismatch of Si chips mounted on the LTCC substrates which causes failure of the melting connections between chip and substrate. Therefore, a CTE match or close to Si (~2.6–3.3 ppm /°C [97]) is very important parameter to attain. Note that the CTE measurement direction was the ⊥c in the tape-casted A55-5 and A55-10 samples. The CTE of the composites decreased with increasing hBN amount, and it was more pronounced at high hBN loadings. In other words, 6.73 ppm/°C for the A55 and 5.79 ppm/°C for the A55-10 between 25-800 °C, and 5.96 ppm/°C for the A55 and 5.17 ppm/°C for the A55-10 between 25-300 °C. The CTE value for Al_20_3 is 8.8 ppm/°C

between 0 °C and 1000 °C [28]. Silicate glasses have low CTEs due to the ability of absorbing vibrational energy by adjusting irregular bond angles [5]. In addition, hBN has a CTE of 2.3-2.4 ppm/°C for the ⊥c and 11.3-15.6 ppm/°C for the //c [78][79] which definitely helps match the final CTE of the composites to Si. In fact, hBN possesses a small negative CTE such that it is -2.72 ppm/°C for the ⊥c and 37.7 ppm/°C for the //c at room temperature [98]. Therefore, a much lower CTE value of the aligned hBN particles for the ⊥c lowered the overall CTE of the composites (i.e., particularly, for the A55-10). In addition, in-situ crystallized anorthite helped lower the CTE of the A55-10 due to its low CTE of 4.82 ppm/°C [99]. The glass transition temperatures (T_g) were determined as 648 °C for the A55 and 651 °C for the A55-1, 652 °C for the A55-2.5, 651 °C for the A55-5 and 618 °C for the A55-10. Because LTCCs have higher thermal resistance than the resins, they provide better product reliability at high temperatures. However, a number of thermal tests are applied to the LTCC circuits such as heat exposure test (i.e., 1000 hours at 150 °C), temperature cycle test (i.e., from room temperature to 125 °C) [40]. In this regard, the T_g is important for the LTCC circuits and the composites have T_g values way above the test conditions.

4.4 Mechanical Properties

LTCC substrates have become more important due to the demand for the miniaturization of electronic components. Therefore, optimization of mechanical properties is extremely important in order to prevent failure of thin layers during manufacturing or in service. Figure 4.8 shows hardness values of the Al_2O_3/glass/hBN samples sintered at optimum sintering temperatures for each composition, calculated using Equation 2.4. All samples were produced by both dry pressing and tape casting. The hardness values of Al_2O_3 and glass are 1870 HV [71] and 591 HV [71], respectively. The hardness decreased with increasing hBN amount fabricated by both dry pressing and tape casting samples. In other words, hardness values were 623±7 HV (dry pressing, AP=0.13% and CP=1.23%), 665±11 HV (tape casting, AP=0.04% and CP=1.33%) for the A55, 290±15 HV (dry pressing, AP=10.28% and CP=2.62%) and 393±12 HV (tape casting, AP=0.91% and CP=6.75%) for the A55-5, 112±13 HV (dry pressing, AP=14.87% and CP=4%), 198±10 HV (tape casting, AP=0.32% and

CP=12.49%) for the A55-10. Higher hardness values for the tape-casted composites were attributed to the higher densification levels with respect to the dry-pressed composites. Particularly, 393±12 HV for the A55-5 and 198±10 HV for A55-10 prepared by tape casting with near-zero AP were achieved due to alignment of the plate-like hBN particles enhancing both densification and hardness. However, continuous decrement in hardness with the hBN content can be attributed to high level of closed porosity, particularly for the A55-10, that weakens the whole structure. Similar decrease in hardness was obtained in hot pressed hBN/Si_3N_4 composites such that hardness considerably decreased with increasing hBN content (e.g., from 14.9 GPa (1 wt% hBN and density 3.37 g/cm^3) to 7.7 GPa (5 wt% hBN and density 3.03 g/cm^3) [100]). Based on the hardness data, mechanical properties were further characterized using the dry-pressed samples for the A55, A55-1 and A55-2.5, and tape-cast samples for the A55-5 and A55-10 because densification (or, porosity) is very critical for mechanical properties.

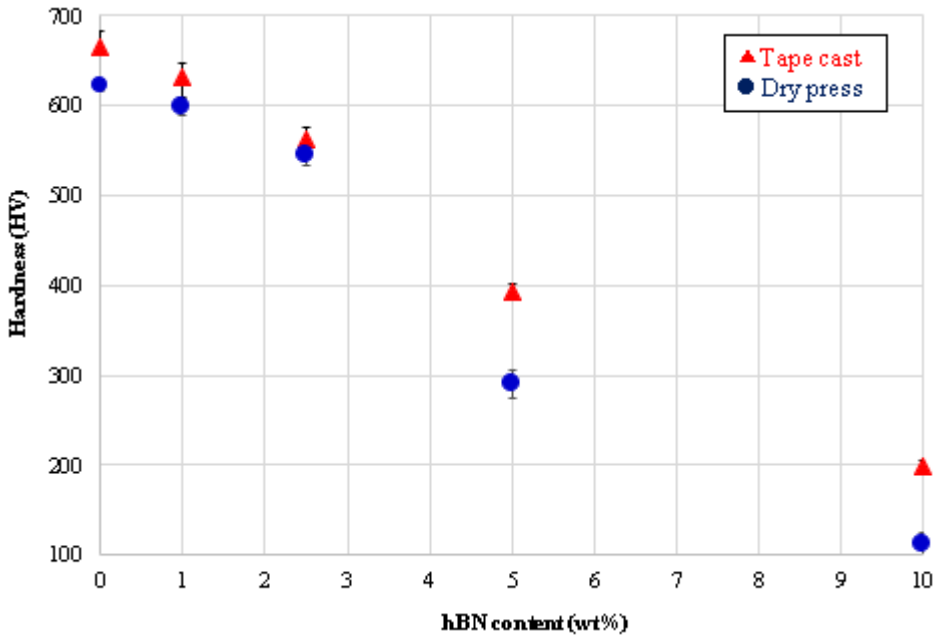

Figure 4.8 Hardness of the Al_2O_3/glass/hBN composites sintered at optimum temperature for each composition

Elastic modulus of the Al_2O_3/glass/hBN composites were calculated using Equations 2.7 and 2.8. Elastic modulus measurement was carried out using samples sintered at

optimum temperature for each composition (e.g., at 800 °C for the A55, A55-1, A55-2.5 and A55-5, and at 900 °C for the A55-10). The elastic modulus of the samples is given in Figure 4.9. The elastic modulus of Al_2O_3 and glass are 390 GPa [37], and 70 GPa [28], respectively. In general, mean elastic modulus values decreased with increasing hBN content and almost stabilized after the A55-2.5. The A55-10 sample had the lowest value. In other words, elastic modulus values were 116±4 GPa for the A55, 108±3 GPa for the A55-1, 98±8 GPa for the A55-2.5, 103±4 GPa for the A55-5 and 83±2 GPa for the A55-10. Similar effects of the platelet hBN particles on elastic modulus were reported in barium aluminasilicate ($BaAl_2Si_2O_8$, BAS)/hBN (10 to 50 wt%) composites fabricated by hot pressing at 1500 °C such that it decreased from 86 GPa at 10 wt% hBN (AP= 0.02%) without any visible micro cracks to 46 GPa at 50 wt% hBN (AP= 4%) with cracks and voids [85]. Figure 4.10 shows flexural strength of the composites sintered at optimum temperature, calculated using Equation 2.6. In general, flexural strength decreased with increasing the hBN content for the dry-pressed samples. The A55-5 reached the highest value but the flexural strength decreased at the A55-10. In other words, flexural strength values were 102±10 MPa for the A55, 76±6 MPa for the A55-1, 92±11 MPa for the A55-2.5 MPa, 110±18 MPa for the A55-5 and 82±4 MPa for the A55-10. The flexural strength of Al_2O_3 and glass are 411 MPa [37] and 87 MPa[28], respectively.

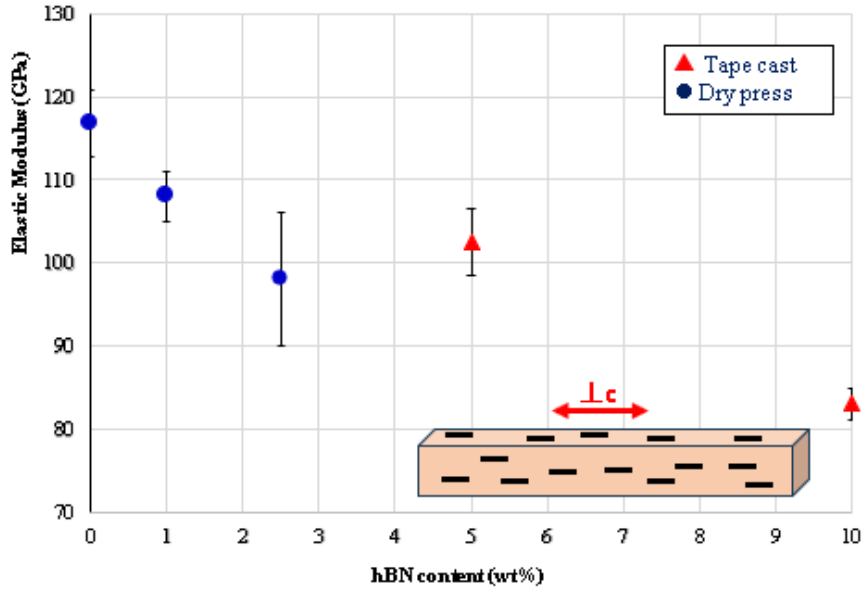

Figure 4.9 Elastic modulus of the Al_2O_3/glass/hBN composites sintered at optimum temperature for each composition.

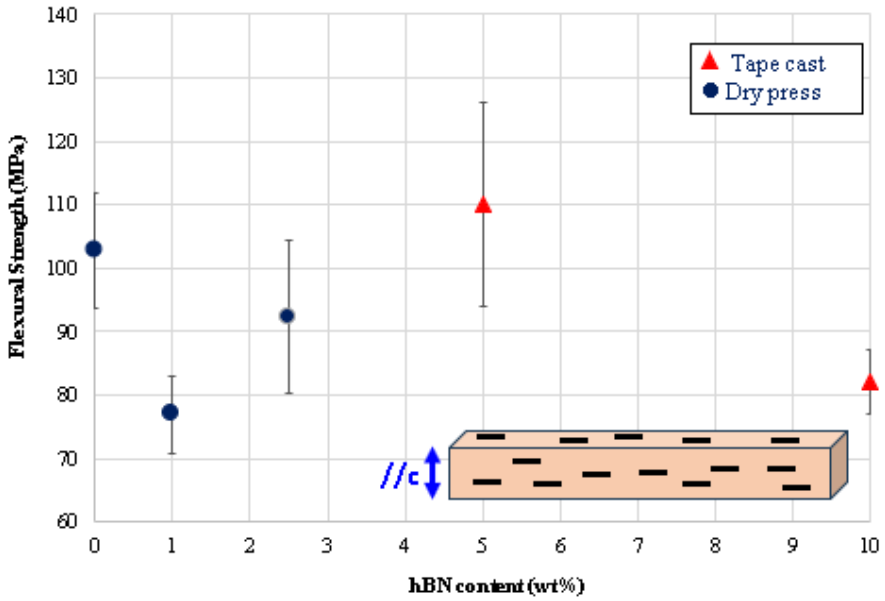

Figure 4.10 Flexural strength of the Al2O3/glass/hBN composites sintered at optimum sintering for each composition

Elastic modulus and flexural strength measurements were taken from the as-sintered samples. The samples produced by tape casting had homogeneously dispersed and oriented platelet hBN particles (i.e., anisotropic properties) as compared to the random

orientation (i.e., isotropic properties) for the samples produced by dry pressing. Although elastic modulus and flexural strength were measured from the same bar-shaped ceramics, the measurements were the ⊥c for the elastic constant and the //c for the flexural strength in the tape-casted A55-5 and A55-10 samples. Flexural strength of~ 82-138 MPa for the //c and ~18-34 MPa for the ⊥c, and elastic modulus of ~ 62-82 GPa for the //c and ~ 8-25 GPa for the ⊥c were reported for highly-textured hBN ceramics [78][79]. Therefore, elastic constant should decrease and flexural strength should increase due to anisotropic properties of the aligned hBN particles. Weak van der Waals forces are present parallel to the c-axis (//c, or, in-between the layers); however, strong sp^2 covalent bonds are present perpendicular to the c-axis (⊥c, or, in the layers). Therefore, crack path in the fracture morphologies is much flatter for the ⊥c while it is curved crack propagation paths with many crack deflections for the //c [78] [79]. In addition to the anisotropic properties of the hBN structure, densification (and closed porosity) levels are also critical for mechanical properties because the presence of defects such as pores in the structure leads to lower mechanical properties [101]. Figure 4.9 indicates that elastic constant decreases in general, but slightly increases in the A55-5 due to the hBN alignment with respect to the isotropic dry-pressed samples. A relatively sharp decrease in the A55-10 is consistent with the hBN anisotropic properties. Figure 4.10 indicates in general that flexural strength increases with the hBN content up to the A55-5 that is consistent with the hBN anisotropic properties but then decreases at the A55-10. Different densification levels in the tape-casted A55-5 and A55-10 composites compete with the anisotropic properties. The A55-5 has RD=92.33%, AP=0.91%, CP=6.75% and the A55-10 has RD=87.19%, AP=0.32%, CP=12.49%. Therefore, a high level of CP in the latter considerably decreased the flexural strength. It is important to note that as-sintered ceramics were used for the measurements, which could also give rise to property variations in case of the presence of microcracks on the surfaces. The overall properties of the Al_2O_3/glass/hBN composites sintered at optimum sintering temperature for each composition are summarized in Table 4.1.

Table 4.1 Summary of the physical properties of the composites sintered at their optimum temperatures for each composition

			Dielectric Properties		Thermal Properties		Mechanical Properties		
Composition	Sintering temperature (°C)	Density (g/cm^3)	Dielectric constant	Dielectric loss	Thermal conductivity (W/m.K) (at 25°C)	CTE (ppm/°C) (25-300°C)	Hardness (HV)	Elastic Module (GPa)	Flexural Strength (MPa)
AS5	800	2.89	7.3	0.0036	1.93	5.96	623±7	116±4	102±10
AS5-1	825	2.81	7.2	0.0039	2.15	5.81	599±9	108±3	76±6
AS5-2.5	825	2.75	6.6	0.0023	2.24	5.68	543±10	98±8	92±10
AS5-5	825	2.65	6.55	0.009	2.46	5.62	393±12	102±4	110±18
AS5-10	900	2.45	5.57	0.006	2.71	5.17	198±10	83±2	82±4

Al_2O_3/glass/hBN composites were successfully fabricated for the LTCC applications. XRD results proved that hBN neither chemically reacted with the other phases nor decomposed with temperature, which is critical to increase thermal conductivity and to decrease dielectric constant at the same time. Although AP was less than 1% in all composites, CP increased with increasing hBN content such that CP=1.23% (with RD=98.64% and AP=0.13%) for the A55 and CP=12.49% (with RD=87.19% and AP=0.32%) for the A55-10. Porosity affected physical properties. For example, dielectric constant decreased (or, alternatively, enhanced) such that it was 7.3 for the 0 wt% hBN and 5.57 for the 10 wt% hBN composites at 5 MHz. Increased hBN content from 0% to 10 wt% decreased hardness from HV 623±7 to 198±10, flexural strength from 102±10 to 82±4 MPa, and elastic modulus from 116±4 to 83±2 GPa. However, mean thermal conductivity was strongly improved from 1.93 W/m·K for the 0 wt% hBN to 2.71 W/m·K for the 10 wt% hBN at 25 °C but it was lower than expected due to the high level of CP. Elastic constant should decrease and flexural strength should increase due to anisotropic properties of the aligned hBN particles but different densification levels in the tape-casted A55-5 and A55-10 composites competed with the anisotropic properties. An increase in polymer ratio in the binder solution from 17 wt% (5 wt% hBN) to 25 wt% (10 wt% hBN) was required due to high surface area of the hBN particles in order to make a successful tape casting. Therefore, hBN content greater than 10 wt% was not applied due to both difficulty in tape casting and densification temperature exceeding 950 °C that could cause hBN oxidation (see Figure 3.7).

CHAPTER 5

MECHANICAL, THERMAL AND DIELECTRIC PROPERTIES OF MULLITE/GLASS COMPOSITES

In Chapter 4, Al_2O_3/glass/hBN composite properties were investigated and hBN addition significantly improved the properties with respect to the base Al_2O_3/glass composite. Particularly, thermal conductivity was enhanced with increasing hBN content. In this section, therefore, it was further aimed to improve the properties by replacing Al_2O_3 with mullite ($3Al_2O_3.2SiO_2$). Mullite has suitable physical properties for structural and electronic applications due to high melting temperature (1830 °C), low density (3.2 g/cm^3), low thermal conductivity (6.07 W/m·K at 20 °C and 3 W/m·K at 1400 °C), low dielectric constant (6.5-8.1 at 1-40 GHz), low thermal expansion (~ 4.5 ppm/°C between 20 °C and 1000 °C), excellent creep and high-temperature resistance (~ 400 MPa flexural strength up to 1300 °C) [77]. At the same time, thermal shock resistance of mullite (142.4 ºC [102]) is higher than that of Al_20_3 (101ºC [5]). Mullite/glass (10-60 wt%) composites were prepared by dry pressing to determine densification temperature range and to investigate mechanical, dielectric and thermal properties optimized for the LTTC and radome applications. The mullite glass composites will hereafter be referred to as M10, M20, M30, M50, M55, M60 which corresponds to 10, 20, 30, 50, 55, and 60 wt% glass, respectively. For comparison of the physical properties, liquid phase sintered dense mullite (see Table 3.3 for mullite composition) properties were used (e.g., 3.4 wt% TiO_2 as additive, bulk (relative) density=3.06 g/cm^3 (97%) and AP=0.62% [102]**)**.

5.1 Densification

Figure 5.1 shows densification and apparent porosity (AP) of the composites as a function of glass content and temperature. The solid lines are drawn to guide eye. The densification behaviors differed from each other as full densification was achieved at lower temperatures with increasing glass amount. The optimum densification temperatures and bulk densities for each composite were determined by considering

high bulk density, near-zero AP and water absorption (WA), as calculated from the Archimedes' principle. The optimum densification temperatures of composites derived from Figure 5.1 is compared in Figure 5.2. The optimum densification conditions were reached at 1550 °C for the M10 (2.99 g/cm^3, AP=0.06% WA=0.02%), 1450 °C for the M20 (2.86 g/cm^3, AP=0% WA=0%), 1400 °C for the M30 (2.76 g/cm^3, AP=0.16% WA=0.05%), 850 °C for the M50 (2.64 g/cm^3, AP=0.5% WA=0.21%), 825 °C for the M55 (2.63 g/cm^3, AP=0.19% WA=0.17%) and 825 °C for the M60 (2.6 g/cm^3, AP=0.2% WA=0.07%). Closed porosity was less than 1.40%. As the glass amount was increased, bulk densities decreased due to lower density of the glass (i.e., the theoretical density of mullite=3.13 g/cm^3 [102] and glass=2.43 g/cm^3 [71]). The glass contents by volume percent in the M10, M20, M30, M50, M55, and M60 were 12.5, 24.3, 35.5, 56.2, 61.15 and 65.8, respectively. The densification plots indicated two distinct regions, that is, densification temperatures less than 850 °C for the M50-M60 and more than 1400 °C for the M10-M30 composites. A higher glass content in the former induced densification at or near softening point of the glass (e.g., 852 °C, see also Figure 3.2) and a low amount of glass in the latter induced densification above melting point of the glass (e.g., 1104 °C, see also Figure 3.2).

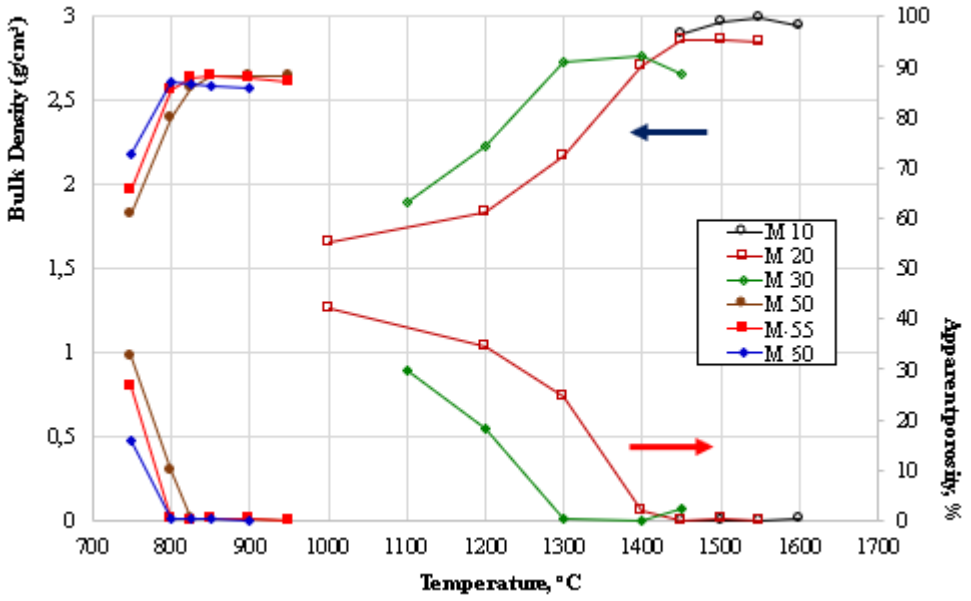

Figure 5.1 Densification of the composites as a function of glass content and temperature

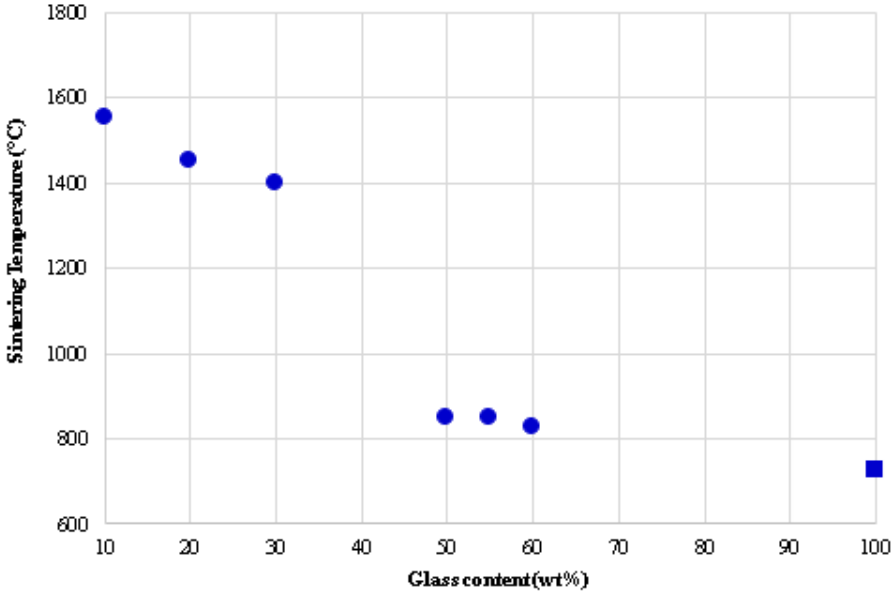

Figure 5.2 Optimum sintering temperatures of the mullite/glass composites.

5.2 Phase formation and microstructure evolution

The SEM image of the composites sintered at their optimum temperatures are shown in Figure 5.3. Darker regions were mullite and lighter regions were glass phase. Small spherical particles on the surfaces were silica left from polishing with colloidal silica. Note that mullite ($3Al_2O_3.2SiO_2$) and glass (65.8 wt% SiO_2, 15.1 wt% Al_2O_3) had common cations, which decreased atomic number dependent contrast. Similar to the densification behaviors, glass content altered microstructure development. In the M10-M30 composites, the mullite grains were much bigger than those in the M50-M60 composites. In addition, although the glass phase homogeneously embraced the mullite grains in all cases, the M10-M30 composites had more contacts between the mullite grains. The M10 sample had the largest and most anisotropic grains as well as most grains in contact with each other (Figures 5.3 (a-b)). The least amount of glass induced a liquid phase sintering and promoted anisotropic or faceted grain growth by means of solution of smaller grains and then precipitation on larger grains. In fact, the same situation was valid for the M20 and M30 samples, except for more liquid phase present with increasing glass content accordingly, which resulted in still bigger but more corner-rounded mullite grains due to increased diffusion distance among the mullite grains (Figures 5.3 (c-d) and 5.3 (e-f)). Similar microstructure results were

reported in literature [103][104]. Glass-rich regions became more prominent with the glass content in the M50-M60 composites. In other words, the mullite grains (in fact, irregularly shaped particles due to ball milling) were totally distributed in the microstructure without any grain growth (Figures 5.3 (g-k)), which indicated viscous sintering due to the presence of a high liquid volume. Densification was completed by rearrangement of the liquid phase alone in the viscous sintering mechanism without significant grain shape/size change during sintering [105]. Densification and microstructure evolution results indicate that the amount of the glass phase is critical because it dramatically changes densification temperature by means of liquid phase and viscous sintering mechanisms, and the morphology and size of the mullite grains by changing grain-to-grain distance. Similar results were also reported for the Al_2O_3/(20-60 wt%) glass composites [71] and textured Al_2O_3 sintered in the presence of CaO and SiO_2 (1:1 ratio) added as a liquid phase former[106].

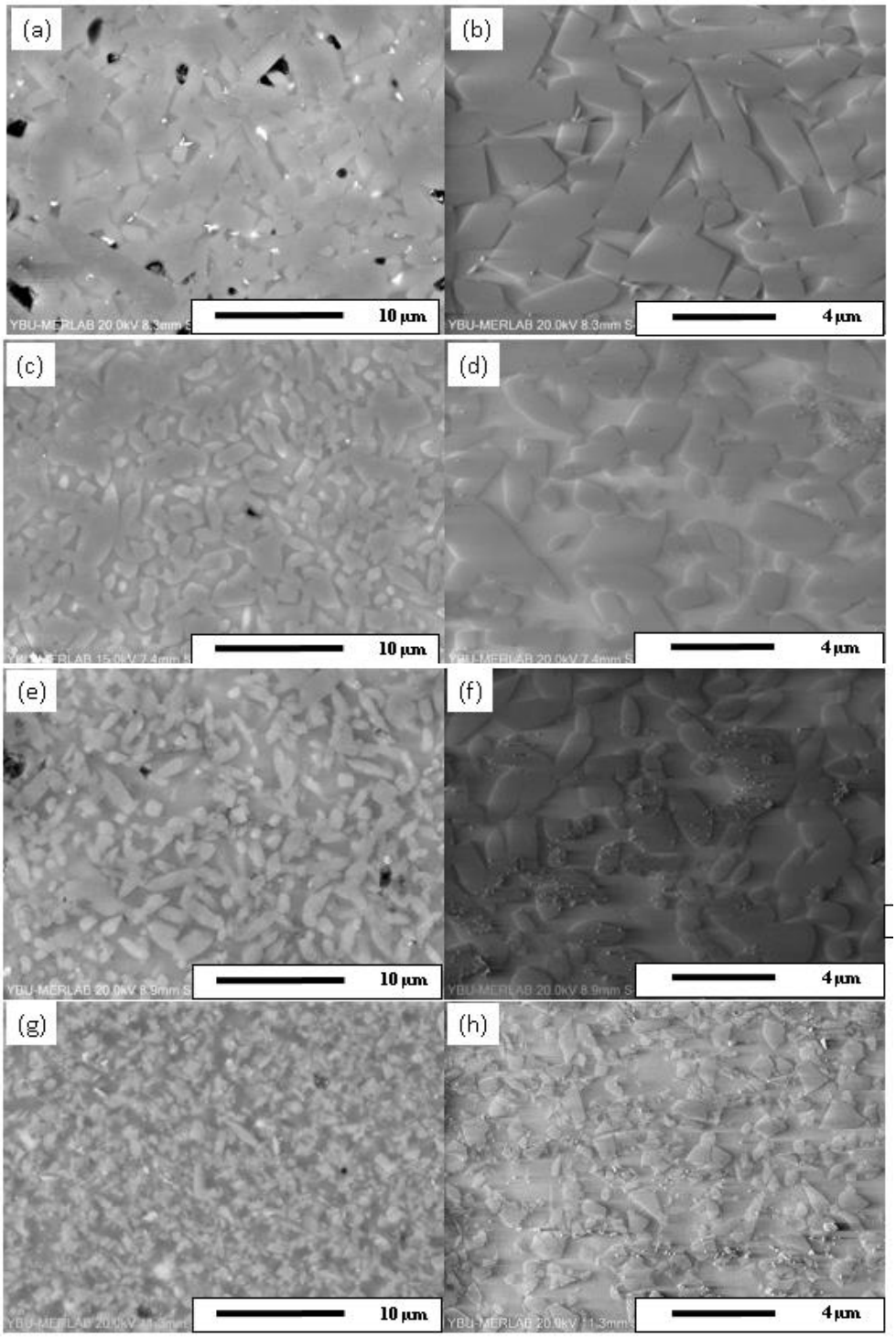

Figure 5.3 SEM pictures of the samples sintered at 1550 °C; (a) and (b) M10, 1450 °C; (c) and (d) M20, 1400 °C; (e) and (f) M30, 850 °C; (g) and (h) M50, 825 °C; (i) and (j) M55, 1450 °C; (k) and (l) M60

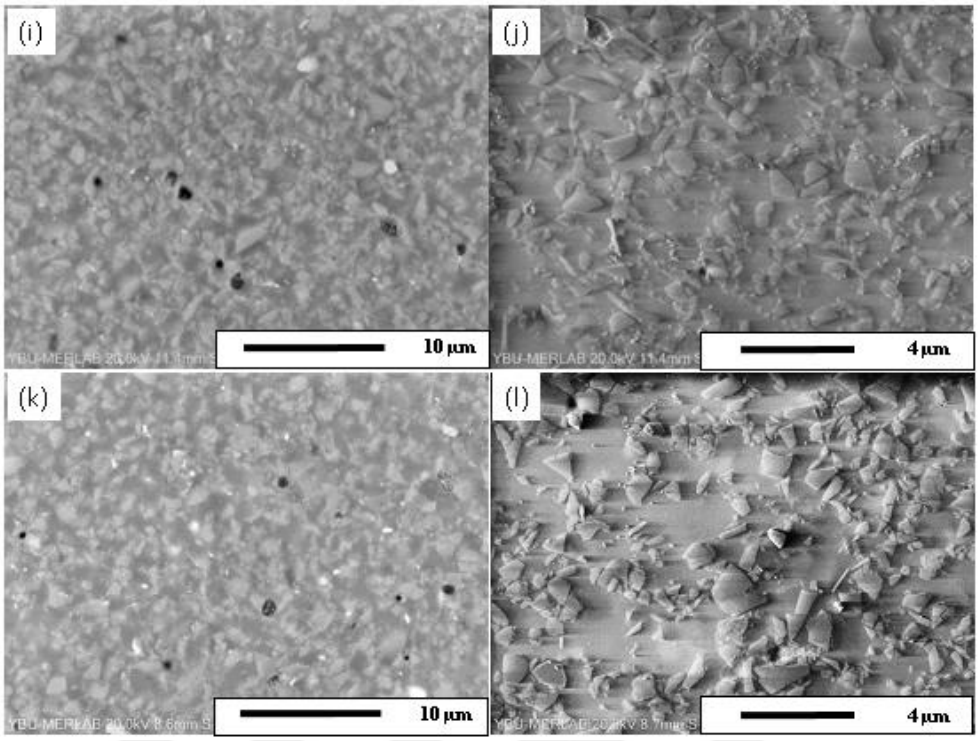

Figure 5.3 (continued) SEM pictures of the samples sintered at 1550 °C; (a) and (b) M10, 1450 °C; (c) and (d) M20, 1400 °C; (e) and (f) M30, 850 °C; (g) and (h) M50, 825 °C; (i) and (j) M55, 1450 °C; (k) and (l) M60

The diffusion distance between the mullite grains varies with the liquid content and is equivalent to the grain boundary layer thickness (also known as the grain-to-grain distance), which is proportional to;

$$2/3 \cdot (V_{Liq}/V_{Sol}) \qquad 5.1$$

where V_{Liq} is the liquid content and V_{Sol} is the solid content in the composites [107]. Compositional analysis was carried out by EDS. Note that it is a qualitative method and does not give exact ratios. For the M20 composite, the Al/Si ratio calculated from the glass region was 1.67 (grain to grain distance: 0.21), that is much higher than the original ratio of 0.27 calculated from the glass itself. The higher ratio can be attributed to more Al dissolution with respect to Si from the mullite phase because the Al/Ca and Si/Ca ratios were 22.77 and 13.66 as opposed to the original glass ratios of 1.08 and

4.01, respectively. Note that an EDS analysis from the mullite grains yielded an Al/Si ratio of 3.29 which is very close to the stoichiometric ratio of 3.14. These results are consistent with the microstructure development observed in the M20 (in fact, in the liquid phase sintered M10-M30 composites, see Figures 2 a-f). As for the M55 composite, the Al/Si ratio was 1.05 (grain to grain distance: 1.04) that is lower as compared to the M20 due to low temperature viscous sintering. Dursun et al. [103] also showed in the glass/Al_2O_3 composite that as the glass ratio increased, the Al/Si ratio decreased (i.e., 2.45 for 20 wt% glass to 0.98 for 55 wt% glass), suggesting that Al_2O_3 significantly dissolved in the glass phase.

Figure 5.4 shows that the weight loss of the M20 green sample containing 2 wt% polymer was measured by thermogravimetric analysis in order to understand the evaporation of the alkaline cations. The polymer in the green sample was removed up to 600 °C and weight loss was 4.13 wt% (e.g., polymer and moisture). After 600 °C, a slope change was observed. The total weight loss was 5.59 wt% up to 1450 °C, which yielded 1.46 wt% loss from the composition. A thermogravimetric analysis of the same glass composition revealed that weight loss was accelerated after 1180 °C such that 47 wt% of the initial Na_2O (1.27 wt% loss from the composition) and 94 wt% of the initial K_2O (2.58 wt% loss from the composition) were evaporated during heating [103]. It has been reported the volatilization of K_2O and Na_2O between 967°C and 1397°C from silica melts containing SiO_2, CaO, Na_2O and K_2O as well [104]. In fact, Figure 5.1 shows that de-densification happened after optimum sintering temperatures for the M10-M30 compositions and AP increased due to evaporation of Na_2O and K_2O from the glass phase, resulting in appearance of some visible pores within the glass matrix.

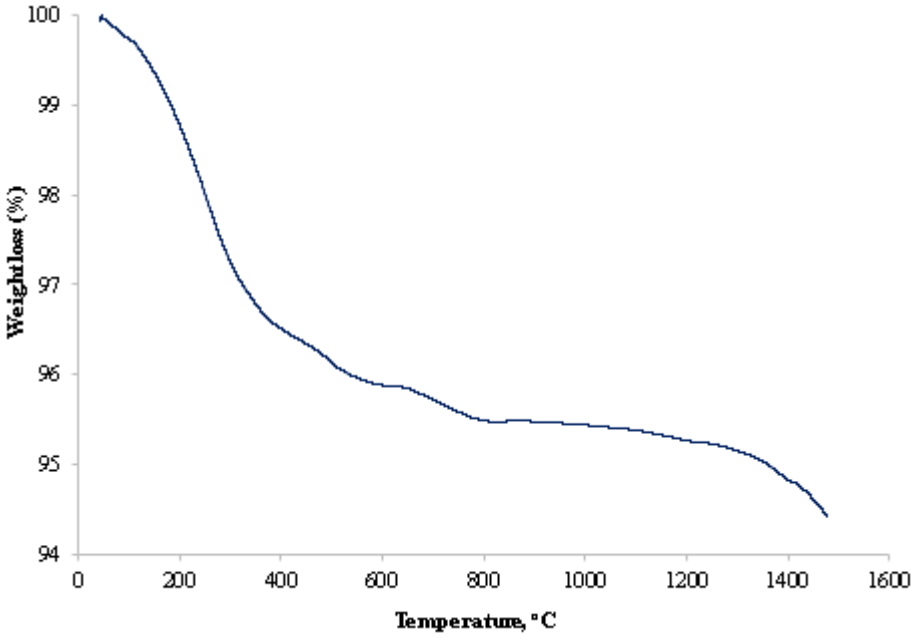

Figure 5.4 Thermogravimetric result of the M-20 with 2 wt% polymer.

Figure 5.5 shows XRD patterns of the glass and composites sintered at their optimum temperatures. Figures 5.5 and 5.6 are given for a more detailed understanding of the phase formations depending on the glass amount and temperature for the M20 and M55, respectively. The glass was amorphous even after heating at 825 °C except for a small quartz peak at 2θ=26.77° (Card number: 00-009-0466), as given in Figure 3.4. The XRD pattern of each composition was normalized according to the highest intensity mullite peak at 2θ = 26.16° (Card number: 00-015-0776). The peaks other than mullite were in good agreement with the anorthite phase $(Ca,Na)(Si,Al)_4O_8$ (Card number: 00-041-1481). Figure 5.5 also illustrates an amorphous background between nearly 2θ = 20–30° for the M50, M55 and M60 composites. Furthermore, the main anorthite peak intensity at 2θ = 28.08° first decreased from the M50 to M55 and then increased from the M55 to M60. In other words, higher temperature caused more anorthite crystallization. Figure 5.6 shows that the anorthite phase first appeared at 825 °C at a very low intensity in the M55 but then started increasing significantly with the temperature and became the strongest peak. It was reported that anorthite crystallization was dependent on both glass content and temperature in the Al_2O_3/glass composites such that high temperature together with high glass content induced the

most in-situ anorthite crystallization [71], as evidenced in this study. Anorthite phase was not observed for the M10, M20 and M30 sintered at the optimum temperatures (Figure 5.5). Furthermore, phase evolution as a function of temperature for the M20 (Figure 5.7) indicates that anorthite forms at low temperatures but it then disappears after 1300 °C within the XRD detection limits. These results suggest that absence of anorthite phase in the M10-M30 composites may be attributed to mullite grain growth/coarsening dominating the microstructure due to sintering way above the melting temperature of the glass (1104 °C) or evaporation of alkaline materials at very high temperatures. In fact, very broad mullite peaks observed for the M10 (Figure 5.5) and M20 (Figure 5.7) compositions could be attributed to the various Al/Si ratios within the mullite solid solution range (from 71.8 to 74.3 wt% of Al_2O_3 under stable conditions [108]). It is particularly evident that sharper mullite peaks at low temperatures become broader with increasing temperature for the M20 composition. The anorthite peak was not observed due to Al_2O_3 grain coarsening in the Al_2O_3/20 wt% glass composites sintered at 1350 °C in the CAS/Al_2O_3 system [103].

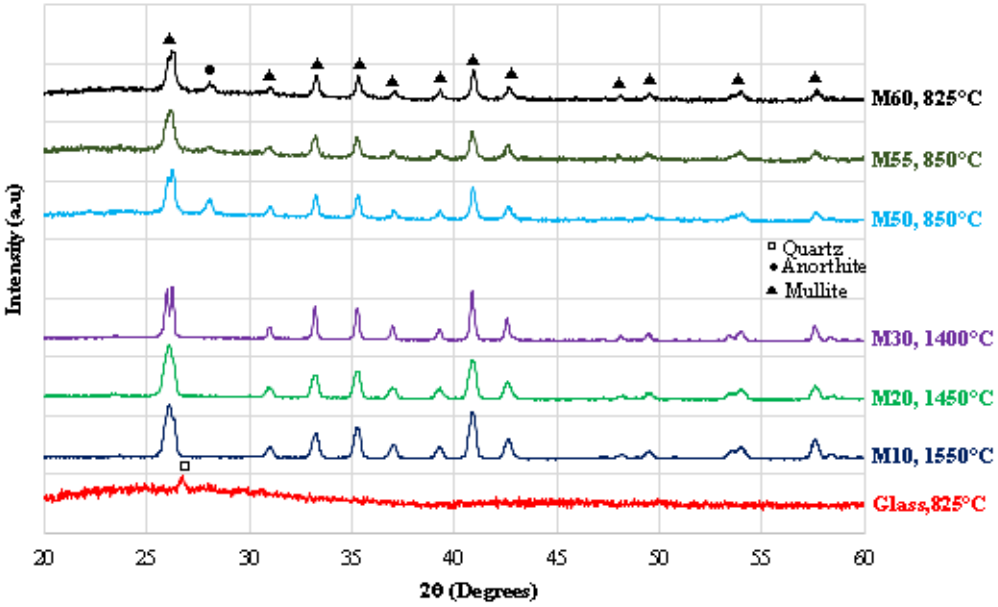

Figure 5.5 XRD patterns of the composites sintered at their optimum temperatures for each composition

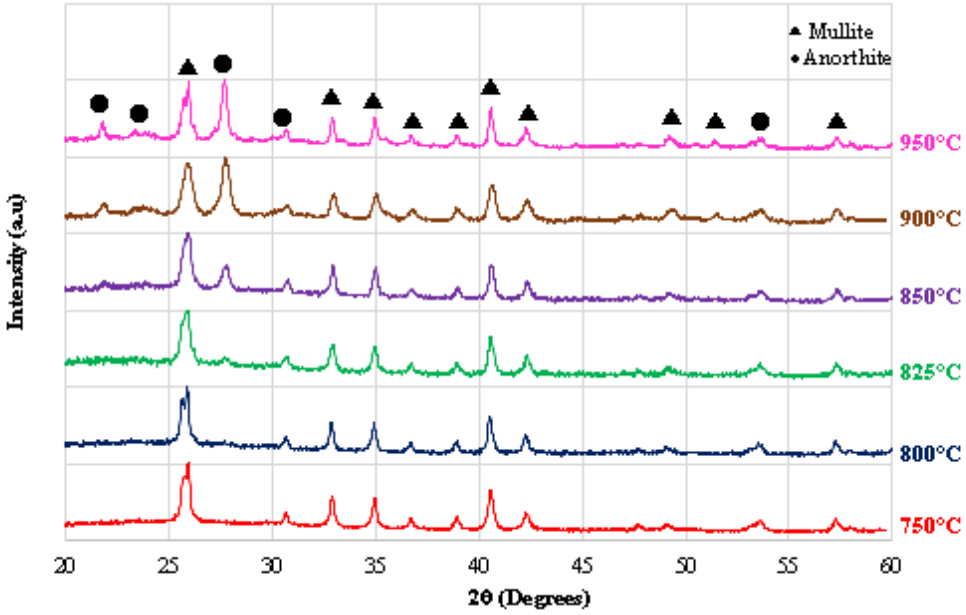

Figure 5.6 XRD patterns of the M55 sintered at different temperatures.

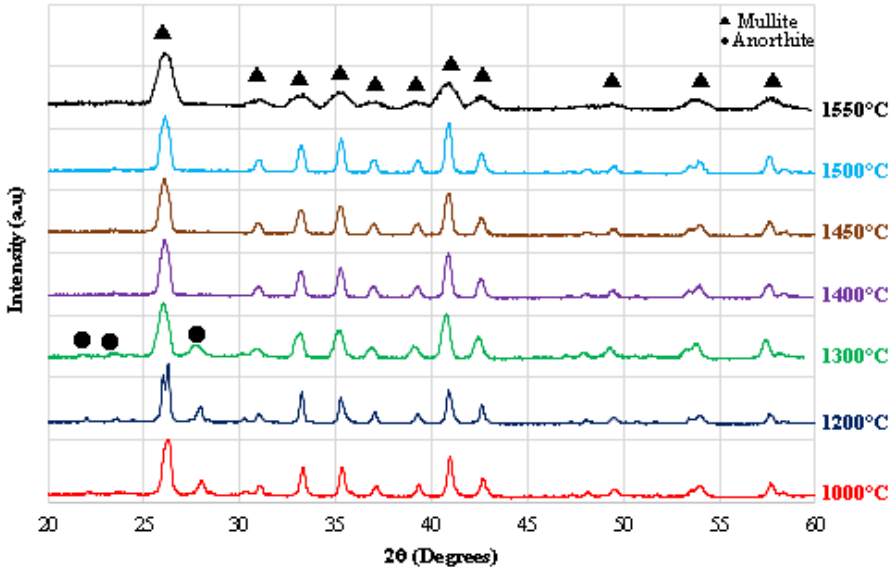

Figure 5.7 XRD patterns of the M20 sintered at different temperatures.

5.3 Dielectric Properties

The dielectric properties depend on several factors, including densification (or porosity), glass content, and crystalline phases present in the structure. The dielectric constant and loss values of the composites sintered at optimum sintering temperature

for each composite are given in Figure 5.8. Capacitance of the composites were measured at 5 MHz and then the dielectric constant (K) was calculated, using Equation 2.11. The dielectric constant (loss) values were 7.4 (0.0031) for mullite [102], 7.29 (0.0028) for the M10, 7.12 (0.0025) for the M20, 6.98 (0.0013) for the M30, 6.79 (0.0043) for the M50, 6.68 (0.0037) for the M55, 6.71 (0.0021) for the M60 and 6.37 (0.0016) for glass [71]. In other words, the glass phase significantly decreased the K due to its lower K = 6.37 [71] at 5 MHz. A similar effect on dielectric properties was reported for the CAS/Al_2O_3 (20 wt% to 60 wt%) composites and dielectric constant decreased with increasing glass content from 8.76 (20 wt% glass) to 7.32 (60 wt % glass [71]). It was also reported for the SiO_2-B_2O_3-CaO-MgO glass/Al_2O_3 composites sintered at 875 °C that dielectric constant at 1 MHz decreased with increasing glass content from 7.57 (50 wt% glass) to 7.32 (60 wt% glass) [109]. Figure 5.5 indicated that anorthite crystallization was dependent on both temperature and glass content such that the anorthite peak intensity was the highest for the M50 and lowest for the M55. Accordingly, the M50 had the highest K and the M55 had the lowest K although they had similar densification levels, which can be attributed to more anorthite crystallization because the K for amorphous and single crystal anorthite are 7.5 and 7.14 at 1 MHz, respectively [87].

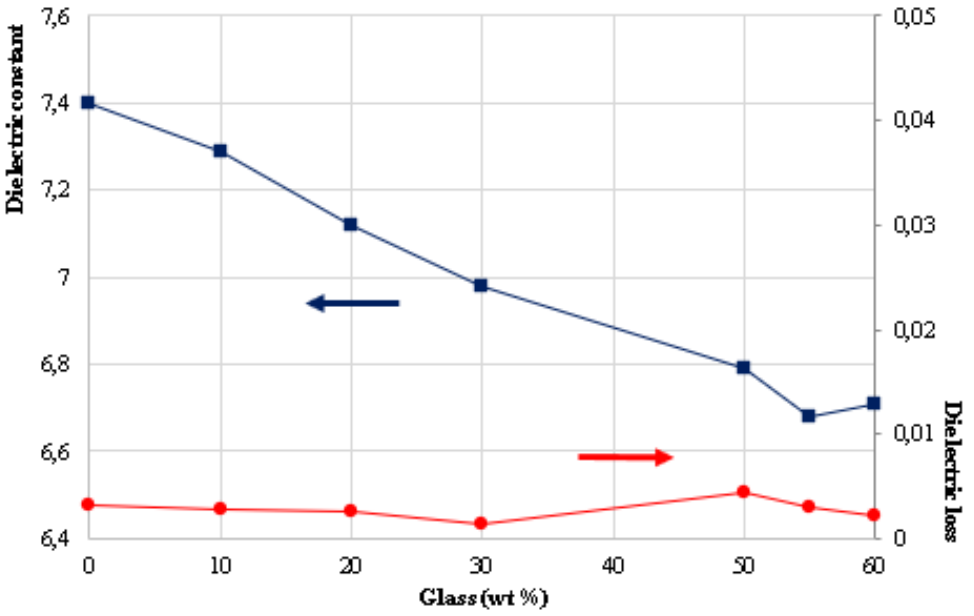

Figure 5.8 Dielectric properties of the composites sintered at optimum sintering temperature for each composition

In general, dielectric losses vary in frequency and temperature, and are caused by dopant and impurity atoms, microstructural defects (e.g., grain boundaries, porosity, microcracks, dislocations, vacancies), order-disorder, crystal structure and orientation [110]. It should be as small as possible to ensure maximum signal separation [111]. The dielectric loss behavior varied for the liquid-phase sintered M10-M30 and viscous-sintered M50-M60 composites. For example, loss decreased with increasing glass content for each group such that from 0.0031 for mullite to 0.0013 for the M30, and from 0.0043 for the M50 to 0.0016 for glass, which might be attributed to the alteration of glass composition due to solution-precipitation for the former, and almost no change in the glass composition for the latter. Grain boundaries can form poles in dielectric materials, and hence grain growth is a factor that can increase the loss factor [110] for the M10-M30 composites. On the other hand, anorthite formation (i.e., 0.0011 and 0.0024 at 1 MHz for single crystal and amorphous anorthite [87], respectively) for the M50-M60 composites were also responsible for the overall loss behavior. Note that dielectric loss is a direct measurement that could easily vary even a different impedance analyzer is used.

5.4 Thermal Properties

In LTCC applications, high thermal conductivity (k) is highly desired for a more reliable and more efficient packaging to dissipate heat generated during service. The need for heat removal has become much more critical with the growing need to manufacture high-density and high-power devices operating at high speeds [40] [91]. One of the most critical parameters in the LTCC systems is the thermal expansion mismatch of Si chips mounted on the LTCC substrates which yields failure of melting connections between chip and substrate. Therefore, a CTE match or close to Si (~2.6–3.3 ppm /°C) is very important parameter to reach [97]. Figure 5.9 compares thermal conductivity (k) and thermal expansion coefficient (CTE) of the composites sintered at optimum temperature for each composition. The CTE values were calculated for 25-300 °C and 25-800 °C ranges. In general, the k of the composites measured at 25 °C decreased with increasing glass amount such that it sharply decreased from 4.45 W/m·K for the M10 to 2.2 W/m·K for the M30, and then gradually to 1.55 W/m·K for the M60. Note that the end compositions mullite and glass has k=6.07 W/m·K [77] and k=0.85 W/m·K [38] at 25 °C, respectively. The M10 and M20 had a higher k due to both less glass content and larger mullite grains mostly in contact (see Figures 5.3 (a-d)). Then, a decline was further observed from the M30 to the M60 due to higher glass content embracing and separating smaller mullite grains, thereby preventing heat-conducting pathways between the mullite grains (see Figures 5.3 (g-l)). In literature, decrease in phonon scattering in ceramics is due to the larger grain size resulting in less grain boundary area [112], which increases the k. A similar effect was reported for the CAS/Al_2O_3 (20 wt% to 60 wt%) composites and the k decreased with increasing glass content from 1.25 W/m·K to 0.98 W/m·K [71]. It was also reported for the SiO_2-B_2O_3-CaO-MgO glass/Al_2O_3 composites that k decreased with increasing glass content from 3.56 W/m·K (50 wt% glass) to 3.20 W/m·K (60 wt% glass)[109]. Although crystalline phases such as mullite and in-situ crystallized anorthite were present in the structure, these phases were embraced by an amorphous phase that reduced the overall k of the composites [109].

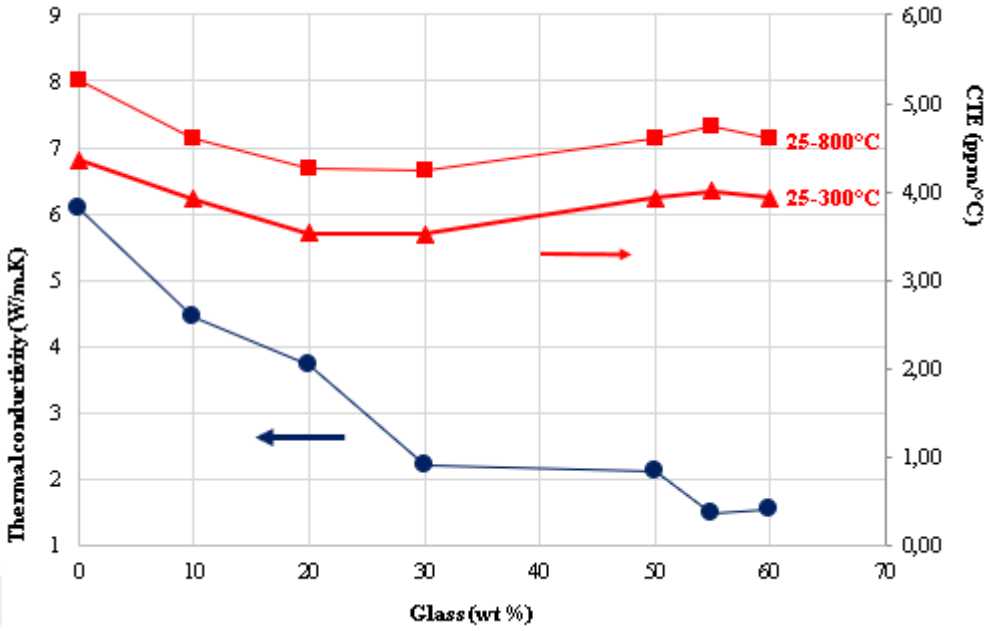

Figure 5.9: Thermal conductivity and thermal expansion coefficient of the composites sintered at optimum temperature for each composition.

An increasing glass content decreased the CTE to 4.61 ppm/°C for the M10, 4.27 ppm/°C for the M20 and 4.25 ppm/°C for the M30. The CTE for mullite is 5.3 ppm/°C between 25 °C and 1000 °C [113], which is close to the measured CTE of 5.26 ppm/°C [102]. The silicate glasses have low CTE's (i.e., 0.55 ppm/°C [28] between 0 and 1000 °C for vitreous silica) due to its ability to absorb vibration energy by adjusting irregular bond angles [5], which explains that high SiO_2 content in the glass caused lowering the CTE's of the M10-M30 composites. The CTE values remained almost constant but little higher with further increasing the glass content such as 4.60 ppm/°C for the M50, 4.75 for the M55 and 4.61 ppm/°C for the M60 between 25 °C and 800 °C, which can be attributed to the in-situ crystallized anorthite due to its relatively higher CTE of 4.82 ppm/°C [99]. Because the circuit temperatures were not that high for the LTCC applications, the CTEs were also calculated for the 25-300 °C range and they varied little, that is, from 3.93 to 4.01 ppm/°C, which are close to the CTE of Si. The glass transition temperatures (T_g) were determined as 642 °C for the M50, 650 °C for the M55 and 647 °C for the M60, 722 °C for the M10, 709 °C for the M20 and 700 °C for the M30. For radome materials, a high T_g determines the operating temperature such

that the higher the T_g the higher the reliable operating temperature. Because LTCCs have higher thermal resistance than the resins, they provide better product reliability at high temperatures. However, a number of thermal tests are applied to the LTCC circuits such as heat exposure test (i.e., 1000 hours at 150 °C), temperature cycle test (i.e., from room temperature to 125 °C) [40]. In this regard, the Tg is important for the LTCC circuits and the composites have Tg values way above the test conditions.

5.5 Mechanical Properties

The mechanical properties of the sintered samples depend on the crystal phases, densification (or apparent porosity) and the presence of defects [101]. Figure 5.10 shows flexural strength and elastic modulus of the composites sintered at optimum temperature for each composition. The composites were prepared at dimensions of 3x4x50 mm^3 to determine both flexural strength and elastic modulus using as-sintered samples. The flexural strength values of mullite and glass are 182 MPa [102] and 87 MPa [28], respectively. The flexural strength of the composites first slightly decreased from 182 MPa [102] (mullite) to 180±49 MPa (M10) and then sharply decreased to 112±10 MPa (M30), and then remained almost the same (e.g., 95±21 MPa for the M50 to 89±20 MPa for the M60) due to viscous sintering. A similar effect on flexural strength was also reported for the CAS/Al_2O_3 (20 wt% to 60 wt%) composites and it decreased from 387 MPa (for 20 wt% glass) to 213 MPa (for 60 wt% glass) [71]. The M10 sample had a higher flexural strength due to its high mullite content together with a supportive microstructure by means of high aspect ratio grains (see Figures 5.3 (a-b)). A lower flexural strength of the glass phase decreased the strength of the composites towards the M30. The elastic modulus of mullite and glass are 185 GPa [102] and 70 GPa [28]. In general, similar to the flexural strength behavior, mean elastic modulus values sharply decreased with increasing glass content for the M10-M30 composites (e.g., 189±8 GPa-131±4 GPa) and then remained almost the same for the M50-M60 composites (e.g., 107±4 GPa-98±4 GPa). The mullite grains were surrounded by the glass phase and hence the glass phase with low elastic modulus dominated the microstructure with increasing the glass content. A similar effect has been reported for the CAS/Al_2O_3 composites and the elastic modulus decreased with increasing glass content such as 231 GPa for the 20 wt% glass and 105 GPa for the 60

wt% glass [71]. It is also important to note that the M10 composite had very close flexural strength and elastic modulus values to the mullite.

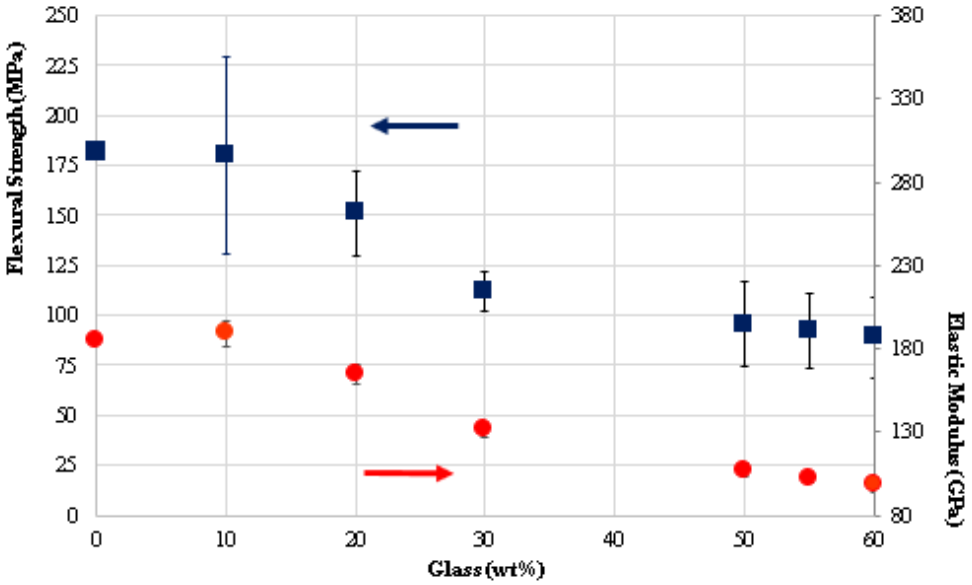

Figure 5.10. Elastic modulus and flexural strength of the composites sintered at optimum sintering temperature for each composition.

Macroscopic views of the fractured bars are shown Figure 5.11. Even though the glass matrix homogeneously covered the mullite grains, the fracture type changed significantly with increasing glass content. For example, the liquid-phase sintered M10-M30 group had nearly straight single fractures, while the viscous sintered M50-M60 group had crooked single fractures, but without any multiple fragmentations for all cases. If the fractures are of low energy-level, it usually results in chipless single fractures. According to the ASTM standard C1161-18, ceramics can break into more fragments in high energy-level fractures (i.e., multiple fractures with/out chip off and/or crack branches). Similar results were reported for the CAS/Al_2O_3 system such that 50 wt% glass composite had a crooked single fracture with a flexural strength of 147 MPa as compared to 213 MPa for the 60 wt% glass composite with multiple fractures with chip off [103].

Figure 5.11 Fractured composites

The hardness of the mullite/glass composites were calculated using Equation 2.4 and is compared in Figure 5.12. Figure 5.12 (a) shows the hardness of the mullite/glass composites with increasing sintering temperature. The grid lines are drawn to guide eye. Increasing temperature enhanced densification and decreased porosity in the mullite/glass composites, which resulted in higher hardness values. Figure 5.12 (b) compares the hardness values for each composition sintered at optimum temperature. The hardness values decreased with increasing glass amount (e.g., sharply from HV 1140±33 for the M10 to HV 800±30 for the M30 and gradually to HV 642±10 for the M60) due to the low hardness of the glass phase embracing mullite grains and thereby separating them as shown in Figures 5.3 (g-l). The reported hardness values of mullite ranged from HV 1070 to 1120 [102] and was HV 591±33 [71] for the glass. The M10 had the highest hardness among the composites due to the highest mullite content (or lowest glass content of 12.5 vol%). In addition, the hardness of the M10 sample was slightly higher than the reported mullite value [102], which can be attributed to the different liquid phase formers and densification levels (i.e., relative density of 97% [102] versus 99%).

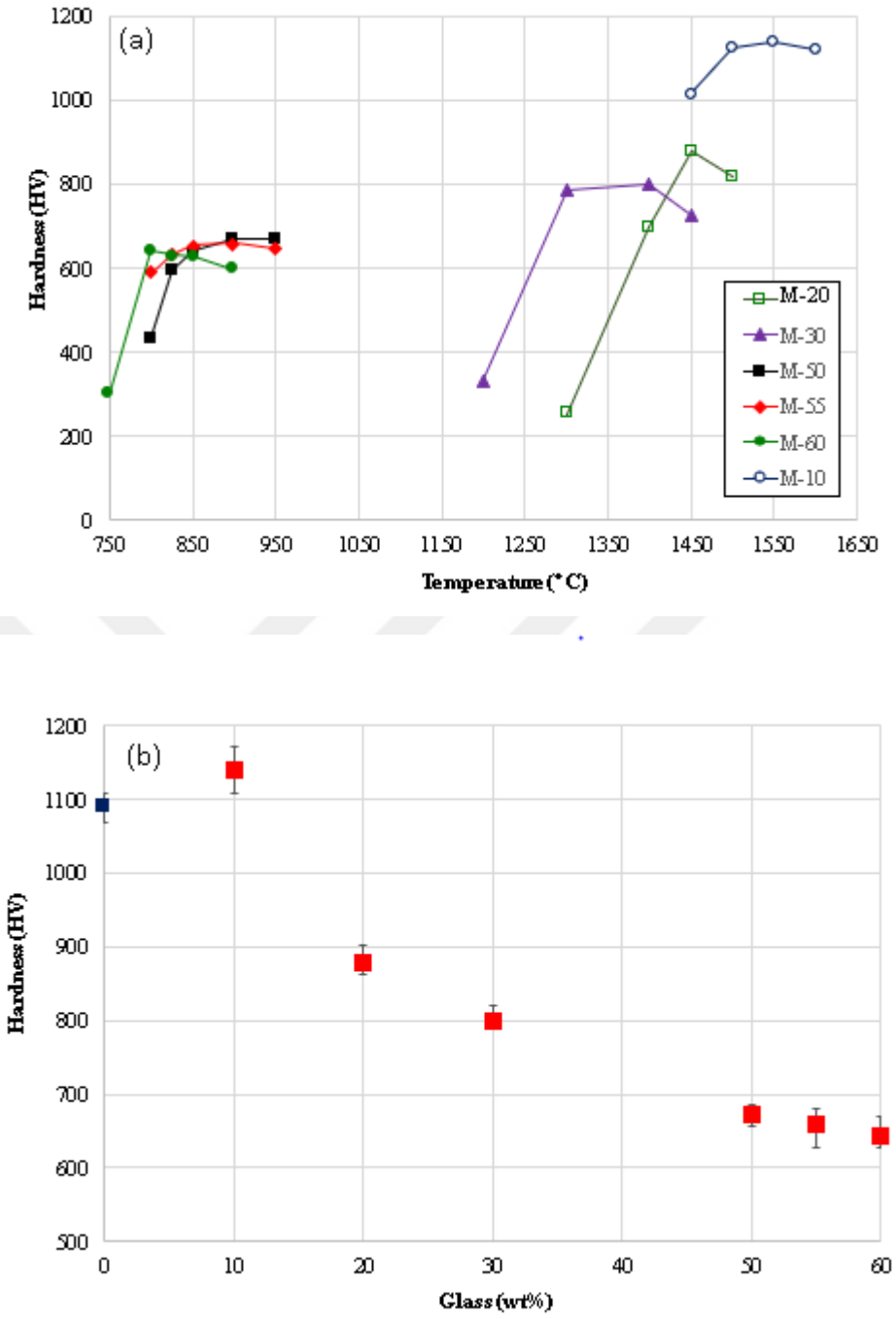

Figure 5.12 Hardness of the mullite/glass composites: (a) Sintered at different temperatures; (b) Sintered at optimum temperature for each composition.

Figure 5.13 shows fracture toughness of the mullite/glass composites sintered at optimum temperature for each composition. Mullite (0 wt% glass) and glass (100 wt% glass) are the end members and are given for a better evaluation of the composite behavior. In the calculations of the fracture toughness values, the elastic modulus for

each set measured was used in Equation 2.5. The fracture toughness of polycrystalline mullite is about 2.5 MPa.m$^{1/2}$ [77] and for silicate glasses it is between 0.7-0.9 MPa.m$^{1/2}$ [28]. Similar to the literature values, the fracture toughness of mullite and glass was reported as 2.5 MPa.m$^{1/2}$ [102] and 1.0 MPa.m$^{1/2}$ [71], respectively.

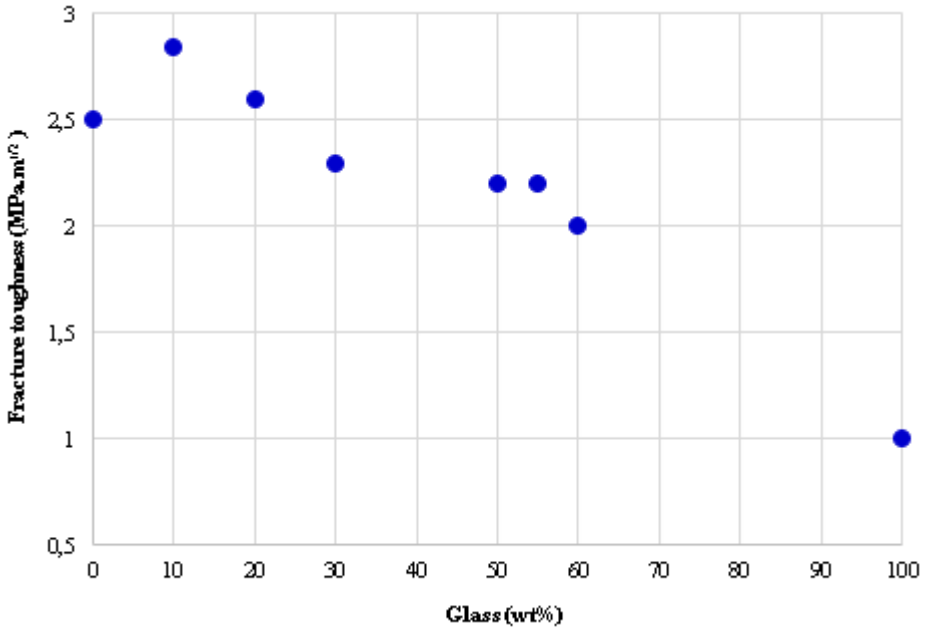

Figure 5.13 Fracture toughness of the mullite/glass composites sintered at optimum sintering temperature for each composition.

The fracture toughness increased from 2.5 MPa.m$^{1/2}$ for mullite to 2.84 MPa.m$^{1/2}$ for the M10. Then, it decreased to 2.3 MPa.m$^{1/2}$ for the M30 and to 2 MPa.m$^{1/2}$ for the M60. The M50, M55 and M60 composites are sintered by viscous sintering and do not possess distinct grain boundaries, unlike the M10 to M30. Figure 5.14 shows SEM images of the cracks at different magnification in the M10 and M60. The M10 sintered at 1550 °C had coarsened as well as faceted/elongated mullite grains within the glass matrix and the crack pathway was like a crooked line, which was an indication of more energy absorption and preferential pathway thru the intergranular glassy phase by means of crack bridging and deflection by the mullite grains (Figure 5.14 (a-b)). Bigger mullite grains located nearly perpendicular to the crack pathway direction absorbed energy and were broken. Similar results were reported for the Al_2O_3/glass composites [103]. As the glass content increased, crack propagation pathways became

much straighter in the composites. The crack pathway became almost straight in the M60 with nearly no crack bridging and deflection due to the dominant glassy phase (Figure 5.14 (c-d)). In glasses, the crack pathway is very flat because glasses have easy cleavage planes and low fracture toughness due to lack of grain boundaries [103] [114]. Hence, the fracture toughness of M10 and M20 was improved due to an optimal glass addition in such a way to induce densification at a lower temperature than mullite as well as providing a very near grain-to-grain distance to efficiently bridge or deflect crack. As a result, the fracture toughness decreases with an increasing amount of glass phase in the composites. The overall properties of the mullite/glass composites sintered at optimum sintering temperature for each composition are summarized in Table 5.1.

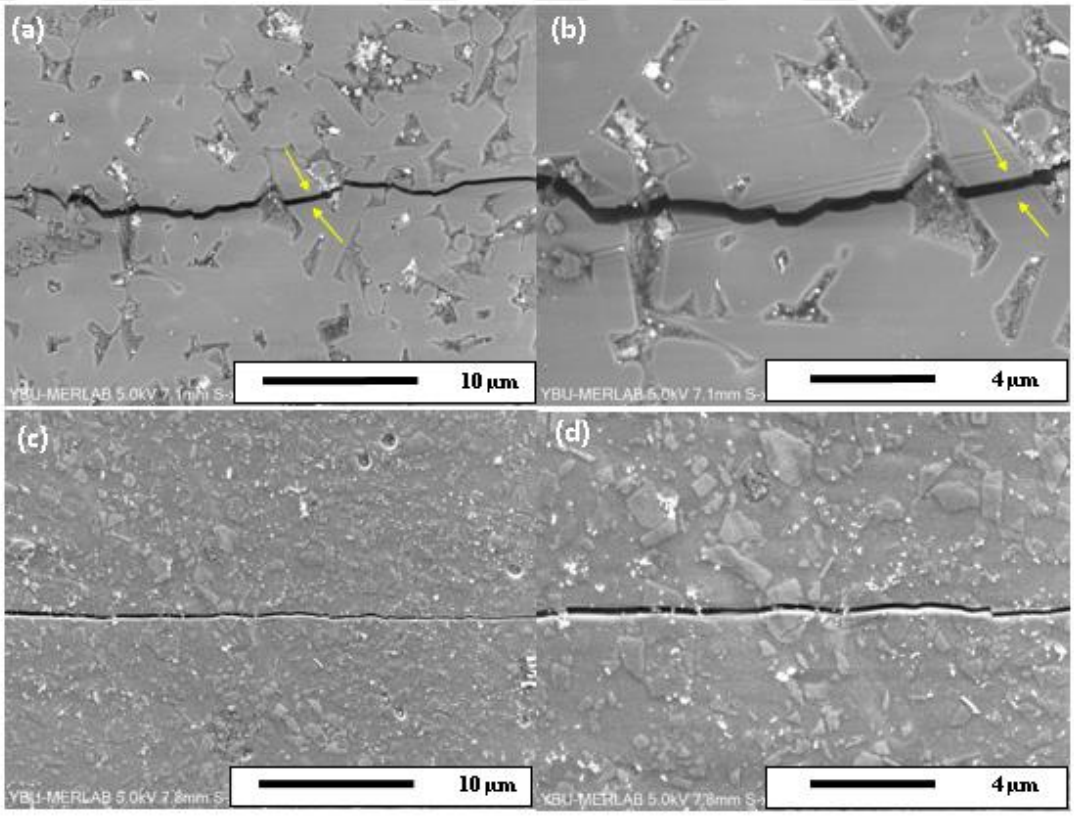

Figure 5.14 Backscattered SEM images of the cracks formed by indentation a) M10, b) higher magnification of M10, c) M60 and d) higher magnification of M60

Table 5.1 Full properties of the composites sintered at their optimum sintering temperatures for each composition.

			Dielectric Properties		Thermal Properties			Mechanical Properties			
Composition	Optimum Sintering Temperature (°C)	Density (g/cm^3)	Dielectric Constant, at 5 MHz	Dielectric Loss, at 5 MHz	Thermal Conductivity (W/m.K) (at 25°C)	Thermal Expansion Coefficient, CTE (ppm/°C) (25-800°C)	Glass Transition Temperature, T_g (°C)	TSR (R, ΔT) (°C)	Hardness (HV)	Elastic Modulus (GPa)	Flexural Strength (MPa)
Mullite [102]	1550	3.06	7.4	0.0031	6.07	5.26	-	142	1070-1120	185	182
M10	1550	2.99	7.29	0.0028	4.45	4.61	722.9	157	1140±33	189±8	180±49
M20	1450	2.86	7.12	0.0025	3.72	4.27	709.1	162	879±23	165±6	151±21
M30	1400	2.76	6.98	0.0013	2.2	4.25	700.8	153	800±30	131±4	112±10
M50	850	2.64	6.79	0.0043	2.11	4.60 3.93 (25-300°C)	642.5	146	673±11	107±4	95±21
M55	825	2.63	6.68	0.0037	1.47	4.75 4.01 (25-300°C)	650.4	144	660±14	102±3	92±19
M60	825	2.6	6.71	0.0021	1.55	4.61 3.93 (25-300°C)	647	149	642±10	98±4	89±20
Glass	750[71]	2.43 [71]	6.37 [71]	0.0016 [71]	0.85[38]	0.55[28]	-	-	591±33	70[28]	87[28]

In summary, glass (10-60 wt%)/mullite composites were successfully fabricated for the radome and LTCC applications. The optimum densification temperatures decreased from 1550°C (for 10 wt% glass) to 1400°C (for 30 wt% glass), to 850°C (for 50 wt% glass), and to 825°C (for 55 and 60 wt% glass). XRD results showed that the main crystalline phase was mullite, but in-situ crystallized anorthite phase formed in the samples with 50 to 60 wt% glass after 825°C. The dielectric constant (loss) of the composites were 7.29 (0.0028) for 10 wt% glass and 6.71 (0.0021) for 60 wt% glass at 5 MHz, respectively. Thermal conductivity decreased with increasing glass content from 4.45 W/m·K (10 wt% glass) to 1.55 W/m·K (60 wt% glass). Glass addition also decreased the mechanical properties of the composites such as hardness from HV 1140±33 (10 wt% glass) to 642±10 (60 wt% glass), flexural strength from 180±49 MPa (10 wt% glass) and 89±20 MPa (60 wt% glass), and elastic modulus from 189±8 GPa (10 wt% glass) to 98 ±4 GPa (60 wt% glass). Table 5.1 summarizes full properties of the composites sintered at their optimum temperatures for each composition. Note that mullite and glass are end members given to compare the properties of the composites. The thermal shock parameter (TSR) of the composites were calculated using experimentally determined parameters at room temperature using Equation 1.4. Lower elastic modulus and CTE of the M10, M20, and M30 composites significantly increase the parameter from a thermomechanical parameters perspective. The composite with 20 wt % glass was a suitable candidate for the radome applications due to its lower elastic modulus and low thermal expansion coefficient together with low dielectric properties. The composite with 55 wt% glass was a suitable candidate for the low temperature co-fired ceramic applications due to its lower densification temperature (<950°C), lower dielectric properties, and a thermal expansion coefficient matched to Si together with optimized mechanical properties.

CHAPTER 6

MECHANICAL, THERMAL AND DIELECTRIC PROPERTIES OF MULLITE/GLASS/NANO FILLER (hBN and AlN) COMPOSITES

In Chapter 5, it was explained the reasons why Al_20_3 was replaced with mullite and then the resulting physical properties were correlated with the compositions. The M55 (e.g., 55 wt% glass/mullite) was densified at 825 °C and had a dielectric constant of 6.68 at 5 MHz as well as a low thermal conductivity of 1.47 W/m·K at 25ºC. In this chapter, therefore, the composite composition was engineered to improve thermal properties without increasing densification temperature and degrading other properties. Nano hBN and nano AlN filler were chosen and added at 1 wt% (M55-1hBN, M55-1AlN), 2.5 wt% (M55-2.5hBN, M55-2.5AlN), 5 wt% (M55-5hBN, M55-5AlN) and 10 wt% (M55-10hBN, M55-10AlN) to the base M55 composition because hBN and AlN have very high thermal conductivities ((20-23 W/m·K for the //c and 111-137 W/m·K for the ⊥c for hBN [78][79] and 320 W/m·K for AlN[81]) and low-to-moderate dielectric properties (i.e., 4–4.4 at 1 MHz [80][83] and dielectric loss = 0.0003 at 1–10 GHz for hBN [63] and dielectric constant (loss) = 8.6-9.2 (0.05–0.001) for AlN [82])). Densification, phase formation, dielectric properties (dielectric constant and loss), mechanical properties (hardness, flexural strength, elastic constant) and thermal properties (thermal conductivity and thermal expansion coefficient) were investigated in detail to understand the nano filler effects on the base M55 composites for the LTCC applications.

6.1 Mullite/Glass/Nano hBN

6.1.1 Densification

Figure 6.1 compares densification and AP of the composites as a function of hBN content and temperature. The green samples were produced by tape casting. The optimum densification temperatures were decided by considering high bulk density

and porosity level. The optimum sintering temperature and bulk density of the composites were determined as 825 °C (2.63 g/cm^3, AP = 0.19% and WA = 0.17%) for the M55, 825 °C (2.59 g/cm^3, AP = 0.10% and WA =0.06 %) for M55-1hBN, 825 °C (2.54 g/cm^3, AP = 0.92% and WA = 0.36%) for the M55-2.5hBN, 825 °C (2.46 g/cm^3, AP = 0.19 % and WA = 0.07%) for the M55-5hBN and 900 °C (2.3 g/cm^3, AP = 0.46% and WA = 0.28%) for the M55-10hBN. Also, relative densities were calculated based on their theoretical densities as determined by logarithmic mixture equation [84], using the theoretical densities of 3.13 g/cm^3 for mullite [102], 2.43 g/cm^3 for glass [71] and 2.1 g/cm^3 for hBN [83]. The relative densities of the M55, M55-1hBN, M55-2.5hBN, M55-5hBN and M55-10hBN were 99.2%, 97.73%, 96.22%, 93.89% and 89.14% respectively, which indicates that hBN addition decreases the (bulk) relative densities. Although the AP values of the samples were very close to zero, lower (bulk) relative densities with increasing hBN content might be attributed to the increased numbers of closed pores (closed porosity, CP=total porosity-AP), that is, total porosity (i.e., 100-relative density) was 0.8% (AP=0.19%, CP=0.61%) for the M55, 2.27% (AP=0.10%, CP=2.17%) for the M55-1hBN, 3.78% (AP=0.92%, CP=2.86%) for the M55-2.5hBN, 6.10% (AP=0.20%, CP=5.91%) for the M55-5hBN and 10.86% (AP=0.46%, CP=10.40%) for the M55-10hBN. It is evident that the CP increases significantly from 0.61% for the M55 to 10.40% for the M55-10hBN, although the AP is less than 0.92%. In general, as the hBN content was increased, the bulk densities decreased due to the lower density of hBN. Moreover, densification was delayed to 900 °C for the M55-10hBN composite. These results showed that a homogeneous particle packing in the green sample was achieved by tape casting due to the dispersion of the plate-like hBN particles, which allowed high hBN loading into the mullite/glass structure without exceeding densification temperature >950 °C. Similar effects of hBN particles on densification have been reported in literature for barium aluminasilicate ($BaAl_2Si_2O_8$, BAS)/hBN (10 to 50 wt%) composites produced by hot pressing at 1500 °C [85]. The bulk density of the composites decreased from 3.18 g/cm^3 at 10 wt% hBN without visible micro cracks to 2.22 g/cm^3 at 50 wt% hBN with evident cracks and voids [85]. Cho et al [86] reported that the plate-like hBN in AlN (5-20 vol%)-hBN ceramics triggered the formation of porosity, resulting in limited densification. Because LTCC technology requires a tape-casting process to fabricate thin dielectric layers, the

production of dense composites with high hBN loading by tape casting is very important.

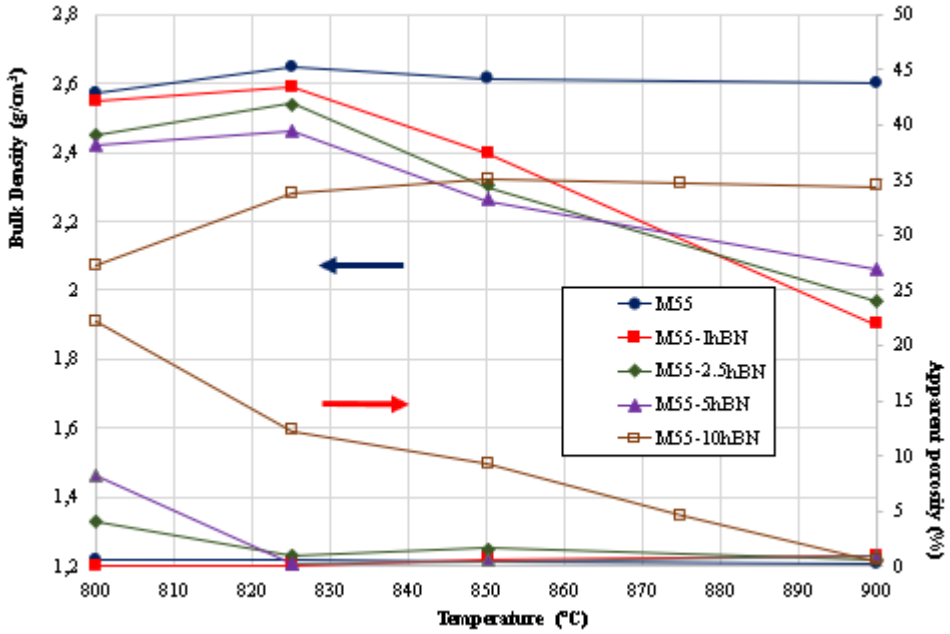

Figure 6.1 Densification of the samples as a function of hBN content and temperature

6.1.2 Phase formation and microstructure evolution

SEM images of the mullite/glass/hBN samples (1-10 wt% hBN) sintered at optimum temperatures are shown in Figure 6.2. Mullite particles (or grains) are homogeneously dispersed in the dense M55 microstructure (Figure 6.2 (a)) where the microstructure is in the form of a "sea-island structure", and the boundaries between glass and ceramic phases are clearly distinguishable. Some near-spherical pores on the surfaces were more evident with increasing hBN content. These are in fact closed pores emerged after polishing. In general, addition of hBN mainly reduces the overall hardness due to its low intrinsic hardness. Similar results were obtained in hot pressed hBN/Si_3N_4 composites such that hardness considerably decreased with increasing hBN content (e.g., from 14.9 GPa (1 wt% hBN and density of 3.37 g/cm^3) to 7.7 GPa (5 wt% hBN and density of 3.03 g/cm^3) [100] . Since hBN has a large specific surface area and plate-like morphology, distinct boundaries between glass phase and ceramic particles started fading away with increasing hBN content (i.e., disappearance of sea-island

structure) when more hBN particles were aligned during tape casting. In other words, a uniform light-gray color dominates or the contrast between mullite and glass is lost as the amount of hBN increases. Because hBN particles are thin and transparent, it is hardly possible to locate them on the surface microstructures. Therefore, SEM images of the M55-10hBN at higher magnifications are shown in Figure 6.3. The plate-like hBN particles were aligned and covered a large in-plane area within the microstructure, as shown by the arrows. In fact, alignment of plate-like hBN particles between mullite and glass phases form a heat-conducting paths, thereby helping form highly heat-conducting channels.

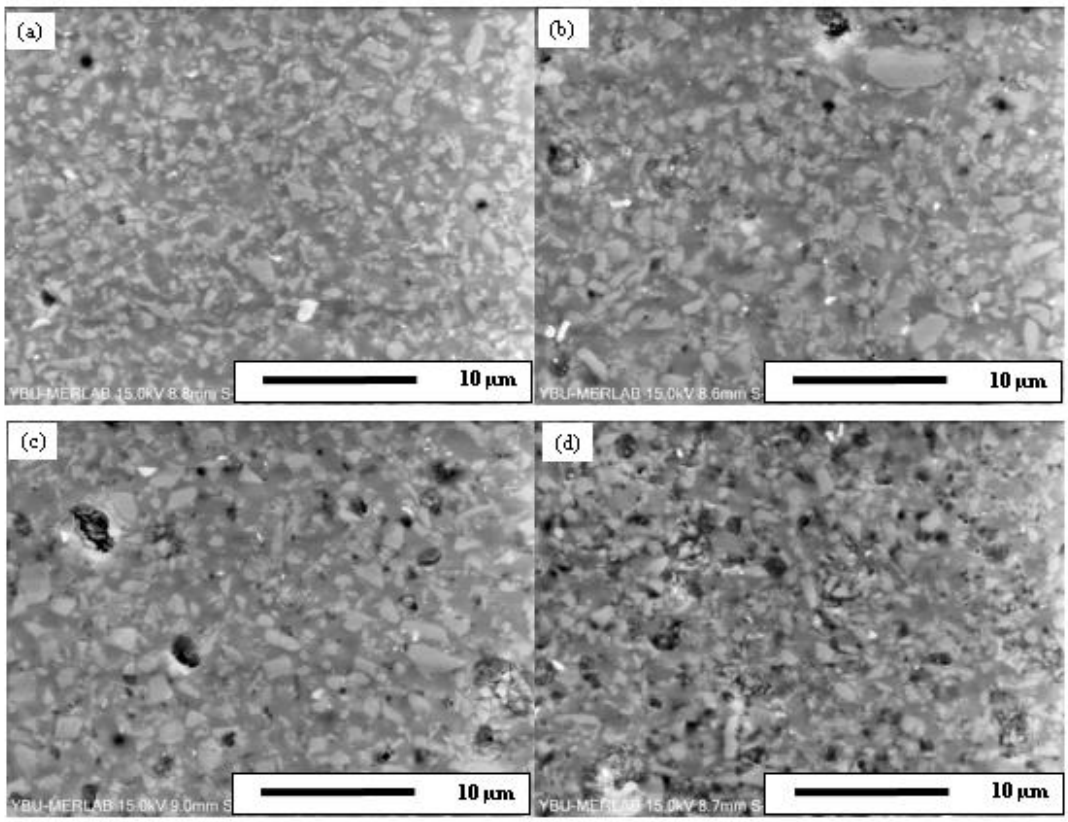

Figure 6.2 SEM images of the composites (a) M55, (b) M55-1hBN, (c) M55-2.5hBN, (d) M55-5hBN, and (e) M55-10hBN

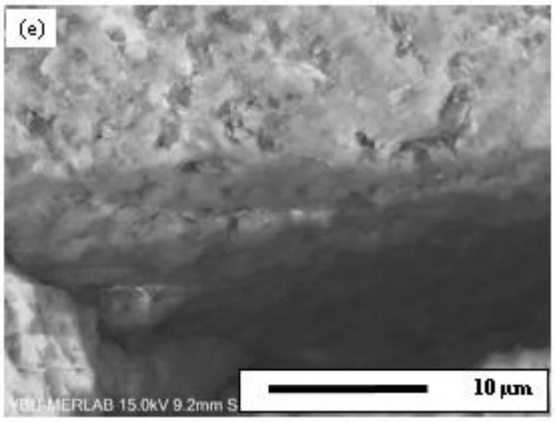

Figure 6.2 (continued) SEM images of the composites (a) M55, (b) M55-1hBN, (c) M55-2.5hBN, (d) M55-5hBN, and (e) M55-10hBN

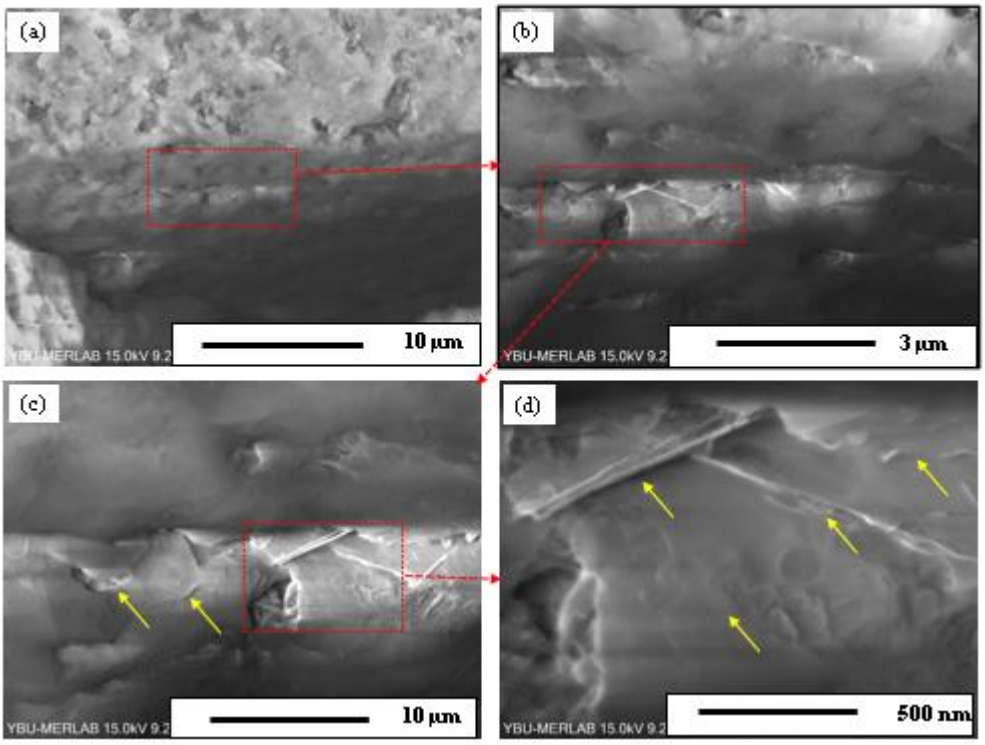

Figure 6.3 High magnification SEM images of the M55-10hBN (a) 5k, (b) 25k, (c) 25k, and (d) 80k

Figure 6.4 shows XRD patterns of the composites sintered at optimum temperatures (825 °C for the M55, 825 °C for the M55-1hBN, 825 °C for the M55-2.5hBN, 825 °C for the M55-5hBN and 900 °C for the M55-10hBN). Anorthite $(Ca,Na)(Si,Al)_4O_8$, Card number: 00–041-1481) and hBN (Card number: 01–074-1977) phases are also

marked on the patterns. Mullite (Card number: 01-074-1977) was the main crystalline phase with the highest intensity for each composition except for the M55-10hBN. Anorthite crystallization was more noticeable from the M55 towards the M55-5hBN. The intensity ratio of the anorthite peak at 2θ~28.08° to the mullite peak at 2θ~26.16° (i.e., $I_{Anorthite}/I_{Mullite}$) was used to qualitatively calculate the temperature dependent anorthite crystallization. The anorthite ratio increased from 0.07 for the M55-1hBN to 0.12 for the M55-5hBN with increasing hBN content at the same temperature. However, the anorthite peak intensity significantly increased to 1.01 and dominated the pattern for the M55-10hBN sintered at 900 °C, which states that hBN served as heterogeneous nucleation sites for anorthite crystallization due to its large surface area [85]. In addition, it was reported that anorthite crystallization is dependent on both glass content and temperature such that both high temperature and high glass content promote more anorthite crystallization [115]. These results indicate that higher temperature causes more crystallization. In literature, the temperature at which the anorthite phase begins to form has been determined as 825 °C. However, the main hBN peak intensity at 2θ=26.8° increases from the M55-1hBN to M55-10hBN, indicating that hBN neither chemically reacted with other phases nor decomposed with temperature. This is important because hBN chemical stability is critical to reduce dielectric constant as well as to increase thermal conductivity of the composites, which is extremely necessary for the LTCC applications.

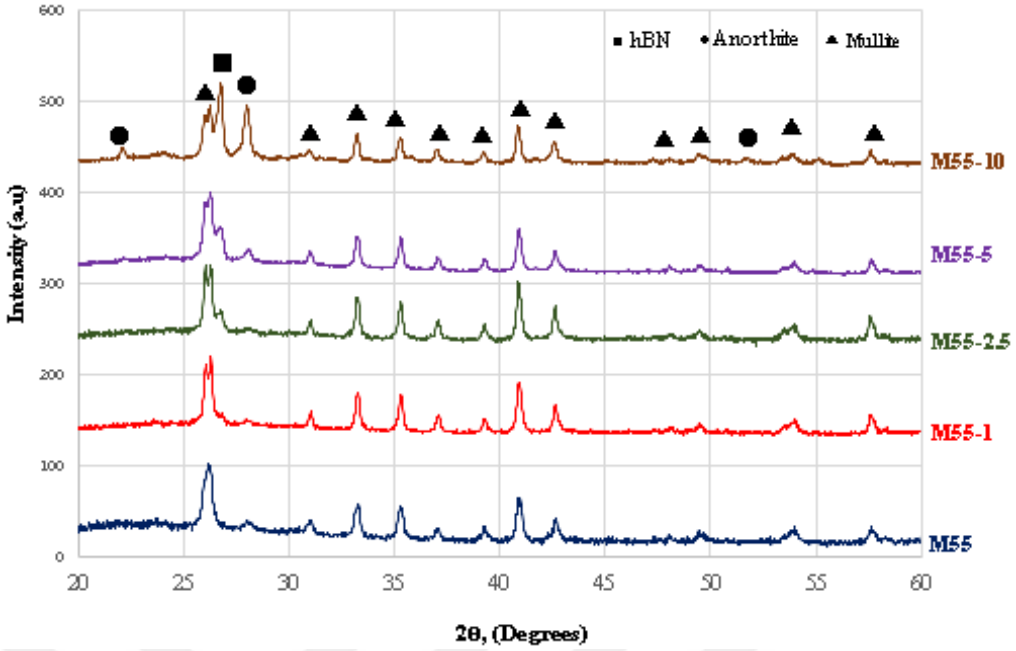

Figure 6.4 XRD patterns of the tape-casted samples sintered at optimum temperature

6.1.3 Dielectric properties

The dielectric properties of a material are dependent mainly on several factors such as glass content, porosity (or densification) and crystalline phases present. Figure 6.5 shows the hBN dependence of dielectric constant (K) and loss measured at 5 MHz for the samples sintered at optimum temperature. Note that K (loss) = 7.4 (0.0031)[102] and K (loss)=6.37 (0.0016) [71] at 5MHz for mullite and glass end compositions, respectively. The K (loss) values at 5 MHz were 6.68 (0.0037) for the M55, 6.34 (0.006) for the M55-1hBN, 5.95 (0.004) for the M55-2.5hBN, 5.66 (0.0021) for the M55-5hBN, and 5.13 (0.003) for the M55-10hBN. Because all samples had almost near zero AP (i.e., less than 0.92%) and WA (i.e., less than 0.36%), the decrements (or, alternatively, enhancement) in the K can be partly attributed to the lower K of hBN (K = 4–4.4 at 1 MHz [80][83], K = 4.5 at 1–10 GHz [63]). Similar to the effects of porosity and in-situ anorthite on dielectric properties for the A55-hBN (1-10 wt%) compositions as described in Chapter 4, closed porosity is also dominant parameter to decrease the K with increasing hBN content. Figure 6.5 also reveals that low dielectric loss of hBN (0.0003 at 1–10 GHz [63]) mostly decreased dielectric loss with increasing the hBN content. A similar decrease in dielectric loss was observed in $MgSiO_3$–SiO_2–

hBN composites [116]. These results prove that dielectric properties were successfully decreased (or improved) by adding 10 wt% hBN with respect to the base M55 composite. A K value as low as possible is strongly desired because it is the parameter that directly affects signal propagation delay in the LTCC electronic packages (see Equation 1.8). In other words, signal transmission speed increases with decreasing K.

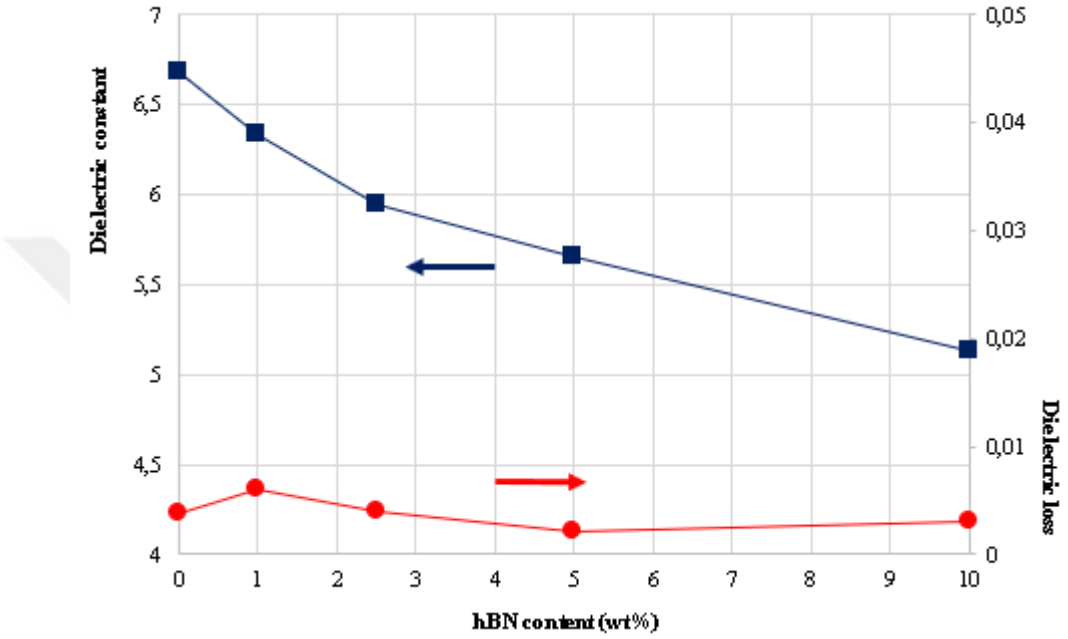

Figure 6.5 Dielectric properties measured at 5 MHz for the samples sintered at optimum temperature for each composition

6.1.4 Thermal properties

In LTCC applications, high thermal conductivity (k) is highly desired for a more reliable and more efficient packaging to dissipate heat generated during service, particularly for high-density and high-power devices operating at high speeds [40] [91]. A thermal expansion coefficient (CTE) match or is close to Si (~2.6–3.3 ppm/°C) is very important parameter to prevent failure of melting connections between chip and substrate [97]. Figure 6.6 compares k and CTE of the composites sintered at optimum temperature for each composition. The CTE were calculated between 25-300 °C and 25-800 °C because the former is important for the LTTC and the latter is important for the radome applications. It has been reported that k = 6.07 W/m·K [77]

and k = 0.85 W/m·K [38] at 25 °C for mullite and glass, respectively. The k of the composites sharply increased as the hBN content increased from the M55 to the M55-5hBN and then nearly stabilized up to the M55-10hBN. The hBN crystal structure allows anisotropic physical properties such that the k values are 20-23 W/m·K for the //c and 111-137 W/m·K for the ⊥c [78][79]. Note that hBN c-axis was parallel to the thermal conductivity measurement direction for the M55-1hBN to M55-10hBN samples. Similar to the effect of porosity for the A55-hBN (5-10 wt%) compositions as described in Chapter 4, improvement in k is not as high as expected despite a high thermal conductivity of hBN along the //c because of a very low thermal conductivity of air (0.0267 W/m·K [92]) due to closed porosity. A similar trend has been reported in the hBN/BAS systems at high hBN loadings such that k increased from 2.5 W/m·K (10 wt% hBN) to 7.2 W/m·K (50 wt% hBN) at 100 °C [95].

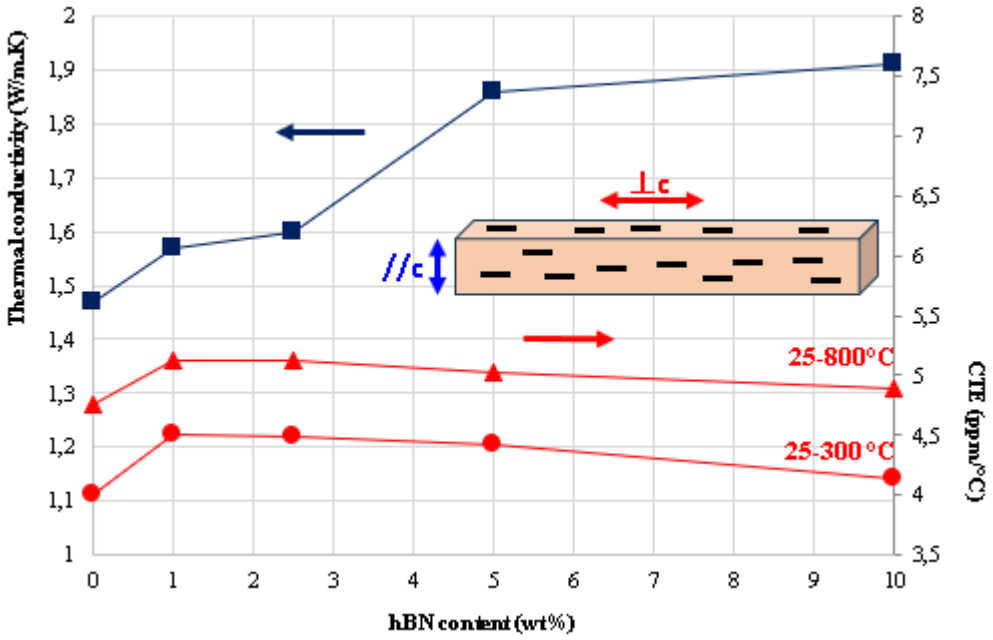

Figure 6.6 Thermal conductivity and thermal expansion coefficient of the composites sintered at optimum temperature for each composition

The CTE values slightly increased from 0 wt% hBN (M55) to 1 wt% hBN (M55-1hBN), and then decreased towards 10 wt% hBN (M55-10hBN). However, the CTE of the composites remained in a narrow range between 4.01 ppm/°C for the M55 and 4.14 ppm/°C for the M55-10hBN for a temperature range of 25-300 °C. Similarly, it

remained in between 4.75 ppm/°C for the M55 and 4.89 ppm/°C for the M55-10hBN for a temperature range of 25-800 °C. In addition, in-situ crystallized anorthite has a CTE of 4.82 ppm/°C [99], which does not alter the final CTEs of the composites. Note that hBN c-axis was perpendicular to the CTE measurement direction in the M55-1hBN to M55-10hBN samples. hBN has a CTE of 2.3-2.4 ppm/°C for the ⊥c and 11.3-15.6 ppm/°C for the //c [78][79] which definitely helps match the final CTE of the composites to Si. In fact, hBN possesses a small negative CTE such that it is -2.72 ppm/°C for the ⊥c and 37.7 ppm/°C for the //c at room temperature [98]. Therefore, a much lower CTE value of the aligned hBN particles perpendicular to the c-axis lowered the overall CTE of the composites (i.e., particularly, for the M55-10hBN). In addition, in-situ crystallized anorthite helped lower the CTE of the M55-10hBN due to its low CTE of 4.82 ppm/°C [99]. The glass transition temperatures (T_g) were determined as 650 °C for the M55, 648 °C for the M55-1hBN, 649 °C for the M55-2.5hBN, 651 °C for the M55-5hBN and 607 °C for the M55-10hBN. As explained in Chapter 4 and Chapter 5, these Tg values are way above the test conditions of heat exposure (1000 hours at 150 °C) and temperature cycle test (from room temperature to 125 °C) [40].

6.1.5 Mechanical properties

Optimization of the mechanical properties is extremely important because thin LTCC substrates can easily be broken during the manufacturing process or actual usage. Figure 6.7 shows hardness of the composites sintered at optimum temperatures. The hardness of the composites continuously decreased with increasing hBN amount. In other words, the hardness values were 660±14 HV for the M55, 608±4 HV for the M55-1hBN, 566±6 HV for the M55-2.5hBN, 472±8 HV for the M55-5hBN, and 262±13 HV for the M55-10hBN. In general, addition of hBN decreases hardness mainly due to its low hardness because the hardness values of mullite and glass are 1059 HV [102] and 591 HV [71], respectively. In addition, closed porosity that increases with increasing hBN content degrades the hardness because it weakens the whole structure, as explained in Chapter 4. Similar results were obtained in hot pressed hBN/Si_3N_4 composites such that hardness considerably decreased with increasing hBN

content (e.g., from 14.9 GPa (1 wt% hBN and density 3.37 g/cm^3) to 7.7 GPa (5 wt% hBN and density 3.03 g/cm^3) [100].

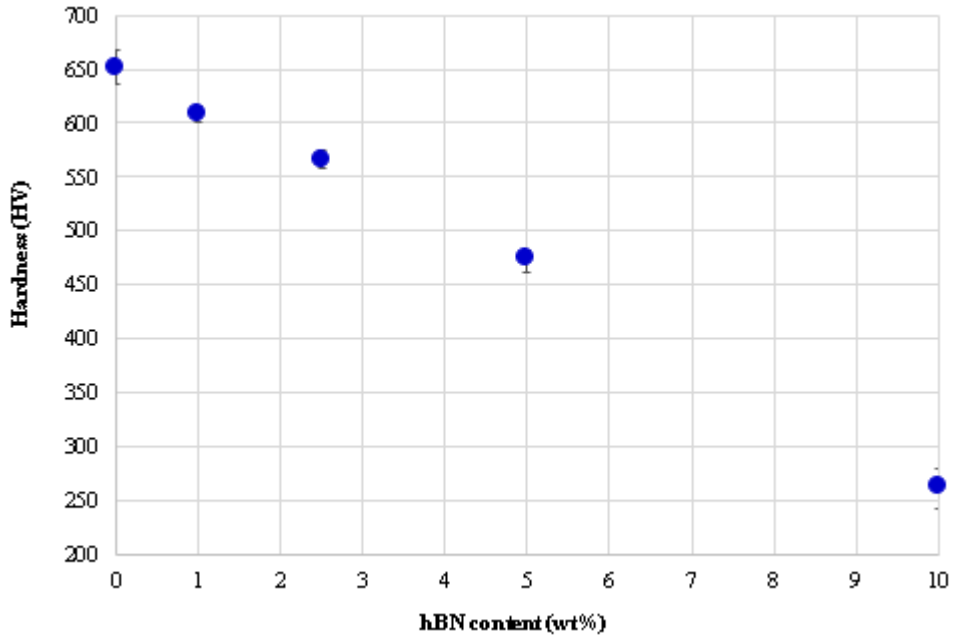

Figure 6.7 Hardness values of the composites sintered at optimum temperature for each composition

Figure 6.8 shows elastic modulus of the composites sintered at optimum temperatures. The elastic modulus of mullite and glass are 185 GPa [102] and 70 GPa [28], respectively. In general, the mean elastic modulus decreased with increasing hBN content. In other words, the elastic modulus values were 102±3 GPa for the M55, 98±4 GPa for the M55-1hBN, 89±8 GPa for the M55-2.5hBN, 84±2 GPa for the M55-5hBN, and 70±7 GPa for the M55-10hBN. Similar effects of the platelet hBN particles on elastic modulus were reported in barium aluminasilicate ($BaAl_2Si_2O_8$, BAS)/hBN (10 to 50 wt%) composites fabricated by hot pressing at 1500 °C [85] such that it decreased from 86 GPa at 10 wt% hBN (AP= 0.02%) without any visible micro cracks to 46 GPa at 50 wt% hBN (AP= 4%) with cracks and voids. Figure 6.9 shows flexural strength values of the composites sintered at optimum temperatures. The flexural strength of mullite and glass are 182 MPa [102] and 87 MPa [28], respectively. In general, the flexural strength first decreased at the M55-1hBN and then slightly increased and remained almost constant up to the M55-10hBN. In other words, the flexural strength

was 92±19 MPa for the M55, 50±6 MPa for the M55-1, 68±7 MPa for the M55-2.5 MPa, 69±8 MPa for the M55-5, and 71±6 MPa for the M55-10.

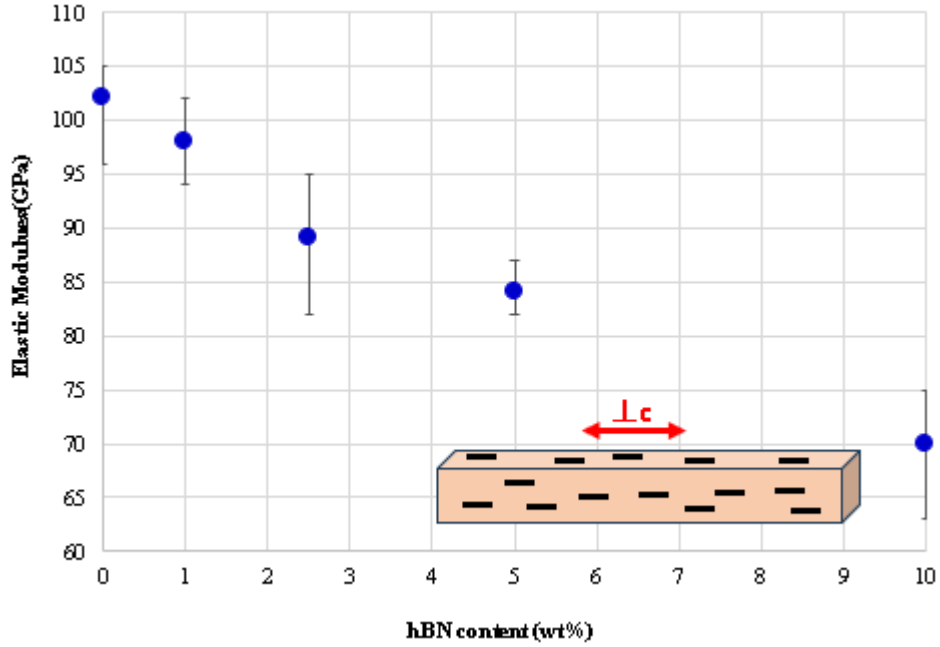

Figure 6.8 Elastic modulus of the composites sintered at optimum temperature for each composition.

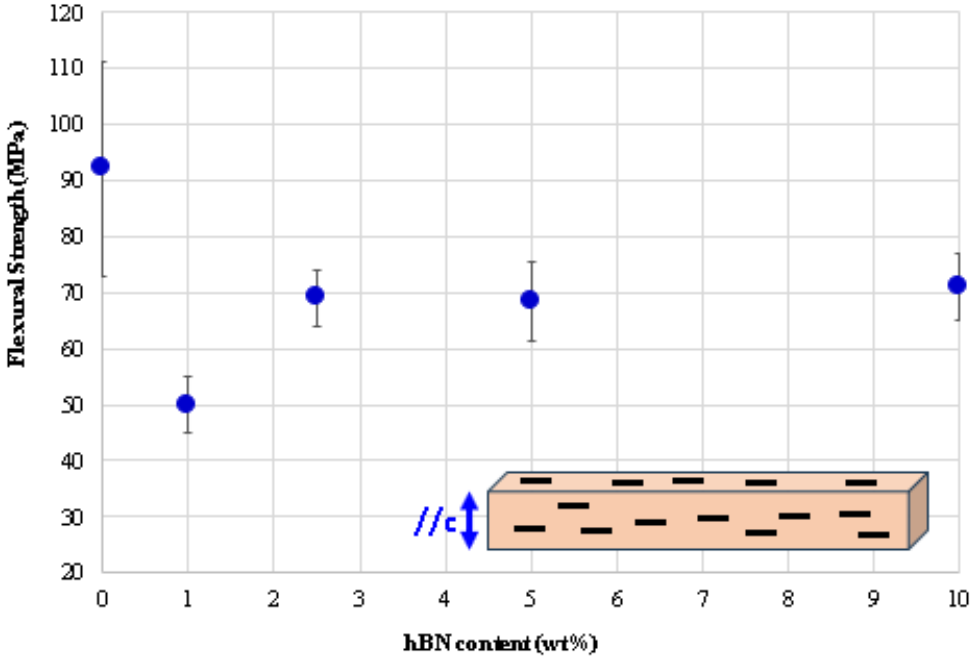

Figure 6.9 Flexural strength of the composites sintered at optimum temperature for each composition

Elastic modulus and flexural strength measurements were taken from the as-sintered samples, as explained in Chapter 4. Although elastic modulus and flexural strength were measured from the same bar-shaped ceramics, the measurements were the ⊥c for the elastic constant and the //c for the flexural strength in the tape-casted M55-1hBN to M55-10hBN samples. Flexural strength of ~ 82-138 MPa for the //c and ~18-34 MPa for the ⊥c, and elastic modulus of ~ 62-82 GPa for the //c and ~ 8-25 GPa for the ⊥c were reported for highly-textured hBN ceramics [78][79] due to weak van der Waals forces in-between the layers (//c) and strong sp^2 covalent bonds in the layers (⊥c). Therefore, elastic constant should decrease and flexural strength should increase due to anisotropic properties of the aligned hBN particles. In addition to the anisotropic properties of the hBN structure, densification (and closed porosity) levels are also critical for mechanical properties because the presence of defects such as pores in the structure leads to lower mechanical properties [101]. Figure 6.8 indicates that elastic constant continuously decreases that is consistent with the hBN anisotropy, but a relatively more decrease in the M55-10hBN is consistent with more closed porosity. Figure 6.9 indicates that a sharp decrease in flexural strength for the M55-1hBN might be attributed to the smaller number of oriented hBN particles that are, in fact, could not support the structure; rather, behave as crack initiation and propagation sites, although it is very difficult to detect individual hBN particles in the microstructure (see in Figure 6.2b). More analytical characterization techniques such as TEM must be conducted to understand the physical basis. Improvement of the flexural strength up to the M55-10 hBN is consistent with the hBN anisotropic properties as well as mechanical support of more aligned hBN particles, but relatively lower value for the M55-10 hBN is due to higher closed porosity level. Qian Li et al. [85] reported the hBN/BAS composites that the flexural strength was enhanced from 160 MPa for the 10 wt% hBN to 193 MPa for the 30 wt% hBN due to the hBN plate-like shape providing a good strengthening effect. It is important to note that as-sintered ceramics were used for elastic constant and flexural strength measurements, which could also give rise to property variations in case of the presence of microcracks on the surfaces. The overall properties of the mullite/glass/hBN composites sintered at optimum sintering temperature for each composition are summarized in Table 6.1.

Table 6.1 Summary of physical properties of the composites sintered at their optimum sintering temperatures for each composition

			Dielectric Properties		Thermal Properties		Mechanical Properties		
Composition	Sintering temperature (°C)	Density (g/cm^3)	Dielectric constant	Dielectric loss	Thermal conductivity (W/m.K) (at 25°C)	Thermal Expansion Coefficient, CTE (ppm/°C) (25-300°C)	Hardness (HV)	Elastic Module (GPa)	Flexural Strength (MPa)
MS5	825	2.64	6.68	0.0037	1.47	4.01	660±14	102±3	92±19
MS5-1 hBN	825	2.59	6.34	0.0060	1.57	4.51	608±4	98±4	50±6
MS5-2.5 hBN	825	2.54	5.95	0.0040	1.6	4.48	566±6	89±8	69±7
MS5-5 hBN	825	2.46	5.66	0.0021	1.86	4.42	473±8	84±2	68±8
MS5-10 hBN	900	2.3	5.13	0.0030	1.91	4.14	262±13	70±7	71±6

6.2 Mullite/Glass/Nano AlN

6.2.1 Densification

Figure 6.10 compares the densification and apparent porosity (AP) of the composites as a function of temperature and AlN content. Straight lines are drawn to guide eye. For each composite, the optimum densification temperature was decided by considering high bulk density as well as near zero AP and water absorption (WA), as calculated from the Archimedes' method. The optimum densification temperatures were 825 °C for the M55 (2.63 g/cm^3, AP=0.19% and WA=0.17%), 800 °C for the M55-1AlN (2.61 g/cm^3, AP=0% and WA=0%), 800 °C for the M55-2.5AlN (2.57 g/cm^3, AP=0.27% and WA=0.09 %), 825 °C for the M55-5AlN (2.53 g/cm^3, AP=0.12% and WA= 0.04%), and 825 °C for the M55-10AlN (2.48 g/cm^3, AP=0.72% and WA=0.28%). Also, relative densities were calculated by dividing the bulk densities of the compositions by their theoretical densities as determined by logarithmic mixture equation [84], using the theoretical densities of 3.13 g/cm^3 for mullite [102], 2.43 g/cm^3 for glass [71] and 3.26 g/cm^3 for AlN [81]. The relative densities of the M55, M55-1AlN, M55-2.5AlN, M55-5AlN and M55-10 AlN were 99.2%, 99.0%, 97.3%, 95.4% and 92.9% respectively, which indicates that AlN addition decreases the (bulk) relative densities. A similar effect of AlN on densification was reported for the cordierite-based glass/ceramic composites and it was reported that relative density decreased from 99.7% (0 wt% AlN) to 97.2% (50 wt% AlN) [117]). Also, Yuan et al [118] investigated CaO–BaO–Al_2O_3–B_2O_3–SiO_2 (CBABS)/AlN addition (30 to 60 wt%) produced by tape casting and reported that bulk density decreased from 2.95 g/cm^3 at 30 wt% AlN to 2.10 g/cm^3 at 60 wt% AlN. Overall, the bulk density, AP, and WA values for each composite varied slightly at temperatures between 800 °C and 900 °C, indicating that densification for each composite was completed at temperatures close to the softening temperature of the glass matrix phase (i.e., 852 °C) due to viscous sintering. Although the AP values of the samples were very close to zero, lower (bulk) relative densities with increasing AlN content might be attributed to the increased numbers of closed pores (closed porosity, CP=total porosity-AP), that is, total porosity (i.e., 100-relative density) was 0.80% (AP=0.19%, CP=0.61%) for the M55, 1% (AP=0%, CP=1%) for the M55-

1AlN, 2.7% (AP=0.27%, CP=2.43%) for the M55-2.5AlN, 4.6% (AP=0.12%, CP=4.48%) for the M55-5AlN and 7.1% (AP=0.72%, CP=6.38%) for the M55-10AlN. It is evident that the CP increases significantly from 0.61% for the M55 to 6.38% for the M55-10AlN, although the AP increases slightly from 0.19% to 0.72%. The optimum densification temperature of the M55 base composition decreased from 825 °C to 800 °C for the M55-1AlN and M55-2.5AlN and then increased to 825 °C for the M55-5AlN and M55-10AlN, which may be attributed to the fact that AlN addition at low loadings lowers the glass viscosity, facilitating viscous sintering. However, retarded densification at high AlN loadings may be attributed to both lower glass content (i.e., 55 wt% in the M55 and 49.5 wt% in the M55-10AlN) and possible agglomeration of high surface area AlN nano particles in between the mullite particles, causing increased viscosity of the glass phase and hence entrapment of the closed pores. Since maximum densification was achieved for all composites below 950°C required for the LTCC systems, the composites sintered at optimum densification temperatures were used for further property characterizations.

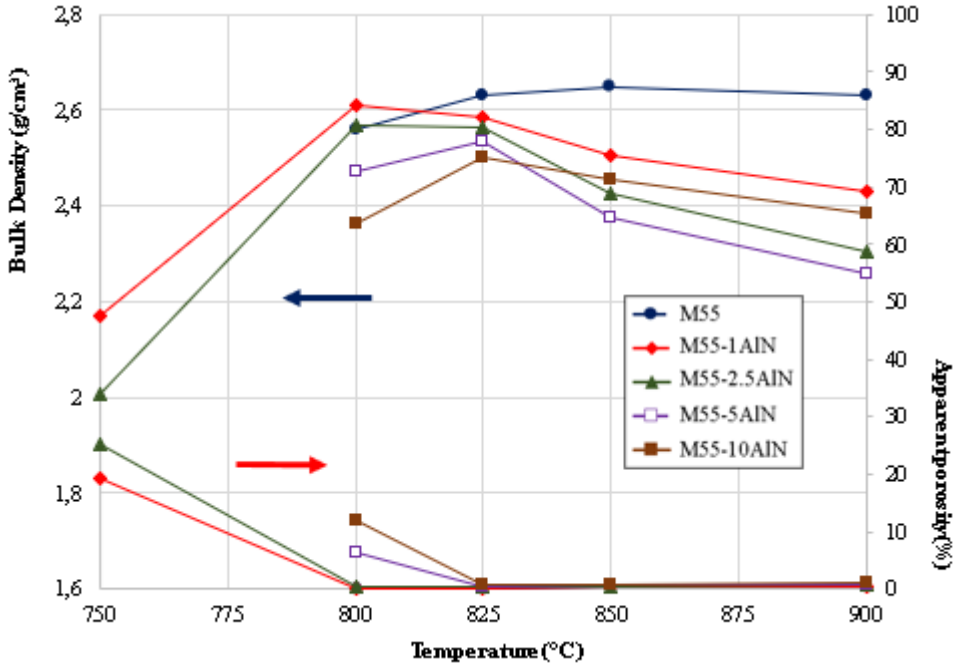

Figure 6.10 Densification of the composites as a function of AlN content and temperature.

6.2.2 Phase formation and microstructure evolution

Figure 6.11 compares XRD patterns of the composites sintered at their optimum temperatures. Mullite (Card number: 00-015-0776) was the main crystalline phase for each composition. Anorthite $(Ca,Na)(Si,Al)_4O_8$ (Card number: 00–041-1481) and AlN (Card number: 01–074-1977) phases are also marked on the patterns. The crystallization of the anorthite phase was only noticeable as it was dependent on both temperature (the anorthite phase begins to form at 825 °C) [103] and glass content [115], but the main AlN peak intensity at $2\theta = 33.36°$ increased from M55-1AlN to M55-10AlN, which indicates that AlN neither chemically reacted with other phases nor decomposed with temperature. The chemical stability of AlN is extremely important at modifying thermal, dielectric and mechanical properties.

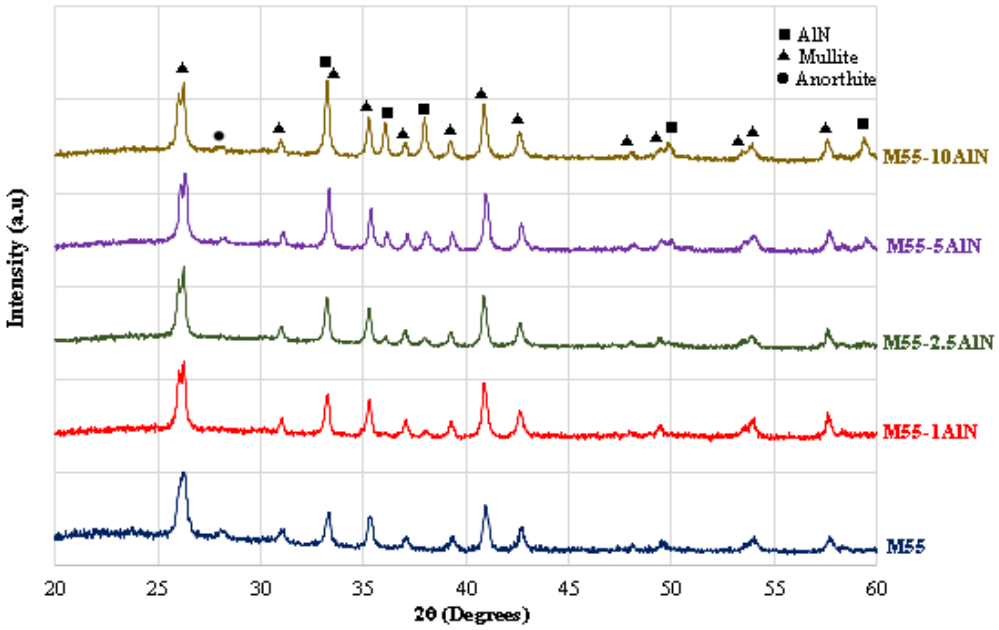

Figure 6.11 XRD patterns of the composites sintered at optimum temperatures for each composition

SEM images of the composites sintered at optimum temperatures are shown in Figure 6.12. Mullite particles (or grains) are homogeneously dispersed in the M55 base composition and the sintered microstructure is in the form of "sea-island" structure (Figure 6.12 (a)). However, the boundary between the glass matrix and mullite particles started fading away as the nano AlN content increased and filled the gaps between mullite particles (Figures 6.12 (b–e)). In addition, the closed pores became

more evident and their amounts increased with the AlN content due to the agglomeration of nano AlN particles and lower glass content, as explained for the densification behaviors. Similar results in the B_2O_3-$2SiO_2$/AlN composites [119] were observed such that the porosity increased as the amount of AlN increased due less amount of liquid phase present during sintering. Figure 6.12 (f) indicates some AlN particles, although it was very difficult to detect N by EDS method and difficulty of discriminating common Al cation in mullite, glass and AlN phases.

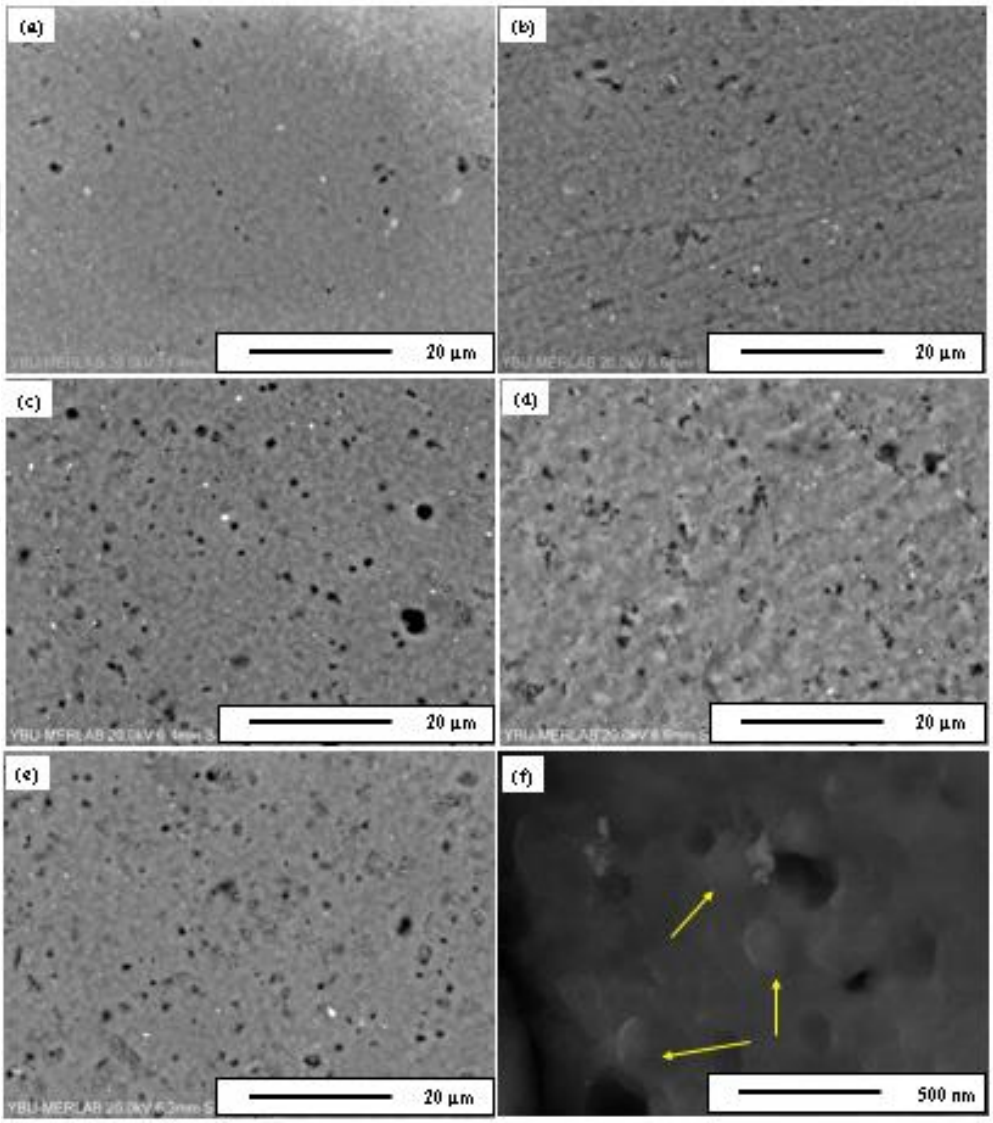

Figure 6.12 SEM images of the composites sintered at their optimum temperatures: (a) M55, (b) M55-1AlN, (c) M55-2.5AlN, (d) M55-5AlN, (e) M55-10AlN and (f) M55-10AlN at high magnification.

6.2.3 Dielectric properties

Figure 6.13 shows dielectric properties of each composition sintered at their optimum temperature as a function of AlN. The dielectric constant (K) and loss were measured at 5 MHz. The capacitance of the samples was measured and then K was calculated using Equation 2.11. Several variables such as densification (or porosity) and the presence of crystalline phases influence the dielectric characteristics. The dielectric constant (loss) at 5 MHz is 7.4 (0.0031) [102] for mullite, 6.37 (0.0016) [71] for glass and 8.6-9.2 (0.05-0.001) for AlN [82][120]). In general, the K followed a slightly decreasing tendency with increasing AlN content such that K (loss)=6.68 (0.0037) for the M55, K (loss)=6.51 (0.0026) for the M55-1AlN, K (loss)=6.54 (0.0024) for the M55-2.5AlN, K (loss)=6.46 (0.0023) for the M55-5AlN, and K (loss)=6.42 (0.0017) for the M55-10AlN. Although all samples had near-zero AP (i.e., less than 0.72%) and WA (i.e., less than 0.28%), increased amounts of closed pores with the AlN content resulted in lower K due to low K (loss) of air (e.g., 1 (0) [88]). Similar effects were reported for the glass/Al_2O_3/AlN (10 to 50 wt%) such that the K (loss) at 10 wt% AlN first decreased (~5) and then remained constant or changed little (~4.2 to 4.4) up to 40 wt% AlN [121]. Figure 6.13 also shows that the dielectric loss slightly and continuously decreased to 0.0026 at 1 wt% AlN and then to 0.0017 at 10 wt% AlN, which can be attributed to a large dielectric loss range of the AlN (0.05-0.001)[82][120] lower than that of the M55 (0.0037) and higher closed porosity (loss=0 for air [88]). In brief, porosity in the sintered ceramics has a great influence on dielectric properties. Signal propagation delay is one of the most critical parameters directly associated with K for the LTCC electronic packaging (see Equation 1.8)[40][52]. AlN addition decreases K with respect to the base M55 composition, which is strongly required for signal transmission speed.

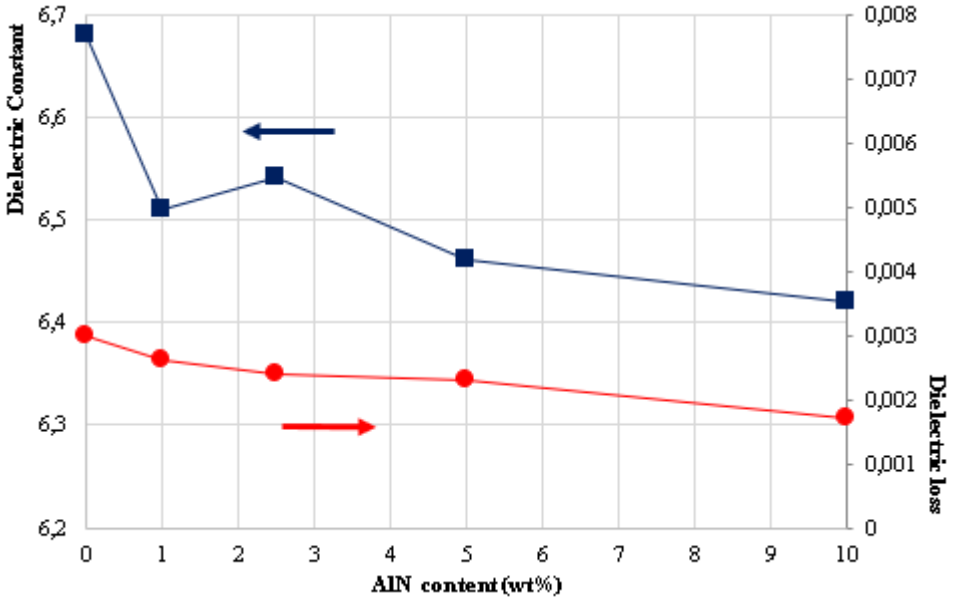

Figure 6.13 Dielectric properties of the composites sintered at optimum temperature for each composition

6.2.4 Thermal properties

A high thermal conductivity (k) is desired for more efficient and reliable LTCC packaging to dissipate heat generated during service. Heat removal has become even more critical with the growing need to manufacture high-density and high-power devices operating at high speeds [40][91]. Figure 6.14 illustrates the k and thermal expansion coefficient (CTE) of the composites sintered at optimum temperature as a function of AlN content. Straight lines are drawn to guide eye. The k values measured at 25 °C are 1.47 W/m·K for the M55, 1.55 W/m·K for the M55-1AlN, 1.63 W/m·K for the M55-2.5AlN, 1.69 W/m·K for the M55-5AlN and 1.76 W/m·K for the M55-10AlN. In other words, k increased with increasing AlN due to high k of AlN because the end compositions mullite, glass and AlN have k=6.07 W/m·K [77], k=0.85 W/m·K [38], and k=320 W/m·K [81] at 25 °C, respectively. The increase is not as high as those reported in the literature [118][122] despite a very high thermal conductivity of AlN, which can be partly attributed to the fact that the increase in the number of closed pores with increasing AlN content resulted in a limited improvement due to a very low thermal conductivity of air (0.0267 W/m·K [92]). In addition, because of the short-range order of the glass structure, phonon thermal conductivity is delayed, and

therefore the thermal conductivity of glasses often have very low k values [94]. Pores definitely puts obstacles among AlN particles which limits heat transfer paths to enhance overall k of the composites [93]. The k increased from 4.5 W/m·K (0 wt% AlN) to 5.98 W/m·K (20 wt% AlN) in the BBSZ/Al_2O_3/AlN system by means of a nanoneedle-shaped phase providing heat conduction channels. However, nano needles caused pore formation which limited thermal conductivity [121]. The k increased with increasing AlN amount from ~3.5 W/m·K for 30 wt% AlN to 5.9 W/m·K for 40 wt% AlN in the borosilicate/AlN composition [118]. In brief, AlN improves the k by forming heat conducting channels, but pores degrade the k by putting obstacles to those channels, which determines overall k of the composites.

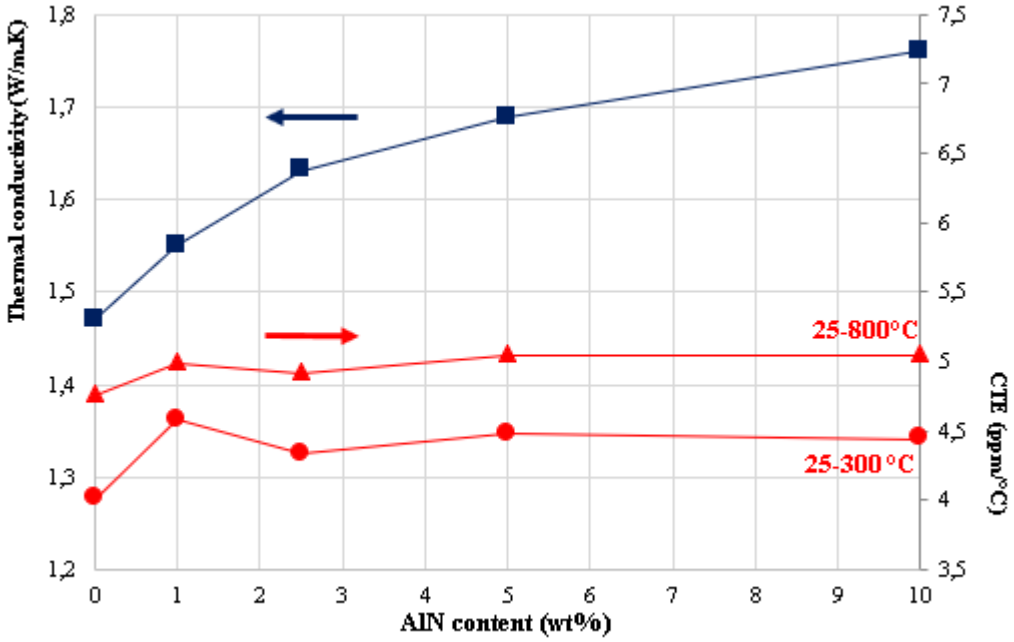

Figure 6.14 Thermal conductivity and thermal expansion coefficient of the composites sintered at optimum temperatures for each composition

The CTE match between Si chips and LTCC substrate is a critical parameter in the LTCC systems [40]. A mismatch can be a failure of melting connections between substrate and chip. Therefore, a CTE match or close to Si (~2.6–3.3 ppm /°C) is very important parameter to reach [97]. Note that the CTE values of mullite, glass, and AlN are 5.3 ppm/°C [113], 0.55 [28] and 4.5-5 ppm/°C [81], respectively. Also, low CTE's

(i.e., 0.55 ppm/°C [28] between 0 and 1000°C for vitreous silica) of silicate glasses originate from the ability to absorb vibrational energy by adjusting irregular bond angles [5]. In general, the CTE of the composites slightly increased and then remained almost constant up to 10 wt% AlN such that 4.01 ppm/°C for the M55, 4.59 ppm/°C for the M55-1AlN, 4.34 ppm/°C for the M55-2.5AlN, 4.48 ppm/°C for the M55-5AlN and 4.44 ppm/°C for the M55-10AlN at 25-300°C. The increase in CTE can be attributed to the relatively high CTE of AlN (4.5-5 ppm/°C) but closed pores distributed in the glass/mullite matrix buffer the thermal vibration. The glass transition temperatures (T_g) were determined as 650 °C for the M55 and 656 °C for the M55-1AlN, 652°C for the M55-2.5AlN, 658 °C for the M55-5AlN and 659 °C for the M55-10AlN. As explained in the preceding chapters, these Tg values are way above the test conditions of heat exposure (1000 hours at 150 °C) and temperature cycle test (from room temperature to 125 °C) [40].

6.2.5 Mechanical properties

The thin LTCC substrates have become more important due to the demand for the miniaturization of the electronic components, which necessitates optimization of the mechanical properties. The mechanical properties depend on the densification level (or relative density), presence of defects, crystalline phases, bonding type and amount of porosity[101]. Figure 6.15 shows Vickers hardness of the composites sintered at their optimum temperatures. The hardness values of the M55 and AlN are 660 HV and 1224 HV [123], respectively. In general, the hardness slightly increased with increased AlN amount and then decreased. In other words, hardness values were 660±14 HV for the M55 (RD=99.2%), 674±13.5 HV for the M55-1AlN (RD=99.0%), 637±20 HV for the M55-2.5AlN (RD=97.3%), 624±24 HV for the M55-5 AlN(RD=95.4%) and 571 ±15 HV for the M55-10AlN (RD=92.9%).

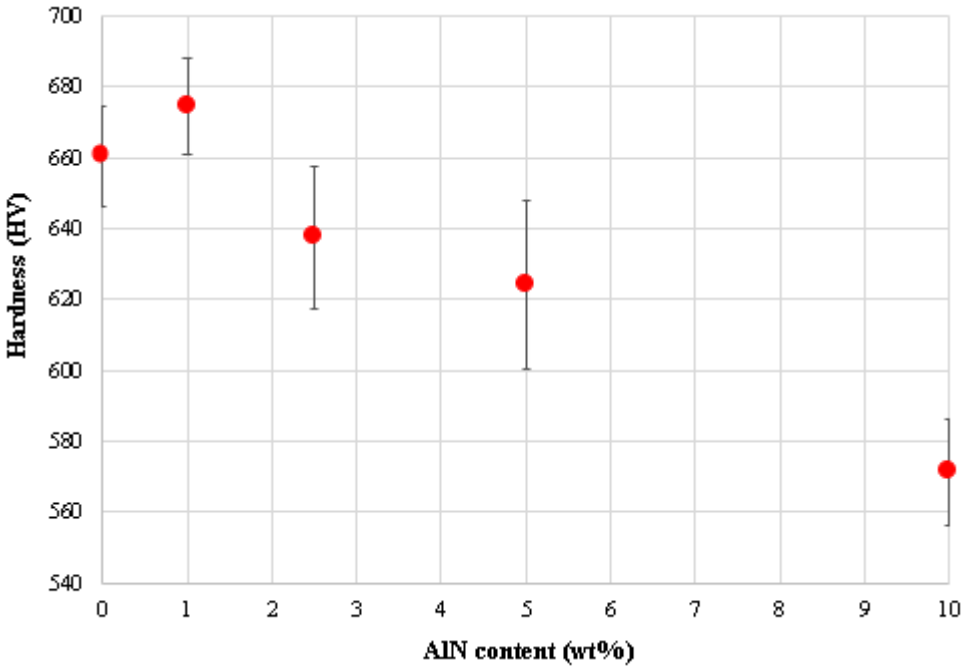

Figure 6.15 Hardness of the composites sintered at optimum temperature for each composition.

Figures 6.16 and 6.17 show the elastic modulus and flexural strength of the composites sintered at optimum temperature for each composition. The properties were determined using as-sintered samples. The flexural strength values of mullite, glass and AlN are 182 MPa [102] and 87 MPa [28], 300-350 MPa [81], respectively. The flexural strength was 92±19 MPa for the M55, 111±24 MPa for the M55-1AlN, 101±17 MPa for the M55-2.5AlN, 97±17 MPa for the M-55-5AlN and 88±11 MPa for the M55-10AlN. In other words, the flexural strength first sharply increased from 92 MPa (M55) to 111 MPa (M55-1AlN) and then continuously decreased up to 88 MPa (M55-10AlN). A similar effect on flexural strength was also reported for the $B_2O_3.2SiO_2$/AlN (30 wt% AlN to 60 wt% AlN) composites and it increased from ~48 MPa (for 30 wt% AlN) to ~60 MPa (for 40 wt% AlN) and then decreased to ~30 MPa (for the 60 wt% AlN) [119]. It was also reported for the cordierite-based glass/AlN composites and the flexural strength of composites first increased from ~115 MPa (0 wt % AlN) to ~160 MPa (20 wt% AlN) and then decreased to 80 MPa (50 wt% AlN) [124]. Similar to the flexural strength variation, the elastic modulus first slightly increased from 102±3 GPa for the M55 to 107±5 GPa for the M55-1AlN and then sharply decreased to 87±7 GPa for the M55-2.5AlN and remained almost the

same up to the M55-10AlN (82±3 GPa). The elastic modulus of mullite, glass, AlN are 185 GPa [102], 70 GPa [28], and 320 GPa [81], respectively. When the mechanical properties are evaluated as a function of AlN content, they all show a similar trend such that they first increase at 1 wt% AlN (e.g., M55-1AlN), and then start to decrease with further AlN content. In other words, dispersed AlN nano phase increases the properties due its higher mechanical properties with respect to the base M55 composition in the dense composite (e.g., RD=99%, AP=0%, WA=0%, CP=1% for the M55-1AlN) but lower densification parameters (or, increased closed porosity) with increasing AlN content become more dominant in other composites (e.g., RD=92.9%, AP=0.72%, WA=0.285%, CP=6.38% for the M55-10AlN), as explained for the densification behaviors in Figure 6.10. A similar effect (e.g., effect of porosity and nano filler) on the mechanical properties was reported in literature [125][126][127]. The overall properties of the mullite/glass/AlN composites sintered at optimum sintering temperature for each composition are summarized in Table 6.2.

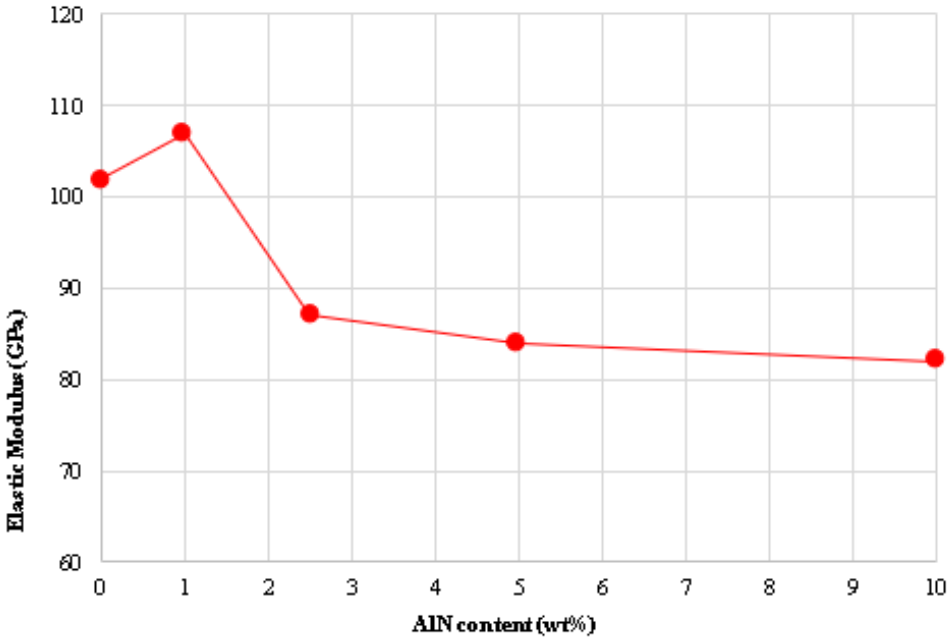

Figure 6.16 Elastic modulus of the mullite/glass/nano AlN composites sintered at optimum temperature for each composition.

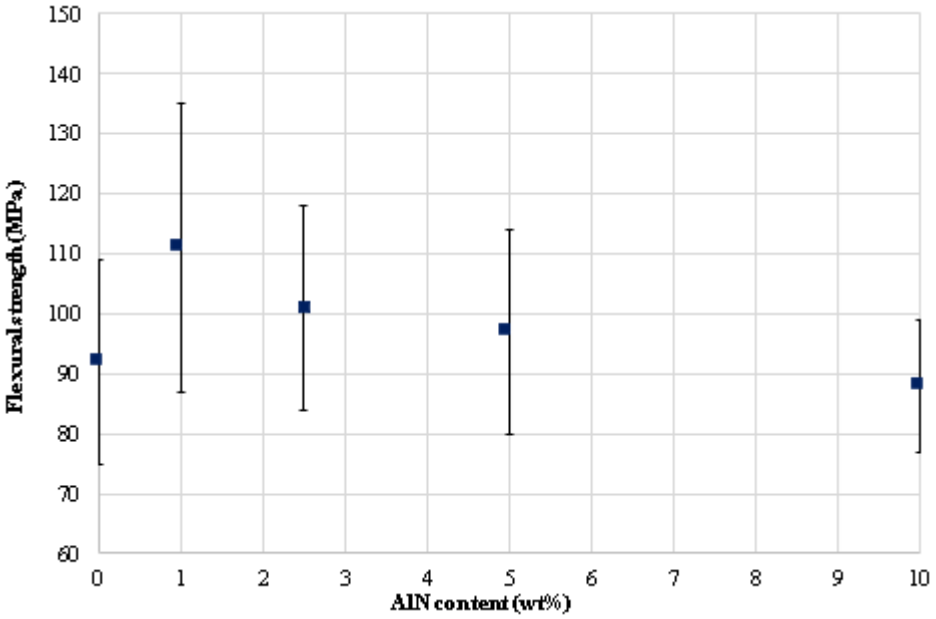

Figure 6.17 Flexural strength of the mullite/glass/nano AlN composites sintered at optimum temperature for each composition.

Table 6.2 Summary of physical properties of the composites sintered at their optimum sintering temperatures for each composition

			Dielectric Properties		Thermal Properties		Mechanical Properties		
Composition	Sintering temperature (°C)	Density (g/cm^3)	Dielectric constant	Dielectric loss	Thermal conductivity (W/m.K) (at 25°C)	Thermal Expansion Coefficient, CTE (ppm/°C) (25-300°C)	Hardness (HV)	Elastic Module (GPa)	Flexural Strength (MPa)
M55	825	2.63	6.68	0.0037	1.47	4.01	660±14	102±3	92±19
M55-1AlN	800	2.61	6.51	0.0026	1.55	4.59	674±13	107±5	111±24
M55-2.5AlN	800	2.57	6.54	0.0024	1.63	4.34	637±20	87±7	101±17
M55-5AlN	825	2.53	6.46	0.0023	1.69	4.48	624±24	84±4	97±17
M55-10AlN	800	2.48	6.42	0.0021	1.76	4.44	571±15	82±2	88±11

Mullite (45 wt%)/glass (55 wt%)/nano hBN and AlN filler (1–10 wt% AlN) composites were successfully fabricated for the LTCC applications. XRD proved that hBN and AlN neither chemically reacted with other phases nor decomposed with temperature. Dense mullite/glass (55 wt%) composite with 10 wt% hBN addition had 2.3 g/cm^3 after sintering at 900 °C, dielectric constant (loss) = 5.13 (0.003) at 5 MHz, thermal conductivity = 1.91 W/m·K at 25 °C, and thermal expansion coefficient = 4.89 ppm/°C, hardness=262±13, flexural strength=71±6 MPa and elastic modulus=70±7 GPa. However, the number of closed pores increased with the AlN content, which limited the property improvement expected. The closed pores, however, relatively improved dielectric constant (loss) from 6.68 (0.0037) at 0 wt% AlN to 6.42 (0.0017) at 10 wt% AlN. Thermal conductivity was also enhanced from 1.47 to 1.76 W/m·K in spite of the closed pores that deteriorated heat transfer paths among the AlN particles. The closed pores relatively degraded mechanical properties at high AlN contents such as hardness from HV 660±14 to 571±15, flexural strength from 92±19 to 82±11 MPa, and elastic modulus from 102±3 to 82±2 GPa. Thermal expansion coefficient varied little with the AlN content (e.g., 4.01 ppm/°C vs. 4.44 ppm/°C). These results indicate that although the mechanical properties relatively decreased with the AlN addition, the mullite/glass/AlN (10 wt%) composite densified at 825°C (bulk density = 2.48 g/cm^3 and AP = 0.72%) had improved dielectric and thermal properties that are comparable to the commercial LTCC products.

CHAPTER 7

PROTOTYPE FABRICATION FOR THE LTCC AND RADOME APPLICATIONS

7.1 Radome

In general, common requirements for the radomes are dielectric constant and loss as low as possible and thermal conductivity as high as possible. In addition, a high melting or glass transition temperature as well as high thermal shock resistance parameter (e.g., high flexural strength and thermal conductivity, low elastic constant and thermal expansion coefficient) are required. The composites with 10-30 wt% glass (i.e., M10-M30) were all suitable candidates for the radome applications (see Table 5.1). The M20 composition was particularly chosen due to its high sintering temperature of 1450°C and highest thermal shock resistance parameter of 162°C together with other appropriate physical properties such as dielectric constant (loss)=7.12 (0.0025) at 5 MHz (and dielectric constant=5.9 at 4–10 GHz), thermal conductivity=3.72 W/m·K, thermal expansion coefficient=4.27 ppm/°C, flexural strength=180±21 MPa, elastic modulus=189±6 GPa. Ecebaş et al. [102] produced mullite by gel casting method for the radome application and reported that flexural strength=182 MPa, elastic module=185 GPa, dielectric constant (loss)=7.4 (0.0031), thermal expansion coefficient=5.26 ppm/ºC, thermal conductivity=3.75 W/m·K and thermal shock resistance parameter=142 ºC. The M20 composite has distinct advantages to mullite such as lower density, dielectric properties, and particularly higher thermal shock resistance parameter that strongly relates with thermo-mechanical properties (see Equation 1.4). Table 7.1 lists some characteristics of the commercial glass-ceramic MACOR, mullite and M20. MACOR offers working temperatures up to 1000 °C but has a glass transition temperature of roughly 475 °C [65][66]. The M20 composite's glass transition temperature is 709 °C, which states a stable high temperature performance. In addition, mechanical properties and thermal conductivity are much higher, which states that the M20 composition is a suitable

candidate for the radome applications and has prominent properties with respect to the commercial products.

Table 7.1 Some properties of commercial glass/ceramic MACOR[66], mullite[102] and M20 (this study)

Materials	MACOR	Mullite	M20
Density (g/cm^3)	2.52	3.13	2.99
Dielectric constant	6.01 at 1 KHz	7.4 at 5 MHz	7.12 at 5 MHz
Dielectric loss	0.0040 at 1 KHz	0.0031 at 5 MHz	0.0025 at 5 MHz
CTE (ppm/ºC)	11.2 (25-600 ºC)	5.26 (25-800 ºC)	4.27(25-800 ºC)
Thermal conductivity(W/m·K)	1.46	2 (100 ºC) - 3.75 (550 ºC)	3.72 (25 ºC)
Flexural strength (MPa)	94	182	151
Elastic modulus (GPa)	66.9	185	165
Continuous operating temperature (ºC)	800 T_g=475	T_g=~500	T_g=709
Maximum no load temperature (ºC)	1000	-	-
Thermal shock resistance (R, R´)	80 (°C), 116 .8 (kW/m)	142 (°C), 532.5 (kW/m)	162 (°C), 607.58 (kW/m)

Weibull modulus and fracture strength are typically used to assess a ceramic's suitability for structural applications. Weibull modulus is influenced by surface finishing characteristics, microstructure, and inclusion type [128]. The statistical Weibull analysis of the flexural strength is displayed in Figure 7.1. Note that as-sintered ceramics were used to measure the flexural strength, which may alter or widen the measured strength data. The Weibull modulus (m) was determined from a linear fit to the data points with an R^2=0.9685 and calculated as 4.70. For ceramics, a typical Weibull modulus is between 3 and 15. A greater m indicates a more trustworthy material with less fracture strength spreading [128]. The linear equation's constant variable (c) was 24.54. Using Equation 2.9, a characteristic strength was determined to be 185 MPa, below which no failure is expected. Ecebaş et al. [102] reported for mullite that m=12.33 (R^2=0.983), c=64.44 and characteristic strength=186 MPa. Although the characteristic strengths are the same despite the fact that liquid phase formers (i.e., 3.4 wt% TiO_2 [102] vs. 10 wt% glass) are different in both mullite compositions, the m values are quite different. This distinct difference can be attributed to the surface conditions of the ceramics during 3-point bending test because Ecebaş et al. [102] ground the surfaces and edge corners of the samples before sintering that might eliminate possible defects causing low flexural strengths. Characteristic

strength=186 MPa and m=4.7 are very promising for the M20 ceramics with as-sintered surfaces. Fu et al. [129] reported a Weibull modulus between 4 and 14 for the Al_2O_3 ceramics prepared by dry pressing at varied pressures and cold isostatic pressing. A very wide modulus range was explained based on the processing factors such as grain size, homogenous microstructure, and green density. The compressive strength of MACOR varied depending on the surface condition such that it was 345 MPa for the as-machined surface and 900 MPa for the polished surface [66].

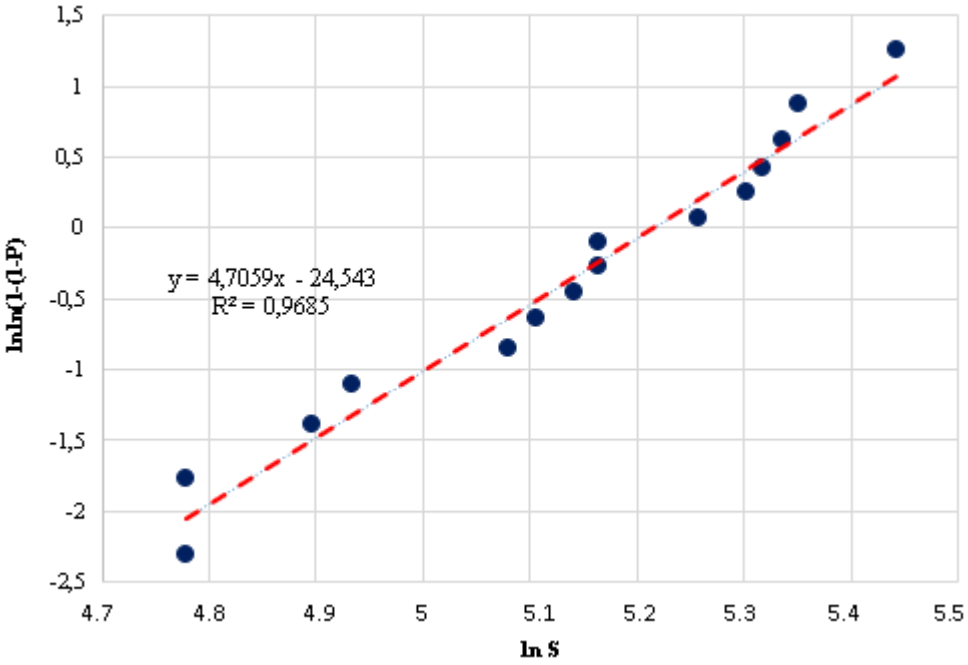

Figure 7.1 Weibull approach for statistical analysis of the flexural strength

Material properties as a function of temperature are critical to evaluate the real time conditions, but most of the time room temperature properties are reported. Figure 7.2 shows the temperature-dependent dielectric properties of the M20 sample. Dielectric properties remained almost unchanged up to nearly 300ºC, but then started increasing sharply. The dielectric constant (loss) changed by 38% (145%) from at 25 ºC to 500ºC. Pyroceramic [130] exhibited similar variation in dielectric constant (by 36.6 % between 25 and 1000ºC. The variation in dielectric loss was ~233%. The variation in the dielectric constant (loss) of Al_20_3 was 19.79% (250%) at 25-1000 ºC [63]. A minimum change in dielectric properties is desired for the radome material from the

thickness design point of view. In addition, the dielectric constant and loss affect the signal propagation and transformation of signal to heat [131].

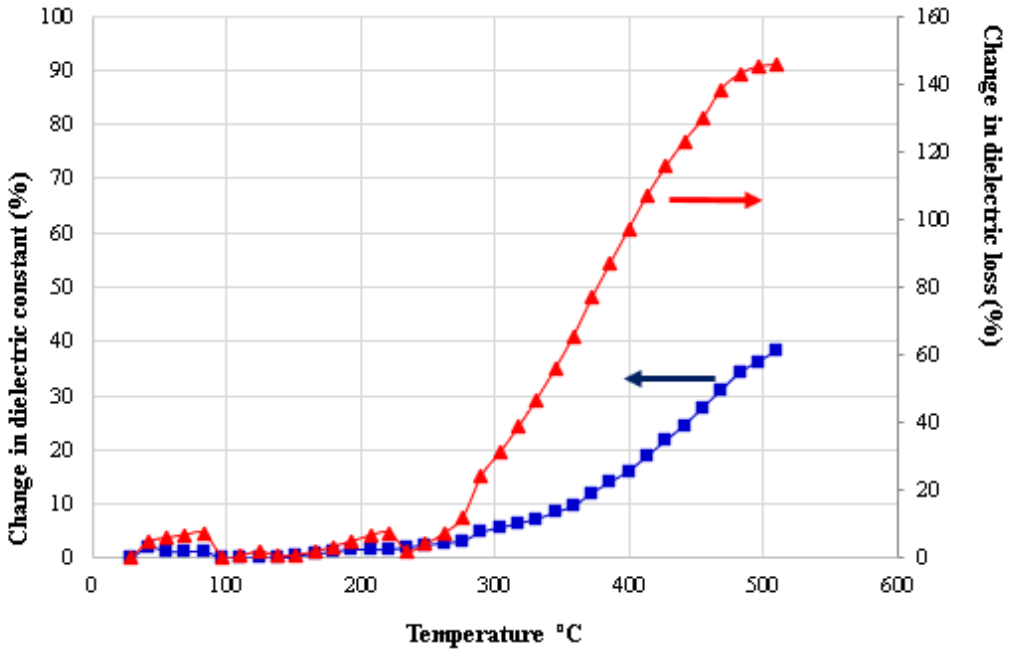

Figure 7.2 Dielectric properties depending on the temperature of M20 sample.

Radomes have curved surfaces in order to conform to the shape of the platform it is integrated. In addition, they are large and 3D products. Therefore, ceramic forming techniques which allows near-net shaping and/or green machining are chosen. Therefore, gel casting method which offers both advantages was used to manufacture a prototype ceramic. Figure 7.3 shows the stages during a prototype fabrication by gel casting method. Slurry gelation was completed in several minutes due to catalyzer TEMED addition. After curing in air at room temperature, green ceramics were dried in an oven to remove water completely without fracturing the ceramic blocks. They were easily green machined in a desired form by using a CNC machine. The machined ceramic blocks were sintered at 1450 ºC for 1h in between flat Al_2O_3 ceramic blocks, following the polymer burn out step. The ceramics were successfully sintered without any visible deformation and machined details were all retained. These results indicate that gel casting is a viable method to manufacture large and 3D ceramics at various dimensions.

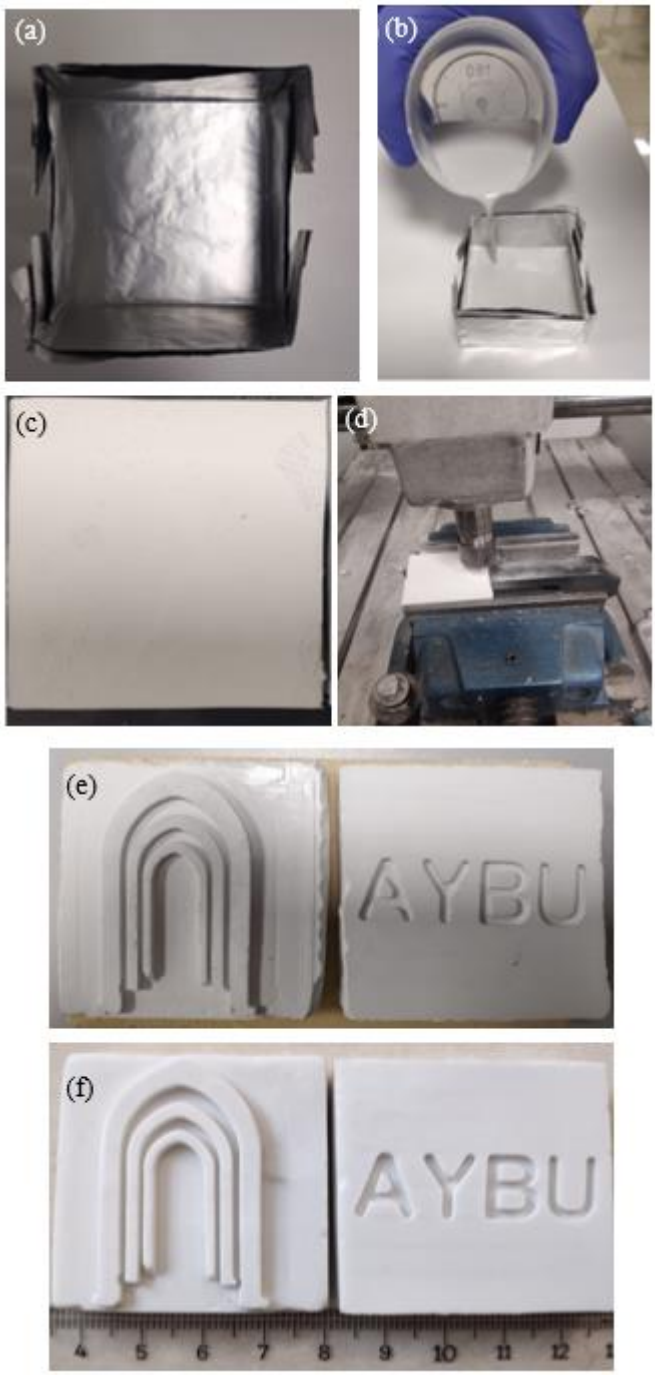

Figure 7.3 Stages of prototype gel casting process; a) aluminum mold, b) gel casting of a slurry, (c) cured and dried green ceramic, (d) green machining by a CNC machine, (e) green-machined ceramics and (f) sintered ceramics

7.2 Low Temperature Co-Fired Ceramic

In general, LTCC systems require some optimized physical properties such as mechanical properties (flexural strength = 116–320 MPa, elastic modulus = 80–150 GPa), dielectric properties (dielectric constant, K = 3.8–9.2, loss = 0.0007–0.006 at 1 MHz) and thermal properties (thermal conductivity, k = 2.0–4.5 W/m·K, thermal expansion coefficient, CTE = 4.5–7.5 ppm/°C), low-temperature densification < 950 °C to be compatible with electrode material (e.g., silver that melts at 961 °C) [53][54][55][56]. Therefore, the M55-10hBN composition was selected for a LTCC prototype production due particularly to low dielectric properties, low thermal expansion coefficient and high thermal conductivity. It has a bulk density=2.3 g/cm^3 after sintering at 900 °C, dielectric constant (loss) = 5.13 (0.003) at 5 MHz, thermal conductivity = 1.91 W/m·K at 25 °C, thermal expansion coefficient= 4.89 ppm/°C, flexural strength=71 MPa and elastic modulus= 71 GPa. Tape casting method was used to prepare LTCC prototype. A pseudoplastic behavior is desired for tape casting slurry [132] but viscosity-shear rate graph given in Figure 7.4 indicates that it was not an ideal pseudoplasticity although viscosity decreased with the shear rate. Since the slurry contained a high amount of binder solution (i.e., 60 wt% solution) and the solution contains 75 wt% solvent (methyl ethyl ketone + ethyl alcohol), the rapid evaporation of the solvent during measurement solidified the slurry and made the viscosity measurement very difficult. Figure 7.5 shows the stages during a prototype LTCC fabrication by tape casting method. The same procedures were applied for tape casting as explained in Chapter 2. Dried thickness of the tapes was about 80 μm. A brush was used for Ag application on the green layers. The green tapes with/out electrodes were hot-laminated at 80 °C applying 20 MPa for 10 min for each side. The green tapes were stacked in such a way to locate 4 or 6 blank interlayers between each electroded layer. Figure 7.6 shows the cross-section of the ceramic sintered at 900 °C with an optical microscope. Aligned Ag electrodes are readily observed. LTCC samples were successfully fabricated without delamination or warping in the final products. The XRD pattern taken from the Ag applied surface is shown in Figure 7.7. It is clear that Ag (Card number: 01-087-0720) did not react with other phases (mullite, anorthite, hBN).

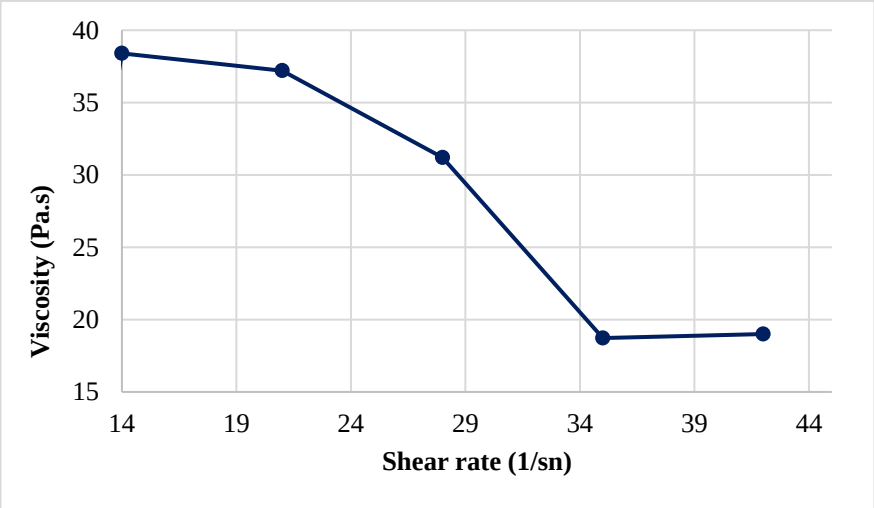

Figure 7.4 Viscosity as a function of shear rate

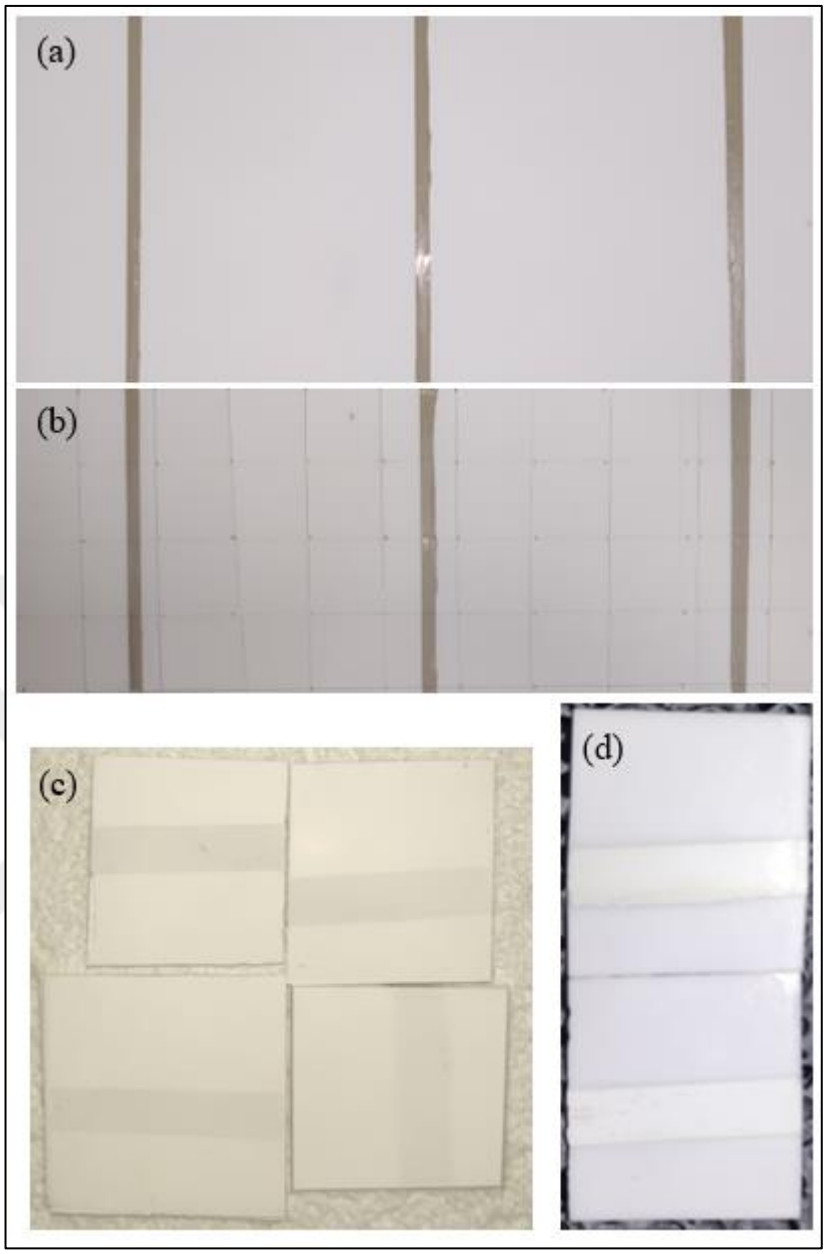

Figure 7.5 Processing of the LTCC prototype; (a) green tapes with Ag electrodes, (b) green tapes cut in desired dimensions, (c) laminated green tapes and (d) sintered ceramics.

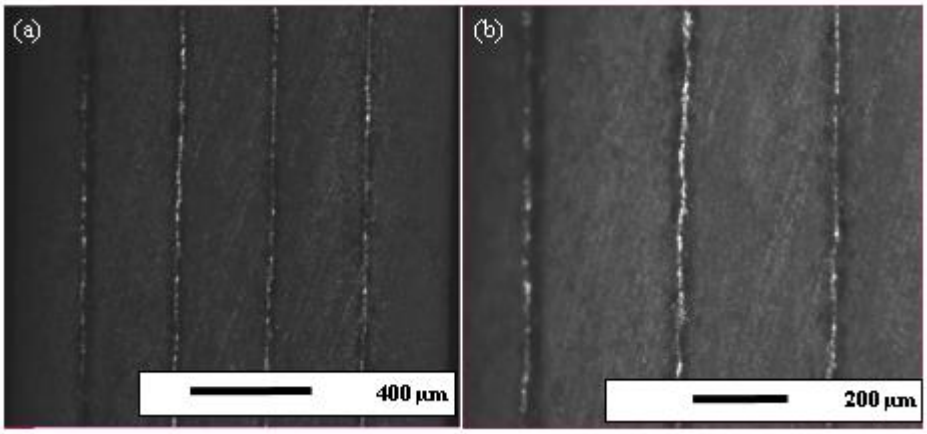

Figure 7.6 Micrograph of the sintered samples; (a) 4 blank interlayers between each electrode; (b) 6 blank interlayers between each electrode layer

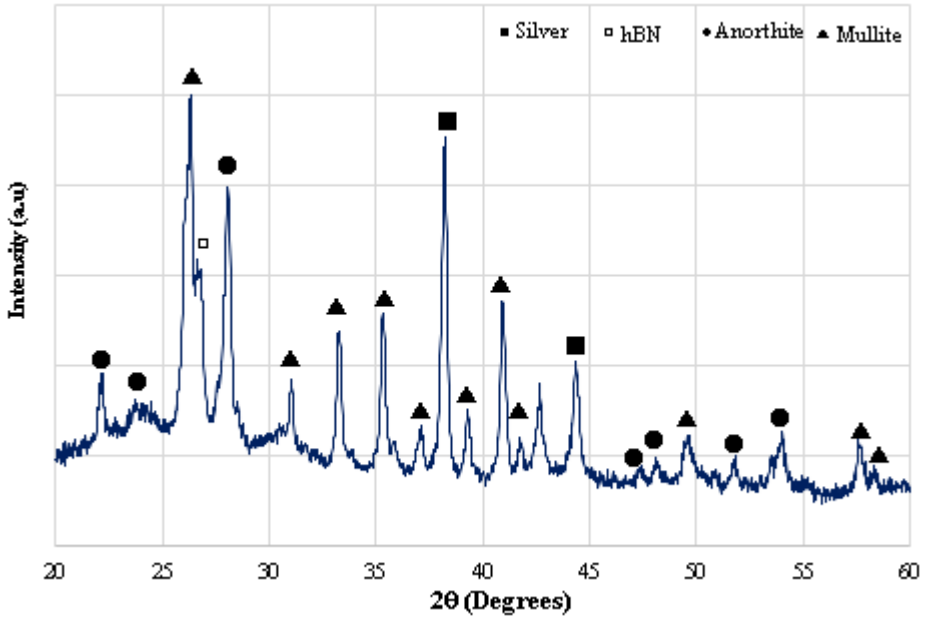

Figure 7.7 XRD pattern of the ceramic surface with silver

Figure 7.8 shows the temperature-dependent dielectric properties of the M55-10 hBN sample. The dielectric constant (loss) changed by 2.46% (0.92%) from at 25 ºC to 150 ºC. A number of thermal tests are applied to the LTCC circuits such as heat exposure test (i.e., 1000 hours at 150 °C), temperature cycle test (i.e., from room temperature to 125 °C)[40]. In this regard, temperature-dependent changes in the dielectric properties up to 150 °C are very small, which ensures a reliable service condition.

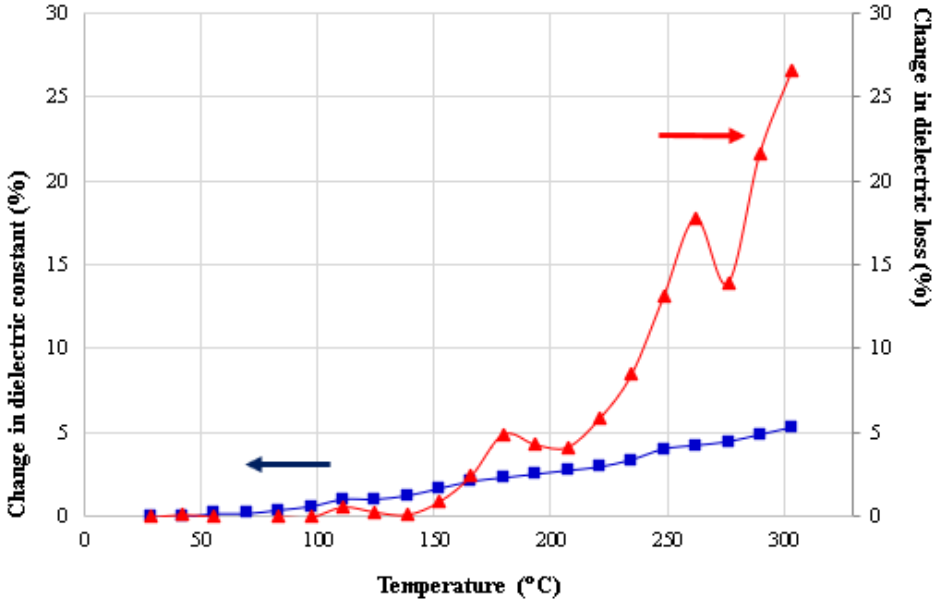

Figure 7.8 Dielectric properties as a function of temperature at 5 MHz

CHAPTER 8

CONCLUSIONS

It was aimed to optimize mechanical, thermal and dielectric properties of (SiO_2-Al_2O_3-CaO based) glass/(mullite or Al_2O_3) ceramic/(and nanofiller (hBN, AlN)) composites for functional (e.g., low temperature co-fired ceramic-LTCC) and structural (e.g., radome) applications. As common requirements for both applications, dielectric constant and loss must be as low as possible, and thermal conductivity must be as high as possible, together with moderate mechanical properties to support the structure. However, densification temperature less than 950 °C is a must for the LTCC systems to apply silver electrode, a high melting or glass transition temperature as well as high thermal shock resistance parameter (e.g., high flexural strength and thermal conductivity, low elastic constant and thermal expansion coefficient) are required for the radomes. Therefore, compositional engineering concept was applied to optimize those requirements by varying glass content to adjust densification temperature by means of liquid phase or viscous sintering and nano filler contents to adjust mainly thermal and dielectric properties. Al_2O_3 and mullite ($3Al_2O_3.2SiO_2$) were chosen as the main skeleton crystalline phases to support the whole composite structure.

A base Al_2O_3/55 wt% glass composition was first selected and then the effect of (1-10 wt%) hBN was initially investigated. Although apparent porosity was less than 1% in all composites, closed porosity increased with increasing hBN content such as 1.23% (with RD=98.64%) at 0 wt% hBN and 12.49% (with RD=87.19%) at 10 wt% hBN. Porosity affected physical properties in different ways. It decreased (or, alternatively, enhanced) dielectric constant from 7.3 for the 0 wt% hBN to 5.57 for the 10 wt% hBN at 5 MHz. Although hBN addition strongly improved mean thermal conductivity from 1.93 W/m·K at 0 wt% hBN to 2.71 W/m·K at 10 wt% hBN at 25 °C, the improvement was not as high as expected and remained limited due to the closed porosities. The mechanical properties were lowered but high enough for the LTCC applications (i.e., flexural strength=82 MPa and elastic modulus=83 GPa at 10 wt% hBN). Furthermore, an hBN content greater than 10 wt% was not applied due to both a higher polymer

ratio required for tape casting and densification temperature exceeding 950 ºC causing hBN oxidation.

Al_2O_3 was then replaced with mullite to further optimize the properties. First, densification, phase formation and physical (dielectric, thermal, mechanical) properties were thoroughly studied for the base mullite/glass (10-60 wt%) composites. The optimum densification temperatures decreased from 1550°C (for the 10 wt% glass) to 1400°C (for the 30 wt% glass) due to liquid phase sintering, to 850°C (for the 50 wt% glass) and 825°C (for the 55 and 60 wt% glass) due to viscous sintering. In-situ anorthite crystallization took place in the samples with the 50 to 60 wt% glass after 825°C. Although the dielectric constant (loss) was enhanced from 7.29 (0.0028) for the 10 wt% glass and 6.71 (0.0021) for the 60 wt% glass at 5 MHz, thermal conductivity decreased from 4.45 W/m·K for the 10 wt% glass to 1.55 W/m·K for the 60 wt% glass due to low conductivity of the glass matrix. Glass addition also lowered, as expected, the mechanical properties from the 10 wt% glass to 60 wt% glass such as hardness from HV 1140 to 642, flexural strength from 180 MPa and 89 MPa, and elastic modulus from 189 GPa to 98 GPa.

The mullite/55 wt% glass composition was selected to further engineer the properties for the LTCC applications because it was densified at 825 °C and had a dielectric constant (loss) of 6.68 (0.0037) at 5 MHz as well as a thermal conductivity of 1.47 W/m·K at 25ºC. Therefore, plate-shaped hBN and spherical AlN powders as nano fillers (1-10 wt%) were added to the base mullite/55 wt% glass to particularly improve thermal properties without increasing densification temperature above 950 °C and degrading other properties. XRD proved that hBN and AlN neither chemically reacted with other phases nor decomposed with temperature, which was critical for the property improvements. The composite with 10 wt% hBN had a dielectric constant (loss) of 5.13 (0.003) at 5 MHz and a thermal conductivity of 1.91 W/m·K at 25 °C. However, increased numbers of closed pores with the AlN content limited the property improvement expected. The composite with 10 wt% AlN had a dielectric constant (loss) of 6.42 (0.0017) and a thermal conductivity of 1.76 W/m·K at 25 °C.

The overall results were evaluated together to comply with some potential structural and functional applications. The mullite/20 wt% glass composition was chosen for the

radome applications particularly due to its high sintering temperature of 1450 °C (bulk density=2.86 g/cm^3, RD=99.3 %, AP=0%, Tg=709 °C) and highest thermal shock resistance parameter of 162°C together with other physical properties such as dielectric constant (loss)=7.12 (0.0025) at 5 MHz (and dielectric constant=5.9 at 4–10 GHz), thermal conductivity=3.72 W/m·K, thermal expansion coefficient=4.27 ppm/°C (25-800 °C), flexural strength=180 MPa, elastic modulus=189 GPa. The mullite/55 wt% glass/10 wt% hBN composition was selected for the LTCC applications particularly due to low dielectric properties, low thermal expansion coefficient and high thermal conductivity such that it has a bulk density=2.3 g/cm^3 (RD=89.14%, AP=0.46%, CP=10.40%) after sintering at 900 °C, dielectric constant (loss) = 5.13 (0.003) at 5 MHz, thermal conductivity = 1.91 W/m·K at 25 °C, thermal expansion coefficient= 4.89 ppm/°C (25-800 °C), flexural strength=71 MPa and elastic modulus=71 GPa. These results are comparable with respect to the commercial products.

Finally, a prototype LTCC was fabricated by tape casting method that allows formation of thin and large-area layers on which electronic components and electrodes are applied. Laminated green samples with inner silver strip electrodes were successfully co-fired and densified. In addition, a prototype radome was fabricated by gel casting method that allows formation of near-net shape 3D products or green machinable bulk samples. The bulk ceramics were first green machined and then successfully densified without any shape distortion.

REFERENCES

[1] Ş. Yılmaz, Volkanik Bazalt Kayaçlarından Cam-seramik Malzeme Üretim Koşullarının Araştırılması ve Özelliklerinin İncelenmesi, İstanbul Teknik Üniversitesi, Fen Bilimleri Enstitüsü, n.d.

[2] ASTM C162-05(2015) Standard Terminology of Glass and Glass Products, (n.d.). https://www.astm.org/c0162-05r15.html.

[3] H. Rawson, Properties and applications of glass, Elsevier Sci. Technol. 3 (1980).

[4] P.W. McMillian, Glass-Ceramics, 2nd ed., LONDON, 1979.

[5] W.D. Kingery, Introduction to Ceramics, J. Electrochem. Soc. 124 (1997) 152C.

[6] L.J. Golonka, Technology and applications of Low Temperature Cofired Ceramic (LTCC) based sensors and microsystems, Bull. Polish Acad. Sci. Tech. Sci. 54 (2006) 221–231.

[7] D.R.U. W. D. Kingery, H. K. Bowen, Introduction to Ceramics, in: New York, 1975: pp. 47–50.

[8] W. H. Zachariasen, The atomic arrangement in glass, J. Am. Chem. Soc. 54 (1932) 3841–3851.

[9] D.R. Uhlmann, Crystallization and glass formation, J. Non. Cryst. Solids. 73 (1985) 585–592. https://doi.org/10.1016/0022-3093(85)90377-1.

[10] D.R. UHLMANN, Glass Formation, a Contemporary View, J. Am. Ceram. Soc. 66 (1983) 95–100. https://doi.org/10.1111/j.1151-2916.1983.tb09982.x.

[11] M. Erol, Glass, Glass Ceramic and Sintered Materials Produced From Industrial Wastes, İstanbul Teknik Üniversitesi, Fen Bilimleri Enstitüsü, 2006.

[12] W. Callister, Materials science and engineering: An introduction, 2007.

[13] I.J. McColm, Refractory oxide ceramics. Ceramic Science for Materials Technologists, Chapman an, New York, 1983.

[14] R. Casasola, J.M. Rincón, M. Romero, Glass-ceramic glazes for ceramic tiles: A review, J. Mater. Sci. 47 (2012) 553–582. https://doi.org/10.1007/s10853-011-5981-y.

[15] R.D. Rawlings, J.P. Wu, A.R. Boccaccini, Glass-ceramics: Their production from wastes-A Review, J. Mater. Sci. 41 (2006) 733–761. https://doi.org/10.1007/s10853-006-6554-3.

[16] M.T. Sebastian, H. Jantunen, Low loss dielectric materials for LTCC applications: A review, Int. Mater. Rev. 53 (2008) 57–90. https://doi.org/10.1179/174328008X277524.

[17] R.F. WALKER, Mechanism of Material Transport During Sintering, J. Am. Ceram. Soc. 38 (1955) 187–197. https://doi.org/10.1111/j.1151-2916.1955.tb14928.x.

[18] R.M. German, History of sintering: Empirical phase, Powder Metall. 56 (2013) 117–123. https://doi.org/10.1179/1743290112Y.0000000025.

[19] R. Cartwright, Book Reviews: Book Reviews, Perspect. Public Health. 130 (2010) 239–239. https://doi.org/10.1177/1757913910379198.

[20] Z. Zak Fang, Sintering of Advanced Materials, Woodhead P, 2010.

[21] German RM., "Powder Metallurgy Science Princeton, NJ, Metal Powder Industries Federation., Princeton, NJ, 1984.

[22] M. N. Rahaman, Ceramic Prpcessing and Sintering, second edi, New York, 2003.

[23] S.J.L. (2004). Kang, Sintering: densification, grain growth and microstructure., Elsevier, 2004.

[24] B. Francois, R-r, (1967) 449–450. The Sintering of Crystalline Oxides, I. Interactions Between Grain Boundaries and Pores

[25] V.Z. Shirinian, D. V Lonshakov, S. Nichols, Additive manufacturing of metal components – process-material interaction in different process chains Additive manufacturing of metal components – process- material interaction in different

process chains ., (2019). https://doi.org/10.1088/1757-899X/580/1/012006.

[26] R.M. German, P. Suri, S.J. Park, Review: Liquid phase sintering, J. Mater. Sci. 44 (2009) 1–39. https://doi.org/10.1007/s10853-008-3008-0.

[27] O.H. Mahi, F. T. Kwon, Liquid Phase Sintering: Ceramics, Reference Module in Materials Science and Materials Engineering, 2016.

[28] W.D. . Kingery, Introduction to Ceramics, 1977.

[29] D. J. Green, An Introduction to the Mechanical Properties of Ceramics, 1 st, Cambridge University Press, 1998.

[30] H. Belghalem, M. Hamidouche, L. Gremillard, G. Bonnefont, G. Fantozzi, Thermal shock resistance of two micro-structured alumina obtained by natural sintering and SPS, Ceram. Int. 40 (2014) 619–627. https://doi.org/10.1016/j.ceramint.2013.06.045.

[31] https://www.tf.uni-kiel.de/matwis/amat/elmat_en/kap_3/backbone/r3_2_4.html.

[32] Dielectric Polarization, (n.d.). https://eng.libretexts.org/Bookshelves/Materials_Science/Supplemental_Modules_(Materials_Science)/Optical_Properties/Dielectric_Polarization.

[33] Dielectric constant, (n.d.). %250ADielectric properties for the composites as a function of a Anorthite/Al2O3 ratio for the glass/Al2O3/hBN and b Anorthite/mullite ratio for the glass/mullite/hBN composites (Arrows indicate the optimum densification temperatures)%250A%250AFull size image%250.

[34] Dielectric materials, https://www.brainkart.com/article/Dielectric-Materials_6827/ (accessed Jan. 06, 2023).

[35] Dielectric Strength | Constant | Loss | Definition - Your Electrical Guide, (n.d.). Dielectric Strength %7C Constant %7C Loss %7C Definition - Your Electrical Guide (accessed June 12, 2023).

[36] D.R.G. G.H. Poirier, Transport Phenomena in Materials Processing, Springer Nature, Switzerland, 2016.

[37] J. F. Shackelford and R. H. Doremus, Ceramic and glass materials: Structure, properties and processing, 2008.

[38] Lide DR., CRC handbook of chemistry and physics, 2003.

[39] Y. Fei, Thermal expansion," Rock Phys. Phase Relations, in: 1995: pp. 29–44.

[40] Yoshihiko Imanaka, Multilayered Low Temperature Cofired Ceramics (LTCC) Technology, JAPAN, 2005.

[41] H. Liang, H.L. Barnes, J. Laskar, D. Estreich, Application of digital PGA technology to k-band microcircuit and microwave subsystem packages, IEEE Trans. Microw. Theory Tech. 48 (2000) 2644–2651. https://doi.org/10.1109/22.899025.

[42] T.A. Midford, J.J. Wooldridge, R.L. Sturdivant, The Evolution of Packages for Monolithic Microwave and Millimeter-Wave Circuits, IEEE Trans. Antennas Propag. 43 (1995) 983–991. https://doi.org/10.1109/8.410215.

[43] R.R. TUMMALA, ChemInform Abstract: Ceramic and Glass-Ceramic Packaging in the 1990s, ChemInform. 22 (2010) no-no. https://doi.org/10.1002/chin.199132314.

[44] H.T.S. A. L. Eustice, S. J. Horowitz, J. J. Stewart, A. R. Travis, Low temperature cofireable ceramics. A new approach for Electronic packaging, 36th Electron. Compon. Conf. (1986) 37–47.

[45] K.H.D. J. Muller, H. Thust, RF design considerations for passive elements in LTCC material systems ., Int. J. Microcircuits Electron. Packag. 18 (1995) 200–206.

[46] K.W. Leung, K.M. Luk, and Extends a Length of, (1995) 517–519.

[47] H. Jantunen, a Novel Low Temperature Co-Firing Ceramic (Ltcc) Material for Telecommunication Devices, (2001).

[48] S.F. Wang, J.P. Dougherty, W. Huebner, J.G. Pepin, Silver-Palladium Thick-Film Conductors, J. Am. Ceram. Soc. 77 (1994) 3051–3072. https://doi.org/10.1111/j.1151-2916.1994.tb04549.x.

[49] S.D.E. Microtechnique, Fabrication of Low Temperature Co-Fired Ceramic (Ltcc)-Based Sensor and Micro-Fluidic Structures, Techniques. 3696 (2007).

[50] J. Zhou, Towards rational design of low-temperature co-fired ceramic (LTCC) materials, J. Adv. Ceram. 1 (2012) 89–99. https://doi.org/10.1007/s40145-012-0011-3.

[51] Chowdhry U. Sleight AW, Ceramic substrates for microelectronic packaging, Annu Rev Mater Sci. 17(1) (1987) 323–340.

[52] M.K. Mattox DM, Gurkovich SR, Olenick A, Low Dielectric Constant, alumina-compatible, Co-Fired multilayer substrate, Ceram. Eng. Sci. 9 (1988) 1567–1578.

[53] Kyocera, LTCC Data Sheet, (n.d.). https://global.kyocera.com/prdct/semicon/material/ (accessed August 30, 2021).

[54] Murata commercial LTCC data sheet (online), (n.d.). https://www.murata.com/en-global/products/filter/lcfilter.

[55] Ferro, LTCC Data Sheet, (n.d.). https://www.etsmtl.ca/Unites-de-recherche%0A/LTCC/Services-offerts/Ferro_A6M.pdf (accessed August 30, 2021).

[56] Heraeus, Commercial LTCC Data Sheet, (n.d.). https://www.heraeus.com/%0Amedia/media/het/doc_het/products_and_solu%0Ations_het_documents/thick_film/thick_film_data_%0Asheets/passive_components/ltcc/LTCC_Materials_%0AX200.pdf (accessed August 30, 2021).

[57] . https://www.hk.koaglobal.com/sitecore/content/KOA_Global/japan/Home/product/category/ltcc/basic (accessed January 26, 2020).

[58] Corning, (n.d.). https://www.corning.com/worldwide/en/products/advanced-optics/product-materials/aerospace-defense/missile-domes-radomes.html%0A.

[59] D. G. Burks, Radomes in Antenna Engineering Handbook, 2007.

[60] G.S. Mani, Microwave Materials, Berlin, Heidelberg, 1994.

[61] G.A.E. Crone, A.W. Rudge, G.N. Taylor, Design and performance of airborne radomes: A review, IEE Proc. F Commun. Radar Signal Process. 128 (1981) 451–464. https://doi.org/10.1049/ip-f-1.1981.0077.

[62] D. (Navsea) Putnam, Advanced Tactical Missile Radomes, (n.d.). https://www.navysbir.com/n13_1/N131-056.htm. (accessed January 26, 2020).

[63] R.H. Cary, Avionic Radome Materials, paris, 1974.

[64] I. Kagomiya, Y. Kodama, Y. Shimizu, K.I. Kakimoto, H. Ohsato, Y. Miyauchi, Low-temperature sintering and microwave dielectric properties of Al2TeO6-TeO2 ceramics, J. Alloys Compd. 640 (2015) 383–387. https://doi.org/10.1016/j.jallcom.2015.03.245.

[65] MACOR-The Genuie Machinable Glass Ceramic, (n.d.). https://www.corning.com/worldwide/en/products/advanced-optics/product-materials/specialty-glass-and-glass-ceramics/glass-ceramics/macor.html (accessed January 26, 2020).

[66] MACOR, Machinable Glass Ceramic For Industrial Applications, (n.d.). https://www.corning.com/media/worldwide/csm/documents/71759a44353543 1395eb34ebead091cb.pdf (accessed January 26, 2020).

[67] F. Chen, F. Cao, H. Pan, K. Wang, Q. Shen, J. Li, S. Wang, Mechanical and dielectric properties of silicon nitride ceramics with high and hierarchical porosity, Mater. Des. 40 (2012) 562–566. https://doi.org/10.1016/j.matdes.2012.03.026.

[68] L. Fangsen, Z. Wancheng, H. Hanjun, L. Fa, Z. Dongmei, High performance porous Si3N4 ceramics prepared by coated pore-forming agent method, Ceram. Int. 35 (2009) 3169–3173. https://doi.org/10.1016/j.ceramint.2009.05.007.

[69] Jain,R.,“Gel Electrophoresis, (n.d.). https://www.slideshare.net/RishabhJain413/lectut-btn202pptl13-gel-electrophoresis (accessed June 12, 2023).

[70] Electrophoresis Acrylamide Polymerization- A practical approach, (n.d.). https://www.bio-rad.com/webroot/web/pdf/lsr/literature/Bulletin_1156.pdf (accessed June 12, 2023).

[71] G.M. Dursun, C. Duran, Glass alumina composites for functional and structural applications, Ceram. Int. 45 (2019) 12550–12557. https://doi.org/10.1016/j.ceramint.2019.03.194.

[72] and D.B.M. B. R. Lawn, A. G. Evans, Elastic/Plastic Indentation 103 Damage in Ceramics: The Median/Radial Crack System, J. Am. Ceram. Soc. 63 (1980) 574–581.

[73] J. Kübler, P.L.J. Gauckler, Mechanical Properties of Ceramics Aim of chapter & Learning targets, Mater. Sci. (2010) 1–21.

[74] P.T.B. Hasselman, D. P. H. & Shaffer, "Factors Affecting Thermal Shock Resistance of Polyphase Ceramic Bodies," 1962. http://www.dtic.mil/dtic/tr/fulltext/u2/a281579.pdf.

[75] Almatis, Calcined and Reactive Aluminas for Refractories Calcined, (2014) 1–6.

[76] Nabeltec, Nabeltec, (n.d.). https://nabaltec.de/fileadmin/user_upload/03_produkte/03-5_synthetischermullit/nabaltec_tds_symulox-m72.pdf.

[77] R. Roy, D. Das, P.K. Rout, A Review of Advanced Mullite Ceramics, Eng. Sci. (2022) 1–11. https://doi.org/10.30919/es8d582.

[78] Z. Zhang, X. Duan, B. Qiu, Z. Yang, D. Cai, P. He, D. Jia, Y. Zhou, Anisotropic properties of textured h-BN matrix ceramics prepared using 3Y2O3-5Al2O3(-4MgO) as sintering additives, J. Eur. Ceram. Soc. 39 (2019) 1788–1795. https://doi.org/10.1016/j.jeurceramsoc.2019.01.003.

[79] Z. Tian, Y. Wang, Z. Zhang, X. Duan, D. Jia, S. Wu, The effects of holding time on grain size, orientation degree and properties of h-BN matrix textured ceramics, Mater. Chem. Phys. 248 (2020) 122916. https://doi.org/10.1016/j.matchemphys.2020.122916.

[80]. www.makeitfrom.com/materialproperties/Hexagonal-Boron-Nitride-BN (accessed January 26, 2020).

[81] Y. Baik, R.A.L. Drew, Aluminum nitride: Processing and applications, Key Eng. Mater. 124 (1996) 553–570. https://doi.org/10.4028/www.scientific.net/kem.122-124.553.

[82] J.S. Thorp, D. Evans, M. Al-Naief, M. Akhtaruzzaman, The dielectric properties of aluminium nitride substrates for microelectronics packaging, J. Mater. Sci. 25 (1990) 4965–4971. https://doi.org/10.1007/BF00580114.

[83] T.H. Chiang, T.E. Hsieh, A study of encapsulation resin containing hexagonal boron nitride (hBN) as inorganic filler, J. Inorg. Organomet. Polym. Mater. 16 (2006) 175–183. https://doi.org/10.1007/s10904-006-9037-8.

[84] W.-H.L. Chung-Lun Lo , Jenq-Gong Duh,Bi-Shiou Chiou, Low-Temperature Sintering and Microwave Dielectric Properties of Anorthite-Based Glass-Ceramics, J. Am. Ceram. Soc. 85 [9] (2002) 2230–35.

[85] Q. Li, D. Cai, Z. Yang, X. Duan, D. Li, Y. Sun, Effects of BN on the microstructural evolution and mechanical properties of BAS-BN composites, Ceram. Int. 45 (2019) 1627–1633. https://doi.org/10.1016/j.ceramint.2018.10.039.

[86] W.S. Cho, Z.H. Piao, K.J. Lee, Y.C. Yoo, J.H. Lee, M.W. Cho, Y.C. Hong, K. Park, W.S. Hwang, Microstructure and mechanical properties of AlN-hBN based machinable ceramics prepared by pressureless sintering, J. Eur. Ceram. Soc. 27 (2007) 1425–1430. https://doi.org/10.1016/j.jeurceramsoc.2006.05.044.

[87] J.E.D.& G.R.R. Robert D. Shannon, Dielectric constants of crystalline and amorphous spodumene, anorthite and diopside and the oxide additivity rule, Phys. Chem. Miner. Vol. 19 (1992) 148–156.

[88] S.J. Penn, N.M.N. Alford, A. Templeton, X. Wang, M. Xu, M. Reece, K. Schrapel, Effect of porosity and grain size on the microwave dielectric properties of sintered alumina, J. Am. Ceram. Soc. 80 (1997) 1885–1888.

https://doi.org/10.1111/j.1151-2916.1997.tb03066.x.

[89] K.P. Hong, I.J. Choi, J.W. Jung, H.R. Choi, Y.S. Cho, J. Kwak, D.H. Kang, Densification, crystallization, and dielectric properties of ALN, BN, and Si3N4 filler-containing LTCC materials, Int. J. Appl. Ceram. Technol. 10 (2013) E25–E32. https://doi.org/10.1111/j.1744-7402.2012.02825.x.

[90] S. Wang, D. Jia, Z. Yang, X. Duan, Z. Tian, Y. Zhou, Effect of BN content on microstructures, mechanical and dielectric properties of porous BN/Si3N4 composite ceramics prepared by gel casting, Ceram. Int. 39 (2013) 4231–4237. https://doi.org/10.1016/j.ceramint.2012.11.005.

[91] U.C. and A.W. Sleight, Ceramic Substrates for Microelectronic Packaging, Annu. Rev. Mater. Sci. 17 (1987) 323–340.

[92] M.E. Schmalko, R.O. Morawicki, L.A. Ramallo, Simultaneous determination of specific heat capacity and thermal conductivity using the finite-difference method, J. Food Eng. 31 (1997) 531–540. https://doi.org/10.1016/S0260-8774(96)00074-X.

[93] P. Xia, Z. Li, W. Wu, Y. Zhu, D. Feng, Effects of AlN on the thermal and mechanical properties of vitrified bond and vitrified CBN composites, Ceram. Int. 40 (2014) 12759–12764. https://doi.org/10.1016/j.ceramint.2014.04.129.

[94] C. Kittel, Interpretation of the thermal conductivity of glasses, Phys. Rev. 75 (1949) 972–974. https://doi.org/10.1103/PhysRev.75.972.

[95] Q. Li, D. Cai, Z. Yang, X. Duan, P. He, Y. Sun, Thermal properties and thermal shock resistance of BAS-BN composite ceramics, Ceram. Int. 45 (2019) 8181–8187. https://doi.org/10.1016/j.ceramint.2019.01.120.

[96] P. Rutkowski, W. Piekarczyk, L. Stobierski, G. Górny, Anisotropy of elastic properties and thermal conductivity of Al 2O3/h-BN composites, J. Therm. Anal. Calorim. 115 (2014) 461–466. https://doi.org/10.1007/s10973-013-3246-5.

[97] V. Semiconductor, Basic Mechanical and Thermal Properties of Silicon, Growth (Lakeland). 22401 (2000) 1–4. http://www.virginiasemi.com/pdf/Basic

Mechanical and Thermal Properties of Silicon.pdf.

[98] W. Paszkowicz, J.B. Pelka, M. Knapp, T. Szyszko, S. Podsiadlo, Lattice parameters and anisotropic thermal expansion of hexagonal boron nitride in the 10-297.5 K temperature range, Appl. Phys. A Mater. Sci. Process. 75 (2002) 431–435. https://doi.org/10.1007/s003390100999.

[99] V.M.F. Marques, D.U. Tulyaganov, S. Agathopoulos, V.K. Gataullin, G.P. Kothiyal, J.M.F. Ferreira, Low temperature synthesis of anorthite based glass-ceramics via sintering and crystallization of glass-powder compacts, J. Eur. Ceram. Soc. 26 (2006) 2503–2510. https://doi.org/10.1016/j.jeurceramsoc.2005.07.055.

[100] A. Kovalčíková, J. Balko, C. Balázsi, P. Hvizdoš, J. Dusza, Influence of hBN content on mechanical and tribological properties of Si3N4/BN ceramic composites, J. Eur. Ceram. Soc. 34 (2014) 3319–3328. https://doi.org/10.1016/j.jeurceramsoc.2014.02.021.

[101] L.F. Nielsen, Strength and stiffness of porous materials, J. Am. Ceram. Soc. 73(9) (1990) 2684–2689.

[102] N. Ecebaş, G.M. Dursun, A.H. Yeşilova, C. Duran, Gel casting of mullite for radome applications, Int. J. Appl. Ceram. Technol. 17 (2020) 264–273. https://doi.org/10.1111/ijac.13269.

[103] G.M. DURSUN, ALUMINA/GLASS COMPOSITES FOR LOW TEMPERATURE CO-FIRED CERAMICS (LTCC) AND RADOME APPLICATIONS, Ankara Yıldırım Beyazıt, 2019.

[104] J. Matousek, Chemistry of Evaporation from Silicate Melts, n.d.

[105] L. Zhang, S. Olhero, J.M.F. Ferreira, Thermo-mechanical and high-temperature dielectric properties of cordierite-mullite-alumina ceramics, Ceram. Int. 42 (2016) 16897–16905. https://doi.org/10.1016/j.ceramint.2016.07.188.

[106] M.D. Vaudin, Texture Development and Microstructure Evolution in, 16 (2000) 3109–3116.

[107] K.W. LAY, Grain Growth in UO2-Al,O3 in the Presence of a Liquid Phase, J. Am. Ceram. Soc. 51 (1968) 373–377. https://doi.org/10.1111/j.1151-2916.1968.tb11896.x.

[108] B. Biswal, D.K. Mishra, S.N. Das, S. Bhuyan, Structural, micro-structural, optical and dielectric behavior of mullite ceramics, Ceram. Int. 47 (2021) 32252–32263. https://doi.org/10.1016/j.ceramint.2021.08.120.

[109] X. Chen, W. Zhang, S. Bai, Y. Du, Densification and characterization of SiO2B2O 3CaOMgO glass/Al2O3 composites for LTCC application, Ceram. Int. 39 (2013) 6355–6361. https://doi.org/10.1016/j.ceramint.2013.01.061.

[110] V.L. Gurevich, A.K. Tagantsev, Advances in Physics Intrinsic dielectric loss in crystals, Adv. Phys. 40 (1991) 719–767.

[111] E. Of, F. Them, M Easurement of M Icrowave D Ielectric, 2008.

[112] B. Feng, G. Li, Z. Pan, H. Xiaoming, L. Peihai, H. Zhu, L. Yawei, X. Fan, Effect of synthesis processes on the thermoelectric properties of BiCuSeO oxyselenides, J. Alloys Compd. 754 (2018) 131–138. https://doi.org/10.1016/j.jallcom.2018.04.307.

[113] Ferro Ceramic INC. -mullite properties, (n.d.). http://www.ferroceramic.com/mullite_table.htm (accessed June 6, 2022).

[114] and W.D.K. Y.-M. Chiang, D. P. Birnie, Physical Ceramics, (1997).

[115] O. Bilaç, G.M. Dursun, C. Duran, Processing and properties of nano-hBN-added glass/ceramic composites for low-temperature co-fired ceramic applications, J. Korean Ceram. Soc. 59 (2022) 383–392. https://doi.org/10.1007/s43207-021-00185-7.

[116] Y. Zhang, C. Jia, High-performance cyanate ester composites with plasma-synthesized MgSiO3-SiO2-hBN powders for thermally conductive and dielectric properties, Ceram. Int. 45 (2019) 6491–6498. https://doi.org/10.1016/j.ceramint.2018.12.138.

[117] G. hua Chen, X. yu Liu, Influence of AlN addition on thermal and mechanical

properties of cordierite-based glass/ceramic composites, J. Mater. Process. Technol. 190 (2007) 77–80. https://doi.org/10.1016/j.jmatprotec.2007.03.106.

[118] L. Yuan, B. Liu, N. Shen, T. Zhai, D. Yang, Synthesis and properties of borosilicate/AlN composite for low temperature co-fired ceramics application, J. Alloys Compd. 593 (2014) 34–40. https://doi.org/10.1016/j.jallcom.2014.01.074.

[119] Z. Sun, W. Li, Y. Liu, H. Zhang, D. Zhu, H. Sun, C. Hu, S. Chen, Design and preparation of a novel degradable low-temperature co-fired ceramic (LTCC) composites, Ceram. Int. 45 (2019) 7001–7010. https://doi.org/10.1016/j.ceramint.2018.12.201.

[120] S. Kume, M. Yasuoka, N. Omura, K. Watari, Effect of additives on dielectric loss of AlN ceramics, Key Eng. Mater. 317–318 (2006) 845–848. https://doi.org/10.4028/www.scientific.net/kem.317-318.845.

[121] X. Feng, Y. Lv, L. Zhang, D. Ge, X. Li, J. Sun, J. Ding, L. Chen, K. Zheng, X. Zhang, X. Tian, Effect of AlN addition on phase formation in the LTCC with Al2O3/AlN biphasic ceramics based on BBSZ glass, Ceram. Int. 46 (2020) 16895–16900. https://doi.org/10.1016/j.ceramint.2020.03.268.

[122] M. Ma, Z. Liu, Y. Li, Y. Zeng, D. Yao, Enhanced thermal conductivity of low-temperature sintered borosilicate glass-AlN composites with β-Si3N4 whiskers, J. Eur. Ceram. Soc. 33 (2013) 833–839. https://doi.org/10.1016/j.jeurceramsoc.2012.09.030.

[123] M.M. Mokhayer, M.G. Kakroudi, S.S. Milani, H. Ghiasi, N.P. Vafa, Investigation of AlN addition on the microstructure and mechanical properties of TiB2 ceramics, Ceram. Int. 45 (2019) 16577–16583. https://doi.org/10.1016/j.ceramint.2019.05.196.

[124] S. Liu, H. Zhang, B. Zhang, X. Zhong, J. Ma, F. Ye, Fabrication and properties of cordierite based glass/AlN composites by sol-gel and pressureless sintering, Ceram. Int. 42 (2016) 7253–7258. https://doi.org/10.1016/j.ceramint.2016.01.119.

[125] C. Society, Mechanical Properties with and Microstructure Scale of Si3N4 Matrix SiC Particles Composite Gen SASAKI , Hirofumi NAKASE , Katsuaki SUGANUMA , Teruaki FUJITA and Koichi NIIHARA * National Defense Academy , * ISIR , Osaka Osaka 567 SiC*f*i *f*m *f* ~ *f*b*f*N *f*X , Ì, 540 (1992).

[126] J.F. Yang, T. Ohji, T. Sekino, C.L. Li, K. Niihara, Phase transformation, microstructure and mechanical properties of Si3N4/SiC composite, J. Eur. Ceram. Soc. 21 (2001) 2179–2183. https://doi.org/10.1016/S0955-2219(01)00193-5.

[127] T. Kusunose, T. Sekino, Y.H. Choa, K. Niihara, Fabrication and microstructure of silicon nitride/boron nitride nanocomposites, J. Am. Ceram. Soc. 85 (2002) 2678–2688. https://doi.org/10.1111/j.1151-2916.2002.tb00514.x.

[128] R.C. Souza, C. Dos Santos, M.J.R. Barboza, L. De Araujo Bicalho, C.A.R.P. Baptista, C.N. Elias, Fatigue behavior of 3%Y2O3-doped ZrO2 ceramics, J. Mater. Res. Technol. 3 (2014) 48–54. https://doi.org/10.1016/j.jmrt.2013.10.005.

[129] Y. Fu, Z. Tao, X. Hou, Weibull distribution of the fracture strength of 99% alumina ceramic reshaped by cold isostatic pressing, Ceram. Int. 40 (2014) 7661–7667. https://doi.org/10.1016/j.ceramint.2013.12.053.

[130] T. Kenion, N. Yang, C. Xu, Dielectric and mechanical properties of hypersonic radome materials and metamaterial design: A review, J. Eur. Ceram. Soc. 42 (2022) 1–17. https://doi.org/10.1016/j.jeurceramsoc.2021.10.006.

[131] MT Sebastian, Dielectric Materials for Wireless Communications, 1st ed., Elsevier, Amsterdam, 2008.

[132] B. Bitterlich, C. Lutz, A. Roosen, Rheological characterization of water-based slurries for the tape casting process, Ceram. Int. 28 (2002) 675–683. https://doi.org/10.1016/S0272-8842(02)00027-5.